Juha-Matti Pirkkalainen Mechanical Resonators Coupled to Superconducting Circuits

Aalto University

O.V. Lounasmaa Laboratory
Department of Applied Physics

Mechanical Resonators Coupled to Superconducting Circuits

Juha-Matti Pirkkalainen

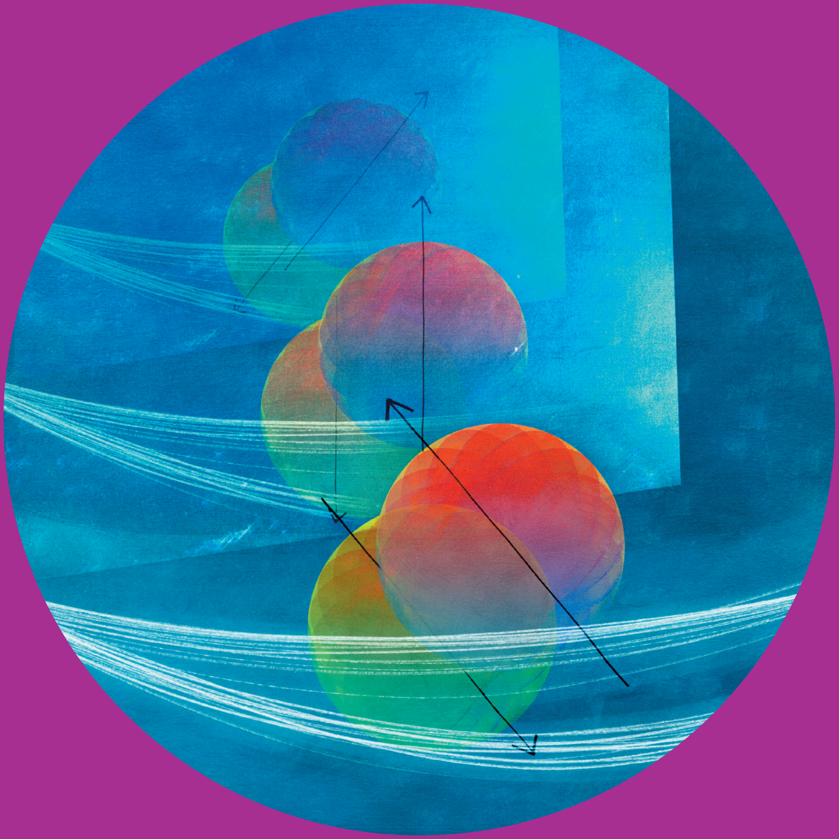

Aalto University

DOCTORAL DISSERTATIONS

Aalto University publication series
DOCTORAL DISSERTATIONS 24/2014

Mechanical Resonators Coupled to Superconducting Circuits

Juha-Matti Pirkkalainen

A doctoral dissertation completed for the degree of Doctor of Science (Technology) to be defended, with the permission of the Aalto University School of Science, at a public examination held at the lecture hall T2 of the school on 11 April 2014 at 1 pm.

Aalto University
School of Science
O.V. Lounasmaa Laboratory, NEMS Group
Department of Applied Physics

Supervising professor
Prof. Mika Sillanpää

Thesis advisor
Prof. Mika Sillanpää

Preliminary examiners
Prof. Daniel Esteve, CEA-Saclay, France
Prof. Göran Johansson, Chalmers University of Technology, Sweden

Opponent
Prof. Eugene Polzik, Niels Bohr Institute, Copenhagen University, Denmark

Aalto University publication series
DOCTORAL DISSERTATIONS 24/2014

ISBN 978-952-60-5580-0
ISBN 978-952-60-5581-7 (pdf)
ISSN-L 1799-4934
ISSN 1799-4934 (printed)
ISSN 1799-4942 (pdf)
http://urn.fi/URN:ISBN:978-952-60-5581-7

Images: Cover image by Juha Juvonen

Unigrafia Oy
Helsinki 2014

Finland

NORDIC ECOLABEL
441 697
Printed matter

A? **Aalto University**

Abstract

Aalto University, P.O. Box 11000, FI-00076 Aalto www.aalto.fi

Author
Juha-Matti Pirkkalainen

Name of the doctoral dissertation
Mechanical Resonators Coupled to Superconducting Circuits

Publisher School of Science

Unit O.V. Lounasmaa Laboratory; Department of Applied Physics

Series Aalto University publication series DOCTORAL DISSERTATIONS 24/2014

Field of research Engineering Physics

Manuscript submitted 17 December 2013 **Date of the defence** 11 April 2014

Permission to publish granted (date) 6 February 2014 **Language** English

☐ **Monograph** ☒ **Article dissertation (summary + original articles)**

Abstract

In the late 1960s and early 1970s, the development of mechanical resonators was pushed forward in efforts to record gravitational waves. In order to push down the limit of the smallest detectable force, the radiation circulating in a Fabry-Perot cavity was demonstrated to modify the damping of the cavity end-mirror suspended to act as a mechanical resonator. A few years later, motivated by the study of the internal properties of atoms and ions, the radiation pressure of light was realized as a means to cool atomic motion. In the following years, the ground-state cooling of ion motion was achieved in landmark studies. For mechanical resonators parametrically coupled to Fabry-Perot cavities, it took much longer to reach quantum ground-state cooling, both in the microwave domain, where the original experiments took place, and in the optical domain. Ground-state cooling in both regimes was reached by three groups during the preparation of this thesis and was largely due to advancements in the fabrication methods.

Ground-state cooling allows, in principle, the quantum nature of mechanical resonators to be probed and harnessed. Microwave domain devices, which are focused on in this thesis, have the advantage that nonlinear elements (superconducting quantum bits, qubits) are readily available. These elements enable nonclassical state preparation of the qubit and the subsequent transfer to the microwave cavity. The goal is to transfer these quantum states to mechanical resonators. This would allow mechanics to be used as a quantum mechanical memory in quantum information processing thanks to their long lifetimes.

In this thesis, various aspects of microwave domain circuit optomechanics are studied. The main goal of this thesis is to study how to enhance the coupling between a quantum regime microwave device and a mechanical resonator by using Josephson junction –based qubits. Coherent interaction between a superconducting qubit and a classical driven mechanical field is demonstrated. The analysis presented in this thesis predicts that ground-state cooling and coherent state transfer is possible in the single-phonon regime with transmon-regime qubits. Also, traditional linear optomechanical systems are considered in which the mechanical resonator is coupled to an electrical resonator. Such systems exhibit a rich spectrum of phenomena from which the quantum-limited amplification and multimode effects are considered in this thesis. It is shown that the system operates near quantum-limited amplification, which could be reached if the mechanical resonator was in the ground state.

Keywords optomechanics, mechanical resonators, superconducting qubits

ISBN (printed) 978-952-60-5580-0 **ISBN (pdf)** 978-952-60-5581-7

ISSN-L 1799-4934 **ISSN (printed)** 1799-4934 **ISSN (pdf)** 1799-4942

Location of publisher Helsinki **Location of printing** Helsinki **Year** 2014

Pages 191 **urn** http://urn.fi/URN:ISBN:978-952-60-5581-7

Tiivistelmä

Aalto-yliopisto, PL 11000, 00076 Aalto www.aalto.fi

Tekijä Juha-Matti Pirkkalainen	
Väitöskirjan nimi Mekaanisten värähtelijöiden kytkeminen suprajohtaviin piireihin	
Julkaisija Perustieteiden korkeakoulu	
Yksikkö O.V. Lounasmaa -laboratorio; Teknillisen fysiikan laitos	
Sarja Aalto University publication series DOCTORAL DISSERTATIONS 24/2014	
Tutkimusala Teknillinen fysiikka	
Käsikirjoituksen pvm 17.12.2013	**Väitöspäivä** 11.04.2014
Julkaisuluvan myöntämispäivä 06.02.2014	**Kieli** Englanti
☐ **Monografia**	☒ **Yhdistelmäväitöskirja (yhteenveto-osa + erillisartikkelit)**

Tiivistelmä

1960- ja 1970-luvun taitteessa kehitettiin mekaanisia värähtelijöitä entistä herkemmiksi mittalaitteiksi. Tätä kehitystä ajoi eteenpäin muun muassa yritykset mitata gravitaatioaaltoja. Yhä pienempien voimien erottamiseksi osoitettiin, että kaviteetin yhtenä päätypeilinä toimivan mekaanisen värähtelijän häviöitä pystyttiin hallitsemaan kaviteettiin syötettävän sähkömagneettisen kentän avulla. Muutamia vuosia myöhemmin atomien sisäisten rakenteiden tutkijat esittivät, että säteilypaineen avulla pystyttiin jäähdyttämään atomien liikettä. Tästä alkanut kehityskulku johti ionien liikkeen jäähdyttämiseen perustilaansa kokeissa, joita pidetään erittäin merkittävinä tieteellisinä saavutuksina. Mekaanisten värähtelijöiden jäähdyttäminen perustilaan niihin kytketyn kaviteetin avulla vei paljon enemmän aikaa ja ne saavutettiin niin optisella kuin mikroaaltoalueellakin vasta tällä vuosikymmenellä paljolti kehittyneiden valmistusmenetelmien ansiosta.

Mekaanisten värähtelijöiden jäähdyttäminen perustilaan mahdollistaa niiden kvanttimekaanisen luonteen todentamisen sekä hyödyntämisen. Mikroalueella toimivien suprajohtavien piirien, joita tässä väitöskirjassa käytetään, etuna on kehittyneiden epälineaaristen komponenttien (kvanttibittien eli kubittien) helppo valmistus. Epälineaariset komponentit mahdollistavat epäklassisten tilojen luomisen kubittiin sekä tilan siirron mikroaaltokaviteettiin ja mekaaniseen värähtelijään. Mekaanisia värähtelijöitä voidaan näissä systeemeissä käyttää kvanttimekaanisen tiedon tallentamiseen niiden erinomaisen elinajan ansiosta.

Tämän väitöskirjan aiheina ovat mikroaaltoalueen lineaarinen ja epälineaarinen optomekaniikka. Päätavoitteena on tutkia optomekaanisen kytkennän kasvattamista Josephson-liitoksiin perustuvien suprajohtavien piirien avulla. Työn päätuloksena toteutetaan kvanttikoherentti kytkentä suprajohtavan kubitin ja klassisen mekaanisen värähtelijän välillä. Työssä analysoidaan lisäksi mekaanisen värähtelijän kytkemistä niin kutsuttuun transmon-kubittiin ja osoitetaan, että mekaaniikan perustilalle jäähdyttäminen sekä koherentti kytkentä kubittiin on mahdollista yhden mekaanisen kvantin tasolla. Väitöskirjassa tutkitaan myös lineaarista optomekaniikkaa, jossa mekaaninen värähtelijä on lineaarisesti kytketty sähköiseen värähtelijään. Työssä näytetään, että systeemi toimii vahvistimena sähköiseen värähtelijään tuleville mikroaalloille ja osoitetaan vahvistuksen kohinan olevan kvanttimekaaniikan lakien rajoittamaa, jos mekaaninen värähtelijä itse on jäähdytetty perustilaansa.

Avainsanat optomekaniikka, mekaaniset värähtelijät, suprajohtavat kubitit

ISBN (painettu) 978-952-60-5580-0	**ISBN (pdf)** 978-952-60-5581-7	
ISSN-L 1799-4934	**ISSN (painettu)** 1799-4934	**ISSN (pdf)** 1799-4942
Julkaisupaikka Helsinki	**Painopaikka** Helsinki	**Vuosi** 2014
Sivumäärä 191	**urn** http://urn.fi/URN:ISBN:978-952-60-5581-7	

Preface

This thesis is the result of work conducted in O.V. Lounasmaa Laboratory between February 2010 and December 2013. When I joined the lab four years ago, I had no clue what to expect except a lot of learning. In retrospective, I consider myself very privileged to have had the opportunity to work in such a thriving science community. Today it is easy to say that my expectations of the amount of learning to be done were greatly underestimated.

During the four years I have worked in the lab, I have managed to gather a long list of people to thank for. Undoubtedly, my supervisor Prof. Mika Sillanpää deserves to be applauded the most for his contribution. I had practically no experience on experimental physics when I started in his group and he really taught me hands-on and from the scratch all the fabrication tricks and the quirks of measurements. I thank him for all the patience and trust he has had on me over the years. In addition to the guidance he has given me, he has provided me an exemplary role model of a top-level physicist.

I want to thank the director of our lab, Prof. Pertti Hakonen for his contributions to my thesis both scientifically and through the enormous amount of work he puts in to make the lab run as a whole. I also want to thank the former director of the laboratory Prof. Mikko Paalanen and all the lab administration for making it possible for me complete the thesis in our laboratory.

I am grateful to the head of the Theory group, Prof. Tero Heikkilä as well as to Dr. Francesco Massel for a long and fruitful collaboration and for guiding my reasonings on various theoretical problems. I am also indebted to Doc. Sorin Paraoanu and the members of his Kvantti group: Karthikeyan Kumar, Dr. Khattiya Chalapat, Antti Vepsäläinen, and Sergey Danilin.

Especially I want to thank the members of our NEMS group for making the atmosphere in the group truly enjoyable and open to discussions and ideas. I thank Jaakko Sulkko for his companionship during all these years, former members Dr. Sung Un Cho, Dr. Tommy Holmqvist, and Dr. Meri Helle for their part in this thesis as well as the current line-up: Dr. Matthias Brandt, Erno Damskägg, and Mikael Kervinen. I am grateful for Dr. Jian Li for both the work we did together back when he was part of the Kvantti group and for the time I have had the pleasure to work with him in our group. His thorough understanding of physics is a rare trait and makes him a fantastic to bounce off ideas with. As one of the former members, I am thankful to Maria Berdova for always having a cheerful mood to lighten up my day and for the collaborations we had with Prof. Sami Franssila's group after her departure.

I want to express my gratitude to all the co-authors of the articles included in this thesis: Dr. David Gunnarsson for his determination to finish the work, Dr. Mika Prunnila, Dr. Xuefeng Song, and Dr. Heini Saloniemi. I am indebted to Dr. Matti Silveri for introducing me to Floquet formalism. I want to also thank Prof. Erkki Thuneberg and Dr. Jani Tuorila for their contributions to this thesis.

The community in O.V. Lounasmaa Laboratory has had a huge part in making my years here unforgettable. Listing everybody here would be a challenging task but a few I want to mention especially: Dr. Juho Rysti, Pasi Häkkinen, Matti Tomi, Daniel Cox, Raphaël Khan, Ville Kauppila, Dr. Teemu Ojanen, Doc. Mikko Möttönen, Dr. Pauli Virtanen, Antti Puska, Pasi Lähteenmäki, Dr. Matti Laakso, Dr. Jaakko Hosio, Petri Heikkinen, Matti Manninen, and Dr. Anssi Salmela.

Dr. Alexander Savin has been instrumental in keeping the lab running and for me it is difficult to even see how that would be possible without him. I am grateful to him for helping me out immediately with problems, big or small, that I have faced. I want to also thank the workshop staff for their great work: Arvi Isomäki, Jari Isomäki, Hannu Kaukelin, and Markku Korhonen.

I am most thankful to Dr. Timo Hakkarainen for his friendship during our undergraduate and graduate studies. I thank my father Matti, mother Ritva, the whole rest of the family, and my friends for their love and support during the completion of this thesis. And finally, I want to thank my beloved wife Pälvi. You and your love have made all these efforts worthwhile and continue to do so long after this thesis is forgotten.

Helsinki, February 9, 2014,

Juha Pirkkalainen

Contents

List of publications

This thesis is based on the following original publications, referred hereafter by the respective Roman numeral.

I F. Massel, T. T. Heikkilä, J.-M. Pirkkalainen, S. U. Cho, H. Saloniemi, P. J. Hakonen, and M. A. Sillanpää. *Microwave amplification with nanomechanical resonators*. Nature **480**, 351–354 (2011).
DOI: 10.1038/nature10628

II F. Massel, S. U. Cho, J.-M. Pirkkalainen, P. J. Hakonen, T. T. Heikkilä, and M. A. Sillanpää. *Multimode circuit optomechanics near the quantum limit*. Nature Communications **3**, 987 (2012).
DOI: 10.1038/ncomms1993

III J. Li, M. P. Silveri, K. S. Kumar, J.-M. Pirkkalainen, A. Vepsäläinen, W. C. Chien, J. Tuorila, M. A. Sillanpää, P. J. Hakonen, E. V. Thuneberg, and G. S. Paraoanu. *Motional averaging in a superconducting qubit*. Nature Communications **4**, 1420 (2013).
DOI: 10.1038/ncomms2383

IV J.-M. Pirkkalainen, S. U. Cho, J. Li, G. S. Paraoanu, P. J. Hakonen, and M. A. Sillanpää. *Hybrid circuit cavity quantum electrodynamics with a micromechanical resonator*. Nature **494**, 211–215 (2013).
DOI: 10.1038/nature11821

V D. Gunnarsson, J.-M. Pirkkalainen, J. Li, G. S. Paraoanu, P. J. Hakonen, M. A. Sillanpää, and M. Prunnila. *Dielectric losses in multi-layer Josephson junction qubits*. Superconductor Science and Technology **26**, 085010 (2013).
DOI: 10.1088/0953-2048/26/8/085010

VI M. Berdova, S. U. Cho, J.-M. Pirkkalainen, J. Sulkko, X. Song, P. J. Hakonen, and M. A. Sillanpää. *Micromanipulation transfer of membrane resonators for circuit optomechanics*. Journal of Micromechanics and Microengineering **23**, 125024 (2013).
DOI: 10.1088/0960-1317/23/12/125024

Author’s contribution

In Publications **I** and **II**, the author contributed to the design and fabrication of the samples, to the cryogenic set-up, and to the writing of the manuscript.

In Publication **III**, the author in part designed the Sample, fabricated the Sample, made the characterizing measurements, and commented on the manuscript at different stages of manuscript preparation.

In Publication **IV**, the author in part designed the Sample, developed the fabrication technique for the mechanical resonators, and fabricated samples. The author developed the cryogenic and room temperature measurement setup, carried out the measurements, and developed most of the theoretical modeling. The author wrote the first version of the manuscript and did most of the data analysis. Extensive supplementary published with the main article was mainly written by the author.

In Publication **V**, the author carried out most of the measurements of the phase qubits and commented on the manuscript at different stages of manuscript preparation.

In Publication **VI**, the author fabricated and measured the Sample together with the main author and participated in writing the manuscript.

The introduction part of this thesis contains new material about nonlinear optomechanics and especially about coupling a transmon qubit to a mechanical resonator. The author has developed the theory and is solely responsible for these unpublished pieces.

Chapter 1

Introduction

Throughout the history of physics, mechanical systems have served as state-of-the-art measurement devices. Torsional oscillators were the most sensitive devices for measuring minute forces for a long time. They were used as early as the end of 18th century in the famous Cavendish experiment which measured gravitational pull between two test masses [1]. They were also used in experiments by Coulomb to study the interaction between electric charges [2], thus establishing the form of Coulomb's law. More modern versions of mechanical measurement devices are, for example, atomic force microscopes [3] and quartz tuning forks, which are used to measure the properties of superfluid helium [4].

Even before any of the experiments above had been conducted, Johannes Kepler noticed in the early 17th century that the tails of comets always point away from the sun [5] and he attributed this to the radiation pressure of sun. Following Kepler, and again with mechanical measurement devices, it wasn't until the beginning of the 20th century that radiation pressure was reliably measured [6, 7].

Since then, mechanical resonators have evolved by utilizing radiation-pressure coupling to optical cavities. The canonical optomechanical setup consists of a harmonically suspended mirror acting as an end-mirror for an optical cavity [8], see Fig. 1.1. Similar optomechanical systems with two optical arms (a laser interferometer) were originally proposed for gravitation wave detection in the 1970s [9]. The definition of optomechanical systems should be taken in the broadest sense by including all the systems which can be described with identical equations of motion. Modern day implementations range from optical systems with mechanical micromirrors [10, 11], silica microtoroids [12], and optomechanical crystals [13] to microwave domain devices with nanomechanical beams [14, 15, 16] and drum resonators [17].

During the completion of this thesis, the optomechanical community raced towards the quantum ground-state cooling of mechanical resonators. This was

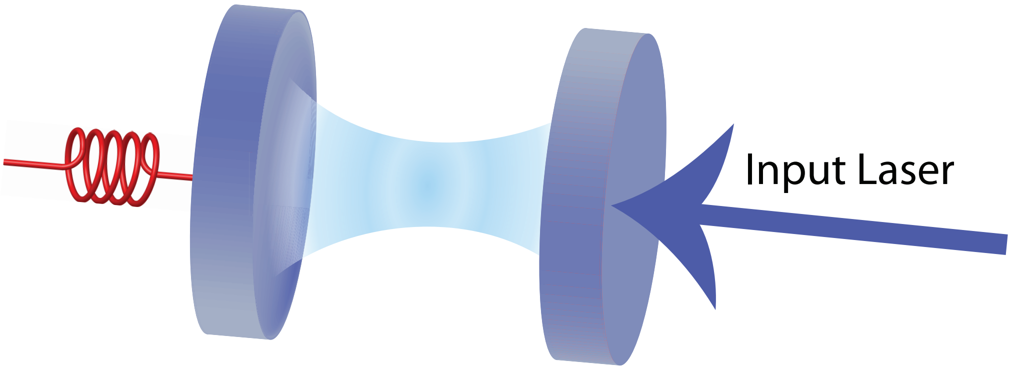

Fig. 1.1: Canonical optomechanical Fabry-Perot cavity with a harmonically suspended mirror.

achieved by three groups, first passively with a high frequency resonator [18], with a drum resonator in the microwave domain [19], and with optomechanical crystals [20] in the optical domain. Ground-state cooling is a prerequisite for mechanical state squeezing [21, 22] and entanglement [23], and it paves the way for more intricate experiments on mechanics.

In measurement applications [24], the advantage of mechanical resonators is that they can be functionalized to measure various forces while the engineered large optomechanical coupling to the cavity ensures an easy and sensitive read-out of the mechanics. Large optomechanical coupling can also be used in applications other than measurements. Coupling that is larger than the losses allows the mechanical and optical field to exchange their states [25]. This opens up a completely new field of coherent optomechanics where the property that historically rendered mechanical system as excellent measurement devices, namely the small lossy coupling to the environment, can be exploited, for example, in mechanical memory applications.

The overarching theme of this dissertation is utilizing mechanical elements as parts of superconducting circuits. The experiments presented study mechanical resonators that are coupled to both harmonic oscillators (Publications **I** and **II**) and quantum two-level systems (Publication **IV**), see Fig. 1.2. In both schemes, the coupling mechanism is radiation pressure and the main motivation is to use the mechanical resonator to enable quantum regime operations.

In Publication **I**, a mechanical resonator is used to amplify microwave signals at the microwave cavity resonance to which it is coupled. It is shown that the system can in principle operate as a quantum-limited amplifier by adding only half a quantum of noise to the input signal.

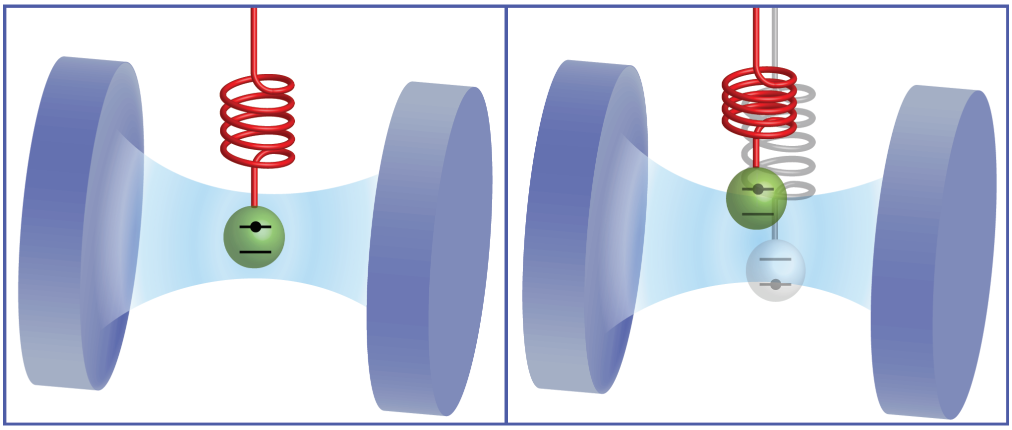

Fig. 1.2: Quantum two-level system coupled to a mechanical resonator and to an optical cavity for read-out (for reviews on closely related topics of atoms in a cavity or harmonically trapped ions, see Refs. [26, 27]). On the left, a Schrödinger cat entangled state between the qubit and mechanics is created.

Two such mechanical resonators are coupled to a common microwave cavity in Publication **II**. The mechanical resonance frequencies are closely spaced and the whole tripartite system is coupled by pumping the cavity to high occupation. Strong enough coupling hybridizes the three systems forming two cavity-like bright modes and a phonon-like dark mode with a long lifetime. The results of Publication **II** show the first signs of the dark mode. The dark mode allows for entangling the motion of two spatially separated mechanical resonators, a resource that is potentially useful in emerging quantum processing applications.

Dark mode could also possibly be used to store photonic information in mechanical phonons which would decay very slowly. A similar idea is pursued in Publication **IV** where a mechanically vibrating membrane is coupled with a superconducting transmon qubit. In this scheme, far larger single-phonon couplings can be attained in comparison to the abovementioned experiments. Coupling strengths larger than the decoherence rates of the qubit would allow state transfer and storage in the mechanical degree of freedom. Furthermore, such strong coupling allows for the construction of nonclassical mechanical states by using the nonlinear nature of the qubit.

The experiments in Publication **IV** show coherent interaction between the qubit and a classical mechanical field. The mechanical resonator is driven to high phonon occupation so that part of the classical field to which the qubit is coupled is electrical. It is shown, however, that 92% of the classical field is mechanical. Much of the introduction in this thesis is devoted to analyzing the prospect of reaching the strong coupling regime between a transmon-regime qubit and mechanics (see Sec. 3.2.2 and Sec. 3.5). In section 3.4, the possibility of protecting the qubit from dephasing is studied by driving the mechanics to high occupation.

The experiments presented in Publication **III**, in which similar motional averaging of a transmon qubit is induced by driving the flux degree of freedom, are closely related to the previously mentioned experiments. The system provides a platform for studying the phenomenon of motional averaging with readily tunable parameters.

The remaining two articles of this thesis concentrate on fabricational issues concerning the building blocks for optomechanical systems. Publication **V** reports on efforts to create a fabrication process for transmon and phase qubits without using e-beam lithography. The junctions are fabricated using vias in silicon nitride. This approach is shown to increase dielectric losses if the excess SiN_x is not removed from the samples.

The progress in optomechanical systems has been largely due to advanced fabrication methods of novel optomechanical devices. As a part of this tendency, Publication **VI** concentrates on creating mechanical resonators through micromanipulation [28]. The use of micromanipulation allows mechanical resonators to be combined with any kind of fabrication process that is used to create the other components. This is a significant advantage in a field where some fabrication processes can be very sensitive.

Chapter 2

Linear circuit optomechanics

The simplest scenario of radiation pressure is a photon travelling towards the positive x-axis and impinging on a small particle with no internal structure, see Fig. 2.1. In this collision, the incoming photon transfers momentum to the particle and is reflected directly back to the incoming direction. If the energy transferred to the particle by the photon is negligible compared to the photon energy ($\Delta\epsilon \ll \hbar\omega_c$), the momentum of the particle is changed by $\Delta p = +2\hbar k$ where $\hbar k$ is the momentum of the incoming particle.

Cavity optomechanics refers to a system where the resonance frequency of a cavity is shifted as a function of mechanical displacement. This construction immediately implies that radiation pressure force is acting on the mechanical element. Many possible implementations of such a system can be envisioned, one of them being an electrical LC circuit with the cavity frequency modulated by mechanically vibrating capacitance. The resonant frequency of such a circuit

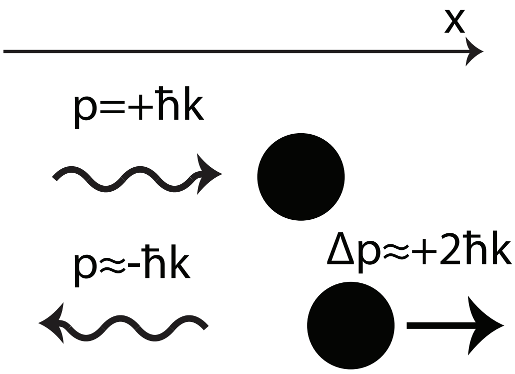

Fig. 2.1: Photon transferring momentum to a small particle.

is given by

$$\begin{aligned}\omega_c =& \frac{1}{\sqrt{LC(x)}} = \frac{1}{\sqrt{LC}}\frac{1}{\sqrt{1+\frac{\partial C_m(x)}{\partial x}\frac{x}{C}}} \\ \simeq& \omega_c\left(1-\frac{g_0}{\omega_c}(\hat{b}^\dagger+\hat{b})+\frac{3}{2}\frac{g_0^2}{\omega_c^2}(\hat{b}^\dagger+\hat{b})^2\right),\end{aligned} \tag{2.1}$$

where ω_c is the unperturbed resonance frequency of the cavity, $C_m(x)$ is the capacitance derivative with respect to the capacitor plate separation x (see below), $\hat{x} = x_{\text{zp}}(\hat{b}^\dagger + \hat{b})$, $\hat{b}$ is the annihilation operator for the mechanics [29], and the vacuum optomechanical coupling strength is

$$g_0 = \frac{\omega_c}{2C}\frac{\partial C_m(x)}{\partial x}x_{\text{zp}}, \tag{2.2}$$

with zero-point fluctuation amplitude

$$x_{\text{zp}} = \sqrt{\frac{\hbar}{2m_{\text{eff}}\omega_m}}, \tag{2.3}$$

where ω_m is the resonant frequency of the mechanics and m_{eff} is the corresponding effective mass. The value of m_{eff} depends on how the global amplitude x is defined, see appendix A for details.

In order to neglect the third term of Eq. (2.1) and retain only the first two, the third term needs to be negligible in comparison to the second one,

$$g_0(\hat{b}^\dagger + \hat{b}) \ll \omega_c, \tag{2.4}$$

which turns out to be experimentally very relevant. In this limit, it is appropriate to use the canonical optomechanical Hamiltonian

$$\hat{H} = \hbar\omega_c\hat{a}^\dagger\hat{a} + \hbar\omega_m\hat{b}^\dagger\hat{b} - \hbar g_0\hat{a}^\dagger\hat{a}(\hat{b}^\dagger + \hat{b}), \tag{2.5}$$

where $\hat{a}$ is the annihilation operator for the cavity.

2.1 Classical optomechanics

2.1.1 Microwave cavity

As the simplest circuit model for microwave cavity, we consider a parallel RLC circuit coupled to external measurement circuitry with capacitance C_{ex}, see Fig. 2.2(a).

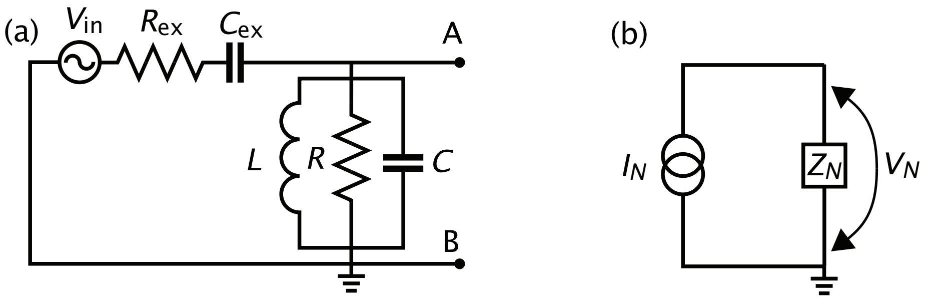

Fig. 2.2: (a) Circuit model of a parallel RLC microwave resonator coupled to an external ac voltage source through capacitance C_{ex} and resistance R_{ex}. (b) Generic equivalent Norton circuit diagram in which the voltage source is replaced a current source.

To study the loading of external circuitry, it is clarifying to transform the circuit into a Norton equivalent circuit. In Norton equivalent circuit model the voltage source is replaced with an equivalent current source in parallel with equivalent Norton impedance. To find the equivalent Norton impedance between points A and B in Fig. 2.2(a), we consider a circuit where the voltage source is replaced with a short. This gives

$$Z_N = \frac{Z_{\text{ex}} Z_{RLC}}{Z_{\text{ex}} + Z_{RLC}}, \tag{2.6}$$

where $Z_{\text{ex}} = R_{\text{ex}} + 1/(i\omega C_{\text{ex}})$ is the impedance of the input circuitry and Z_{RLC} is the impedance of the microwave resonator. The equivalent current for the current source can be found by shorting points A and B,

$$I_N = \frac{V_{\text{in}}}{Z_{\text{ex}}} = \frac{V_{\text{in}}}{R_{\text{ex}} + \frac{1}{i\omega C_{\text{ex}}}}. \tag{2.7}$$

Further insight is gained by transforming the input circuitry terms such that they parallel with the RLC circuit, see Fig. 2.3. Choosing [30]

$$\begin{aligned} R_{\text{ex,eq}} &= \frac{1 + \omega^2 R_{\text{ex}}^2 C_{\text{ex}}^2}{\omega^2 R_{\text{ex}} C_{\text{ex}}^2}, \\ C_{\text{ex,eq}} &= \frac{C_{\text{ex}}}{1 + \omega^2 R_{\text{ex}}^2 C_{\text{ex}}^2}, \end{aligned} \tag{2.8}$$

yields $1/Z_{\text{ex,eq}} \equiv 1/R_{\text{ex,eq}} + 1/C_{\text{ex,eq}} = 1/Z_{\text{ex}}$.

We can simplify these expressions by noting that $R_{\text{ex}} = 50\ \Omega$, $C_{\text{ex}} \approx 5$ fF, and $\omega/(2\pi) \approx 5$ GHz. These numbers indicate that $\omega R_{\text{ex}} C_{\text{ex}} \ll 1$, and we can

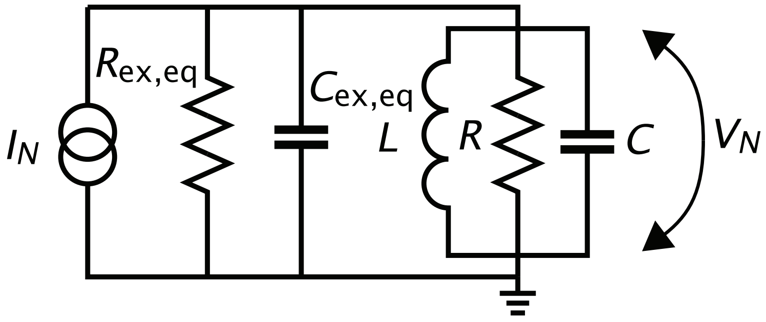

Fig. 2.3: Norton equivalent circuit model for a loaded parallel RLC microwave resonator.

approximate

$$\begin{aligned} R_{\text{ex,eq}} \approx& \frac{1}{\omega^2 R_{\text{ex}} C_{\text{ex}}^2}, \\ C_{\text{ex,eq}} \approx& C_{\text{ex}}. \end{aligned} \tag{2.9}$$

The circuit has now been transformed into a parallel RLC circuit with $C_{\text{tot}} = C + C_{\text{ex,eq}}$, $L_{\text{tot}} = L$, and $1/R_{\text{tot}} = 1/R + 1/R_{\text{ex,eq}}$. The Q-value for a parallel resonator is given by $Q = R_{\text{tot}}\sqrt{C_{\text{tot}}/L_{\text{tot}}}$. We can define internal and external quality factors by

$$\frac{1}{Q} = \frac{1}{Q_{\text{int}}} + \frac{1}{Q_{\text{ext}}}, \tag{2.10}$$

$$Q_{\text{int}} = R\sqrt{\frac{C + C_{\text{ex}}}{L}}, \tag{2.11}$$

$$Q_{\text{ext}} = R_{\text{ex,eq}}\sqrt{\frac{C + C_{\text{ex}}}{L}}. \tag{2.12}$$

The Q-factor defines the ratio of energy stored to the power loss,

$$\frac{Q}{\omega_c} = \frac{E}{P}. \tag{2.13}$$

Therefore, we can define the loss rate of the microwave resonator by $\kappa = \omega_c/Q$. Similarly to the Q-factor, the loss rate can be divided into internal and external components $\kappa = \kappa_{\text{int}} + \kappa_{\text{ext}}$,

$$\kappa_{\text{int}} = \frac{1}{R(C + C_{\text{ex}})} \tag{2.14}$$

$$\kappa_{\text{ext}} = \frac{R_{\text{ex}}}{C_{\text{tot}}}(\omega C_{\text{ex}})^2. \tag{2.15}$$

It is worth noting that the external loss rate grows quadratically with the coupling capacitance as long as $C \gg C_{\text{ex}}$.

The voltage in the transformed circuit is given by

$$V_N = Z_N I_N = I_N \omega_c Z_0 \frac{1}{\kappa + i(\omega - \omega_c)(1 + \omega_c/\omega)}. \tag{2.16}$$

In the limit $\omega R_{\text{ex}} C_{\text{ex}} \ll 1$, $I_N \approx i V_{\text{in}} \omega C_{\text{ex}}$. Furthermore, with external drive close to the resonant frequency, we can approximate $\omega_c/\omega \approx 1$ and write

$$V_N \approx I_N \omega_c Z_0 \frac{1}{\kappa + 2i(\omega - \omega_c)} \approx i V_{\text{in}} \sqrt{\frac{\kappa_{\text{ext}}}{R_{\text{ex}} C_{\text{tot}}}} \frac{1}{\kappa + 2i(\omega - \omega_c)}, \tag{2.17}$$

where $Z_0 = \sqrt{L/C_{\text{tot}}}$.

The energy stored in the resonator is given by

$$E = \frac{1}{2} C_{\text{tot}} V_{N,\text{rms}}^2 + \frac{1}{2} L I_{i,\text{rms}}^2, \tag{2.18}$$

where $V_{N,\text{rms}} = V_N/\sqrt{2}$ is the root mean square voltage over the capacitor and $I_{i,\text{rms}} = L_i/\sqrt{2}$ is the rms current flowing in the inductor. Close to resonance $I_{i,\text{rms}} \approx V_N/Z_0$ [30] and

$$E \approx \frac{1}{2} C_{\text{tot}} |V_N|^2 = \frac{V_{\text{in}}^2}{8} \frac{\kappa_{\text{ext}}}{R_{\text{ex}}} \frac{1}{(\omega - \omega_c)^2 + (\kappa/2)^2}. \tag{2.19}$$

Therefore, the energy stored in the resonator is a Lorentzian as a function of the driving frequency. The full-width at half-maximum is given by the decay rate κ in the angular frequency. The average number of photons in the microwave resonator can be obtained from Eq. (2.19) by dividing with the photon energy $\hbar\omega_c$.

2.1.2 Reflection measurement

The response of the microwave cavity can be probed by shining monochromatic microwaves on the input port and measuring the reflected signal. The incoming microwaves impinging on C_{ex} are affected by the impedance mismatch between the 50Ω input line and the microwave cavity impedance with a coupling capacitance of C_{ex} in series. The reflection coefficient $\Gamma(\omega)$ describes the ratio between the input and output amplitudes as a function of the input signal frequency,

$$\Gamma(\omega) = \frac{Z(\omega) - Z_0}{Z(\omega) + Z_0}, \tag{2.20}$$

where $Z(\omega)$ is the impedance of the loaded microwave resonator and $Z_0 = 50\Omega$ is the impedance of the input line.

If the microwave resonator capacitance is being modulated by a mechanically vibrating capacitor element, we can write $C(t) = C_0 + \Delta C \cos(\omega_m t)$, where ω_m is the resonance frequency of the mechanically oscillating capacitance. Linearizing the expression for $\Gamma(\omega)$ in terms of mechanical displacement x leads to an oscillating reflection coefficient $\Gamma(\omega) = \Gamma_0(\omega) + \Delta\Gamma(\omega)\cos(\omega_m t)$. Probing the cavity with a monochromatic microwave at frequency ω, the reflected signal is

$$\begin{aligned} V_{\text{out}} =& \Gamma(\omega) V_{\text{in}} = \Gamma(\omega) V_1 \cos(\omega t) & (2.21) \\ =& V_1 \Gamma_0(\omega)\cos(\omega t) + \frac{1}{2} V_1 \Delta\Gamma(\omega) \left[\cos(\omega - \omega_m)t + \cos(\omega + \omega_m)t\right]. & (2.22) \end{aligned}$$

The first term is just the ordinary reflection from the microwave cavity, while the last two terms are the sidebands generated by the interaction between the probe tone and the mechanically modulated cavity frequency. The sideband amplitudes depend on the mechanical resonator amplitude A as

$$\Delta\Gamma(\omega) = \left.\frac{d\Gamma}{dC}\right|_{\omega} \frac{dC}{dx} A. \tag{2.23}$$

2.2 Optomechanical coupling

Thus far, the analysis has been classical. Next, we will review a full quantum calculation following [31]. The optomechanical coupling term given in Eq. (2.5) is a three-wave mixing term that includes the product of three operators. In the absence of losses, the equations of motion for the Heisenberg picture annihilation operators are

$$\begin{aligned} \dot{\hat{a}} =& - i\omega_c \hat{a} + i g_0 (\hat{b} + \hat{b}^\dagger)\hat{a} \\ \dot{\hat{b}} =& - i\omega_m \hat{b} + i g_0 \hat{a}^\dagger \hat{a}. \end{aligned}$$

The equations of motion are nonlinear due to the latter terms of each line and the optomechanical coupling in Eq. (2.5) is thus termed nonlinear coupling.

For references on how the full optomechanical coupling produces nonclassical cavity states as well as nonclassical resonator states, see Refs. [23] and [32], respectively. Naturally, with strong coupling, a nonclassical state can just be swapped to the mechanics if one can be prepared to the cavity with other means. If not, linear coupling produces only Gaussian states from Gaussian initial states [31].

2.3 Linearized coupling

The single-photon coupling strength g_0 in the optomechanical Hamiltonian Eq. (2.5) is small in the devices considered in this thesis. Especially, g_0 is small as compared to the decay rate of the microwave cavity. In Publication **I** for example, $g_0/2\pi = 40$Hz while the decay rate of the microwave cavity is $\kappa/2\pi = 6.2$MHz. Thus, it would seem that no effects of optomechanical coupling should be observable at the single photon/phonon level.

The form of the coupling term, however, suggests that increasing cavity occupation increases the coupling. The standard treatment is to linearize the coupling around the mean cavity occupation.

In terms of dimensionless position $\hat{q} = (\hat{b}^\dagger + \hat{b})/\sqrt{2}$ and momentum $\hat{p} = i(\hat{b}^\dagger - \hat{b})/\sqrt{2}$ operators for the mechanics, the system Hamiltonian can be written as [33]

$$\hat{H}_S = \hbar\omega_c\hat{a}^\dagger\hat{a} + \frac{1}{2}\left(\hat{p}^2 + \hat{q}^2\right) - \sqrt{2}\hbar g_0\hat{a}^\dagger\hat{a}\hat{q} + i\hbar E\left(\hat{a}^\dagger e^{-i\omega_d t} - \hat{a}e^{i\omega_d t}\right), \quad (2.24)$$

where $[\hat{q}, \hat{p}] = i$ and E is the strength of the cavity drive. In the input-output formalism (see App. B or [31] for a short introduction) and in the frame rotating with the drive, the equations of motion become

$$\dot{\hat{q}} = \omega_m\hat{p}, \quad (2.25)$$

$$\dot{\hat{p}} = -\omega_m\hat{q} + \sqrt{2}g_0\hat{a}^\dagger\hat{a} - \gamma_m\hat{p} + \xi, \quad (2.26)$$

$$\dot{\hat{a}} = -\left(\kappa/2 + i\Delta\right)\hat{a} + i\sqrt{2}g_0\hat{a}\hat{q} + E - \sqrt{\kappa}\hat{a}_{\text{in}}, \quad (2.27)$$

where γ_m is the decay rate of the mechanics, ξ is the noise term acting on the mechanical resonator [34], κ is the cavity photon decay rate, $\Delta = \omega_c - \omega_d$ is the detuning between the bare cavity frequency and the drive, and $\hat{a}_{\text{in}}$ describes the cavity inputs. Following the standard treatment, we linearize the equations of motion by writing the operators as sums of classical variables and quantum fluctuation operators,

$$\hat{q} = q_s + \delta\hat{q}, \tag{2.28}$$

$$\hat{p} = p_s + \delta\hat{p}, \tag{2.29}$$

$$\hat{a} = \alpha_s + \delta\hat{a}, \tag{2.30}$$

where the classical steady-state solutions are written with a subscript s. To solve these equilibrium values, we neglect all fluctuations in Eqs. (2.25-2.27) and set the time derivatives to zero ($\dot{q}_s = \dot{p}_s = \dot{\alpha}_s = 0$). This gives

$$p_s = 0, \tag{2.31}$$

$$q_s = \frac{\sqrt{2}g_0}{\omega_m}|\alpha_s|^2, \tag{2.32}$$

$$\alpha_s = \frac{E}{\kappa/2 + i(\Delta - \sqrt{2}g_0 q_s)} = \frac{E}{\kappa/2 + i\Delta_{\text{eff}}}. \tag{2.33}$$

Obviously, the last two equations constitute a third-order algebraic equation with up to three stationary solutions. The effective detuning is affected by the stationary radiation pressure and we have defined

$$\Delta_{\text{eff}} = \Delta - \frac{2g_0^2}{\omega_m}|\alpha_s|^2 = \omega_c - \omega_d - \frac{2g_0^2}{\omega_m}|\alpha_s|^2. \tag{2.34}$$

After the stationary terms have been taken into account, the remaining terms give the equations of motion for the fluctuation operators,

$$\dot{\delta\hat{q}} = \omega_m \delta\hat{p}, \tag{2.35}$$

$$\dot{\delta\hat{p}} = -\omega_m \delta\hat{q} - \gamma_m \delta\hat{p} + g\left(\delta\hat{a}^\dagger + \delta\hat{a}\right) + \xi, \tag{2.36}$$

$$\dot{\delta\hat{a}} = -\left(\kappa/2 + i\Delta_{\text{eff}}\right)\delta\hat{a} + ig\delta\hat{q} - \sqrt{\kappa}\hat{a}_{\text{in}}, \tag{2.37}$$

where the steady-state solution is taken to be real and the nonlinear terms $\delta\hat{a}^\dagger\delta\hat{a}$ and $\delta\hat{a}\delta\hat{q}$ are neglected since we assume $|\alpha_s| \gg 1$. We have also defined the cavity-enhanced optomechanical coupling g as

$$g = \sqrt{2}g_0\alpha_s = g_0\sqrt{\frac{2E^2}{(\kappa/2)^2 + \Delta_{\text{eff}}^2}}. \tag{2.38}$$

To summarize the linearization, the drive term is now taken into account in the coupling term g and the new equilibrium position of the mechanics is taken into account in the effective detuning Δ_{eff}.

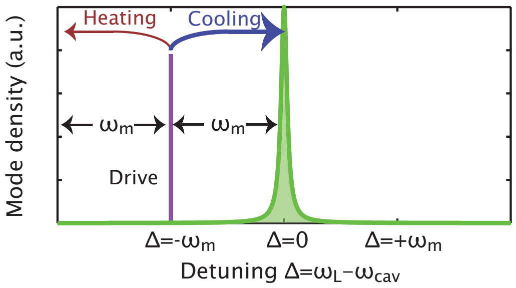

Fig. 2.4: Raman scattering picture of mechanical mode cooling. Cavity drive is optimally red-detuned below the cavity by the mechanical frequency. Scattering takes place upconverting the incoming photons into the cavity frequency by absorbing a phonon from the mechanical mode. The opposite Stokes-process also occurs but with a lot smaller probability in the sideband resolved regime ($\kappa \ll \omega_m$).

Linearized equations produce Gaussian states out of Gaussian initial states and inputs. Therefore, nonclassical states in the sense of negative Wigner distributions can not be attained. Linear equations, however, can describe many interesting phenomena including ground-state cooling, mechanical amplification, and normal-mode splitting. In the following sections, we concentrate on introducing the basic working principles of cooling, amplification, and multimode optomechanics with two mechanical resonators in the linearized regime.

2.3.1 Cooling

The cooling of mechanical mode is best explained in the frequency domain with a scattering approach (see Fig. 2.4). The previous classical analysis indicated that the coupling between the cavity and mechanics scatters photons that are entering the cavity both up and down in frequency. Photons that are red-detuned from the cavity frequency (photons that have a lower frequency) will preferentially be up-converted by absorbing a phonon from the mechanical mode. Due to the finite lifetime of the cavity, a finite density of modes also exists at $\omega - \omega_m$ to down-convert the incoming photon by releasing an extra phonon to the mechanics.

The scattering of incoming photons opens up a new dissipative channel for the mechanical mode in a case where the drive is red-detuned $\Delta_{\text{eff}} > 0$. The optomechanical cooling rate Γ_{opt} is given by the balance between the rate of emission

A^- and absorption A^+ of phonons [33, 35],

$$\Gamma_{\mathrm{opt}} = A^- - A^+ = \frac{2g^2}{\kappa}\frac{(4\omega_m)^2}{\kappa^2 + (4\omega_m)^2}, \tag{2.39}$$

where the last form is given for optimally red-detuned drive [36]. Therefore, the total mechanical damping rate is given by the sum of the intrinsic damping and the introduced optomechanical damping $\gamma_m^{\mathrm{eff}} = \gamma_m + \Gamma_{\mathrm{opt}}$. Classically, the additional dissipation channel would lower the mechanical resonator temperature to

$$T_f = T_i \frac{\gamma_m}{\gamma_m^{\mathrm{eff}}}, \tag{2.40}$$

where T_f is the final temperature and T_i is the initial temperature [31]. This classical expression, however, ceases to be valid close to the quantum ground state of mechanics. Quantum mechanical analyses were carried out in [35] and [36] in which the effective final occupation $\bar{n}_f$ was determined to be (in the limit $\kappa \gg \Gamma_{\mathrm{opt}}, g$ and $\omega_m \gg \gamma_m, g$)

$$\bar{n}_f = \bar{n}_i \frac{\gamma_m}{\gamma_m^{\mathrm{eff}}} + \frac{A^+}{\gamma_m^{\mathrm{eff}}}, \tag{2.41}$$

where $\bar{n}_i$ is the equilibrium thermal occupation of the mechanical mode and the scattering rates are given by [31]

$$A^{\pm} = \frac{g^2\kappa}{\kappa^2/2 + (\Delta_{\mathrm{eff}} \pm \omega_m)^2}. \tag{2.42}$$

In the case that the initial temperature is so large that $\bar{n}_i\gamma_m \gg A^+$, the classical limit Eq. (2.40) is obtained since the second term in Eq. (2.41) becomes negligible.

It is interesting to note that the classical expression anticipates no lower bound on final temperature, while the quantum mechanical treatment gives one. If the coupling to thermal bath is negligibly small ($\gamma_m \approx 0$) and drive is optimally detuned to $\Delta_{\mathrm{eff}} = \omega_m$, the competition between cooling and heating processes yields the minimum phonon number

$$\bar{n}_{f,\mathrm{min}} = \frac{A^+}{A^- - A^+} = \left(\frac{\kappa}{4\omega_m}\right)^2, \tag{2.43}$$

where we have assumed the resolved sideband regime $\kappa \ll \omega_m$. The above limit obviously allows ground-state cooling since the optomechanical cooling can dominate intrinsic damping if one simply drives the cavity with high enough power.

In the cooling experiments presented in Publication **II**, the minimum effective phonon number achieved was 1.8 quanta. Increasing the drive from this optimal cooling power began to heat up the mechanical mode. At the same time, the cavity occupation was observed to increase. In the above derivations, the cavity occupation was neglected. By taking the cavity occupation into account, the minimum phonon occupation is given by [31]

$$\bar{n}_{f,\min} = \bar{n}_i \frac{\gamma_m}{\gamma_m^{\text{eff}}} + \bar{n}_{\text{cav}} + \left(\frac{\kappa}{4\omega_m} \right)^2 , \tag{2.44}$$

where $\bar{n}_{\text{cav}}$ is the thermal occupancy of the cavity.

Thus, the mechanical mode can not reach lower occupation than the cavity to which it is coupled. This becomes a limitation with very strong cavity drive which heats up the whole cryostat due to the attenuators in the input line. The attenuators themselves are required to attenuate the thermal noise coming from the room temperature environment through the microwave lines.

The problem of heating the bath can be circumvented, for example, by using a multimode cavity [37]. A multimode cavity with the cavity mode spacing that is equal to the mechanical frequency ω_m allows driving the lower mode such that lower power is required for cooling, as compared to the single mode cavity case. The reverse process of heating the mechanical resonator is also enhanced such that $\bar{n}_{f,\min} = 9 \left(\frac{\kappa}{4\omega_m} \right)^2$. The ratio κ/ω_m can however be made so small that this limit is not too severe to prevent reaching the ground state.

2.3.2 Amplification

In the previous section, red-detuned cavity drive was shown to add dissipation to the mechanical mode. Equations (2.39) and (2.42) imply that in the case of blue-detuned cavity drive ($\Delta_{\text{eff}} < 0$), the optomechanical coupling decreases the total mechanical damping rate and heats the mechanics. It also turns out that the coupled system of cavity and mechanics acts as an amplifier in the blue-detuned drive regime, as we have shown in Publication **I**.

Linear single-mode amplifiers

To make the amplifier analysis more tractable, I review here concepts about linear amplifiers by following the treatment given by Carlton Caves [38].

For a single-mode linear amplifier, the output annihilation operator of the amplifier is connected to the input operators by

$$\hat{a}_{\text{out}} = M\hat{a}_{\text{in}} + L\hat{a}_{\text{in}}^{\dagger} + \hat{\mathcal{F}}, \tag{2.45}$$

where M and L are complex numbers, and $\hat{\mathcal{F}}$ is the noise operator that adds noise to the output of the amplifier independent of the input signals [39]. For the output operators to have the correct commutation relations ($[\hat{a}_{\text{out}}, \hat{a}_{\text{out}}^{\dagger}] = 1$), the terms have to be connected such that

$$1 = |M|^2 - |L|^2 + [\hat{\mathcal{F}}, \hat{\mathcal{F}}^{\dagger}]. \tag{2.46}$$

To study the properties of the amplifier, it is convenient to work with the input and output quadratures by writing

$$\hat{a}_{\text{in}} = \hat{X}_1 + i\hat{X}_2, \tag{2.47}$$

$$\hat{a}_{\text{out}} = \hat{Y}_1 + i\hat{Y}_2, \tag{2.48}$$

$$\hat{\mathcal{F}}_1 = 1/2(\hat{\mathcal{F}} + \hat{\mathcal{F}}^{\dagger}), \tag{2.49}$$

$$\hat{\mathcal{F}}_2 = -i/2(\hat{\mathcal{F}} - \hat{\mathcal{F}}^{\dagger}). \tag{2.50}$$

If both $M \neq 0$ and $L \neq 0$, the amplifier is phase-sensitive [38] and the amplifier output depends on the phase of the input. It is, however, always possible to rotate the complex amplitude planes of both input and output quadratures such that in the new quadratures ($\hat{\hat{X}}_1, \hat{\hat{X}}_2, \hat{\hat{Y}}_1, \hat{\hat{Y}}_2$), the output quadrature $\hat{\hat{Y}}_1$ depends only on the input quadrature $\hat{\hat{X}}_1$ and similarly for the other quadrature. Writing the amplifier evolution equation (2.45) in these so-called preferred quadratures yields

$$\hat{\hat{Y}}_1 = (|M| + |L|)\hat{\hat{X}}_1 + \hat{\hat{\mathcal{F}}}_1, \tag{2.51}$$

$$\hat{\hat{Y}}_2 = (|M| - |L|)\hat{\hat{X}}_1 + \hat{\hat{\mathcal{F}}}_2. \tag{2.52}$$

Now the gain for the preferred quadratures can be conveniently defined in the units of number of quanta as

$$G_1 = (|M| + |L|)^2, \tag{2.53}$$

$$G_2 = (|M| - |L|)^2. \tag{2.54}$$

To characterize the noise added by the amplifier, we write down the uncertainties of the output in the preferred quadratures as

$$\left(\Delta\hat{\hat{Y}}_i\right)^2 = G_i\left(\Delta\hat{\hat{X}}_i\right)^2 + \left(\Delta\hat{\hat{\mathcal{F}}}_i\right)^2, \tag{2.55}$$

where the second term is the noise added by the amplifier. This added noise depends on the internal state of the amplifier, as will also be the case with the mechanical amplifier considered next. We can now define the added noise number for each preferred quadrature as

$$A_i = \left(\Delta \hat{\tilde{\mathcal{F}}}_i\right)^2 / G_i. \tag{2.56}$$

The added noise numbers are fundamentally limited by quantum mechanics [38]

$$\sqrt{A_1 A_2} \geq \frac{1}{4} \left| 1 - \frac{1}{\sqrt{G_1 G_2}} \right|. \tag{2.57}$$

Application

To analyze the amplification and the added noise, we slightly modify the standard equations of motion (Eqs. (2.35)-(2.37)) and separate the cavity bath to external bath acting through the input/output port and to internal bath such that

$$\delta\dot{\hat{a}} = -\left(\kappa/2 + i\Delta_{\text{eff}}\right)\delta\hat{a} + ig\delta\hat{q} - \sqrt{\kappa_{\text{int}}}\hat{a}_{\text{in}}^{\text{int}} - \sqrt{\kappa_{\text{ext}}}\hat{a}_{\text{in}}^{\text{ext}}, \tag{2.58}$$

where $\kappa = \kappa_{\text{int}} + \kappa_{\text{ext}}$. The input term $\hat{a}_{\text{in}}^{\text{ext}}$ is composed of the coherent input signal into the cavity (the probe tone to be amplified) and incoherent noise from the transmission line. The coherent pump is already taken into account in the stationary solution through the term E. The input term $\hat{a}_{\text{in}}^{\text{int}}$ is associated to the internal losses. According to input-output theory with two baths, the output is related to the input by (see App. B)

$$\hat{a}_{\text{out}} = \hat{a}_{\text{in}} + \sqrt{\kappa_{\text{ext}}}\hat{a}_{\text{in}}^{\text{ext}}. \tag{2.59}$$

In the supplementary material of Publication **I**, the equations of motion, Eqs. (2.35), (2.36), and (2.58), were solved in frequency space to give the output field

$$\begin{aligned} \hat{a}_{\text{out}}^{\text{ext}}(\omega) =& M(\omega)\hat{a}_{\text{in}}^{\text{ext}}(\omega) + L(\omega)\, \hat{a}_{\text{in}}^{\text{ext}\,\dagger}(\omega) \\ &+ \underbrace{M_I(\omega)\hat{a}_{\text{in}}^{\text{int}}(\omega) + L_I(\omega)\, \hat{a}_{\text{in}}^{\text{int}\,\dagger}(\omega) + Q(\omega)\xi(\omega)}_{\hat{\mathcal{F}}}. \end{aligned} \tag{2.60}$$

The full expressions of the terms are lengthy and can be found in the abovementioned supplementary material of Publication **I**. The three terms on the second line represent the noise added by the amplifier. The added noise clearly depends on the internal state of the amplifier through the mechanical bath temperature due to the term $\xi(\omega)$. With optimal coupling, the product of added noises gives

$$2\sqrt{A_1 A_2} \simeq \frac{\kappa_{\text{int}}}{\kappa}\left(\bar{n}_{\text{cav}} + \frac{1}{2}\right) + \frac{\kappa}{\kappa_{\text{ext}}}\left(\bar{n}_i + \frac{1}{2}\right) \geq \frac{1}{2}. \tag{2.61}$$

The mechanical amplifier can therefore operate as a quantum-limited linear amplifier in a case where the mechanics can be cooled to the ground state and the internal losses of the cavity are negligible as compared to the external ones.

2.3.3 Multimode optomechanics

So far in our treatment we have mainly considered only a single cavity mode and a single mechanical mode. Only in passing have we mentioned the possibility of using two cavity modes for cooling [37]. Even in the basic setups considered in this thesis, the electrical microwave cavity has many equispaced modes and the mechanical resonator has a multitude of modes with different coupling strengths to the cavity. Usually, however, it is appropriate to consider only a pair of these since the cavity modes and mechanical modes are well separated in frequency and the coupling is induced by the appropriate cavity drive around one cavity resonance. If the mechanical modes are separated from each other by more than their effective linewidth, the driven system can be approximated by a single cavity mode and a single mechanical mode.

In Publication **II**, the device is designed such that microwave cavity is coupled to two mechanical resonators with closely spaced resonance frequencies. The linearization of equations of motion proceeds similarly to the case of one mechanical resonator and the linearized equations of motion read

$$\begin{aligned}
\delta\dot{\hat{a}} =& -\left(\kappa/2 + i\Delta_{\text{eff}}\right)\delta\hat{a} + ig_1\delta\hat{q}_1 + ig_2\delta\hat{q}_2 - \sqrt{\kappa}\hat{a}_{\text{in}}, && (2.62)\\
\delta\dot{\hat{q}}_1 =& \omega_1\delta\hat{p}_1, && (2.63)\\
\delta\dot{\hat{q}}_2 =& \omega_2\delta\hat{p}_2, && (2.64)\\
\delta\dot{\hat{p}}_1 =& -\omega_1\delta\hat{q}_1 - \gamma_1\delta\hat{p}_1 + g_1\left(\delta\hat{a}^\dagger + \delta\hat{a}\right) + \xi_1, && (2.65)\\
\delta\dot{\hat{p}}_2 =& -\omega_2\delta\hat{q}_2 - \gamma_2\delta\hat{p}_2 + g_2\left(\delta\hat{a}^\dagger + \delta\hat{a}\right) + \xi_2, && (2.66)
\end{aligned}$$

where the mechanical resonator parameters are denoted with subindices 1 and 2. Anticipating the emergence of a dark mode [40] which does not couple to the cavity and two bright modes which have a cavity component, we re-express the equations of motions in basis of symmetric and antisymmetric combinations of resonator positions, weighted by their optomechanical coupling,

$$\begin{aligned}
\hat{q}_s =& \frac{g_1\delta\hat{q}_1 + g_2\delta\hat{q}_2}{g_1 + g_2}, && (2.67)\\
\hat{q}_a =& \frac{g_2\delta\hat{q}_1 - g_1\delta\hat{q}_2}{g_1 + g_2}, && (2.68)\\
\hat{p}_s =& \frac{g_1 + g_2}{g_1^2 + g_2^2}\left(g_1\delta\hat{p}_1 + g_2\delta\hat{p}_2\right), && (2.69)\\
\hat{p}_a =& \frac{g_1 + g_2}{g_1^2 + g_2^2}\left(g_2\delta\hat{p}_1 - g_1\delta\hat{p}_2\right), && (2.70)
\end{aligned}$$

which fulfill the canonical commutation relations $[\hat{q}_s, \hat{p}_s] = [\hat{q}_a, \hat{p}_a] = i$ and $[\hat{q}_s, \hat{p}_a] = [\hat{q}_a, \hat{p}_s] = 0$. The equations of motion become

$$\delta\dot{\hat{a}} = -\left(\kappa/2 + i\Delta_{\text{eff}}\right)\delta\hat{a} + i\left(g_1 + g_2\right)\hat{q}_s - \sqrt{\kappa}\hat{a}_{\text{in}}, \tag{2.71}$$

$$\dot{\hat{q}}_s = \omega_\Sigma \frac{g_1^2 + g_2^2}{\left(g_1 + g_2\right)^2}\hat{p}_s + \omega_\Delta \frac{g_1^2 - g_2^2}{\left(g_1 + g_2\right)^2}\hat{p}_s + \omega_\Delta \frac{2g_1g_2}{\left(g_1 + g_2\right)^2}\hat{p}_a, \tag{2.72}$$

$$\dot{\hat{q}}_a = \omega_\Sigma \frac{g_1^2 + g_2^2}{\left(g_1 + g_2\right)^2}\hat{p}_a + \omega_\Delta \frac{g_2^2 - g_1^2}{\left(g_1 + g_2\right)^2}\hat{p}_a + \omega_\Delta \frac{2g_1g_2}{\left(g_1 + g_2\right)^2}\hat{p}_s, \tag{2.73}$$

$$\begin{aligned}\dot{\hat{p}}_s = &- \omega_\Sigma \frac{\left(g_1 + g_2\right)^2}{g_1^2 + g_2^2}\hat{q}_s - \omega_\Delta \left(g_1^2 - g_2^2\right)\frac{\left(g_1 + g_2\right)^2}{\left(g_1^2 + g_2^2\right)^2}\hat{q}_s \\ &- \omega_\Delta 2g_1g_2 \frac{\left(g_1 + g_2\right)^2}{\left(g_1^2 + g_2^2\right)^2}\hat{q}_a - \gamma\hat{p}_s + \left(g_1 + g_2\right)\left(\delta\hat{a}^\dagger + \delta\hat{a}\right),\end{aligned} \tag{2.74}$$

$$\begin{aligned}\dot{\hat{p}}_a = &- \omega_\Sigma \frac{\left(g_1 + g_2\right)^2}{g_1^2 + g_2^2}\hat{q}_a - \omega_\Delta \frac{\left(g_1 + g_2\right)^2\left(g_1^2 - g_2^2\right)}{\left(g_1^2 + g_2^2\right)^2}\hat{q}_a, \\ &- \omega_\Delta 2g_1g_2 \frac{\left(g_1 + g_2\right)^2}{\left(g_1^2 + g_2^2\right)^2}\hat{q}_s - \gamma\hat{p}_a\end{aligned} \tag{2.75}$$

where $\omega_\Sigma = (\omega_1 + \omega_2)/2$, $\omega_\Delta = (\omega_1 - \omega_2)/2$. We have set $\gamma = \gamma_1 = \gamma_2$ to simplify the equations and have neglected the mechanical fluctuations, $\xi_i = 0$.

Even though the general equations (Eqs. (2.71)-(2.75)) are complicated, we can easily see a few aspects. The antisymmetric mode is coupled to the evolution of the cavity only via the symmetric mode. If the mechanical resonators are degenerate, $\omega_\Delta = 0$, the antisymmetric mode becomes independent of the cavity and vice versa. The mode, thus, does not decay via the cavity and it is therefore termed the dark mode. The mode has a slow decay rate determined by γ which usually is orders of magnitude slower than the cavity decay rate.

In practice, the resonators are never exactly degenerate. To gain more insight into what happens in the limit where coupling is increased with cavity driving, we consider the case $g = g_1 = g_2$ and the equations simplify to

$$\delta\dot{\hat{a}} = -\left(\kappa/2 + i\Delta_{\text{eff}}\right)\delta\hat{a} + 2ig\hat{q}_s - \sqrt{\kappa}\hat{a}_{\text{in}}, \tag{2.76}$$

$$\dot{\hat{q}}_s = \frac{\omega_\Sigma}{2}\hat{p}_s + \frac{\omega_\Delta}{2}\hat{p}_a, \tag{2.77}$$

$$\dot{\hat{q}}_a = \frac{\omega_\Sigma}{2}\hat{p}_a + \frac{\omega_\Delta}{2}\hat{p}_s, \tag{2.78}$$

$$\dot{\hat{p}}_s = -2\omega_\Sigma\hat{q}_s - 2\omega_\Delta\hat{q}_a - \gamma\hat{p}_s + 2g\left(\delta\hat{a}^\dagger + \delta\hat{a}\right), \tag{2.79}$$

$$\dot{\hat{p}}_a = -2\omega_\Sigma\hat{q}_a - 2\omega_\Delta\hat{q}_s - \gamma\hat{p}_a. \tag{2.80}$$

These equations are solved in the supplementary material of Publication **II**. For the case of strong coupling ($\omega_\Delta \ll g$) and optimally red-detuned cavity drive ($\Delta_{\text{eff}} = \omega_\Sigma$) they yield the eigenfrequencies

$$\omega_{\text{bright}} = \omega_\Sigma \tag{2.81}$$

$$\omega_{\text{dark}\pm} = \Delta_{\text{eff}} - i\frac{\kappa}{4} \pm \sqrt{g^2 - \left(\frac{\kappa}{4}\right)^2}. \tag{2.82}$$

The eigenmode corresponding to the eigenvalue ω_{bright} has contributions from the symmetric mechanical mode and the cavity mode going asymptotically to zero as the g/ω_Δ is increased. The lack of cavity component attributes this mode as the dark mode. The other two modes, $\omega_{\text{dark}\pm}$, are the bright modes which asymptotically decouple from the antisymmetric mechanical mode.

The threshold $g = \kappa/4$ can be recognized as the usual onset of normal-mode splitting [11, 17] and serves as a reasonable definition of the strong coupling regime. For $g > \kappa/4$ the roots of $\omega_{\text{dark}\pm}$ become real and the splitting becomes observable.

Chapter 3

Coupling a qubit to a mechanical resonator

The theory described in the previous chapter concerns optomechanics in the regime where the interaction between the mechanical resonator and the cavity is linear. As mentioned earlier, such linear interaction between two harmonic oscillators can only create Gaussian states out of Gaussian inputs. In this chapter, we will concentrate on mechanical resonators coupled to inherently nonlinear systems, that is, to quantum two-level systems realized as superconducting quantum bits (qubits). The nonlinearity of a qubit allows nonclassical states to be created and the subsequent coupling to mechanics then enables state transfer of these nonclassical states to mechanics. In addition, a qubit can also be used to measure the quantum state of the mechanics.

3.1 Superconducting qubits

Consider a small piece of superconducting metal with total capacitance C. The metal island is coupled to a nearby voltage gate with capacitance C_g which allows for the electrostatic energy of the island to be tuned by applying a gate voltage V_g. The energy required to add one Cooper pair, with charge $2e$, to the island is given by $4E_C$, where [41]

$$E_C = \frac{e^2}{2C}, \tag{3.1}$$

which is called the (single electron) charging energy, see App. C. The total electrostatic energy of the island, E_{ch}, is

$$E_{\text{ch}} = 4E_C(n - n_g)^2, \tag{3.2}$$

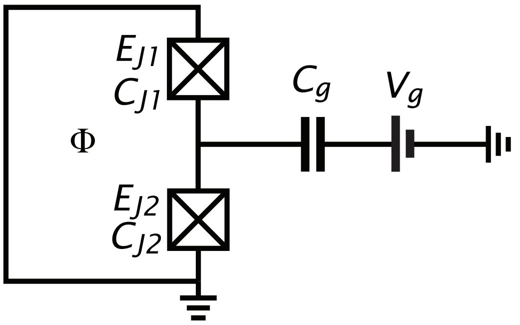

Fig. 3.1: Circuit diagram of a Cooper pair box coupled with capacitance C_g to a voltage source V_g. The Josephson junctions are denoted with boxed crosses with Josephson energies E_J and capacitance C_J. The magnetic flux through the loop is Φ. The system depicted here is tunable with two junctions and a loop. In the text, a simplified circuit with one junction is considered. A schematic diagram of such a circuit can be found in the appendix, see Fig. C.1.

where n is the number of excess Cooper pairs on the island with $n = 0$ corresponding to an electrically neutral island. $n_g = C_g V_g/2e$ is the dimensionless gate charge normalized to units of Cooper pairs. While the number of Cooper pairs on the island is quantized, the charge induced by the gate voltage and n_g are continuous parameters [42].

We have not yet introduced any practical means of manipulating the number of Cooper pairs on the island. In the following, we shall consider a superconducting island which in addition to the gate is coupled to a superconducting electrode with a Josephson junction [43], see Fig. 3.1. The Hamiltonian for such a system, coined the Cooper pair box, is given by [44]

$$\hat{H}_{\text{CPB}} = 4E_C(\hat{n} - n_g)^2 - E_J \cos\hat{\varphi}, \tag{3.3}$$

where $\hat{n}$ is now the Cooper pair number operator for the island. $\hat{\varphi}$ is the order parameter phase difference across the junction and E_J is the Josephson energy that describes the coupling to the electrode. It is related to the normal state resistance by the Ambegaokar-Baratoff relation [45]

$$E_J = \frac{\hbar}{2e}\frac{\pi\Delta(T)}{2eR_n}\tanh\left[\frac{\Delta(T)}{2k_B T}\right], \tag{3.4}$$

where $\Delta(T)$ is the BCS energy gap at temperature T. For temperatures far below the superconducting transition temperature T_c, we can use $\Delta(0) = 1.76 k_B T_c$. In this thesis, only aluminum is used for which T_c = 1.2 K [46].

The number of cooper pairs on the island $\hat{n}$ and the phase on the island $\hat{\phi}$ are conjugate variables with each other. Similarly the number of Cooper pairs passed through a junction and the phase across it are conjugate variables [42]. Equating the number of Cooper pairs on the island and the Cooper pairs passed through the junction, we can express $E_J \cos\hat{\varphi}$ in the Cooper pair basis. Cooper pair basis states satisfy $\hat{n}|n\rangle = n|n\rangle$ and in this basis the Hamiltonian reads

$$\hat{H}_{\mathrm{CPB}} = 4E_C(\hat{n} - n_g)^2 - E_J/2 \sum_n \left(|n\rangle\langle n+1| + |n+1\rangle\langle n|\right). \tag{3.5}$$

The Hamiltonian for the Cooper pair box in Eq. (3.5) underlines the fact that it is the Josephson coupling which allows the tunneling of Cooper pairs in and out of the island.

3.1.1 Charge qubit

Now that a new energy scale E_J is introduced into the system, the eigenstates are modified and the convenient basis to work with is the Cooper pair box eigenbasis. Let us first consider the so-called charge-qubit regime where the Josephson coupling is very small, $E_J \ll E_C$, and assume that the temperature is sufficiently low such that no thermal excitations take place $k_B T \ll E_J \ll E_C$. Therefore, the energy required to add extra Cooper pairs on to the island is larger than the thermal fluctuations can provide. The Coulomb blockade also ensures the non-linearity of the island transitions, thus enabling it to be used as a qubit at low enough temperatures. The qubit eigenstates are the simple Cooper pair states apart from the degeneracy points where the tunnel coupling mixes the two states.

When restricted to gate charge values $n_g \in [0, 1]$, the time-evolution given by the Hamiltonian in Eq. (3.5) can be restricted to two states $|0\rangle$ and $|1\rangle$,

$$\hat{H} = -2E_C(1 - 2n_g)\hat{\sigma}_z - \frac{E_J}{2}\hat{\sigma}_x. \tag{3.6}$$

A schematic energy diagram of the two lowest eigenstates $|0\rangle$ and $|1\rangle$ is plotted in Fig. 3.2.

3.1.2 Transmon

In the last section, we considered a Cooper pair box with a small tunnel coupling with respect to the charging energy. This implied that the eigenstates of the system were only mildly modified by the tunneling interaction, apart from the degeneracy points. This enabled us to restrict the evolution to only two Cooper

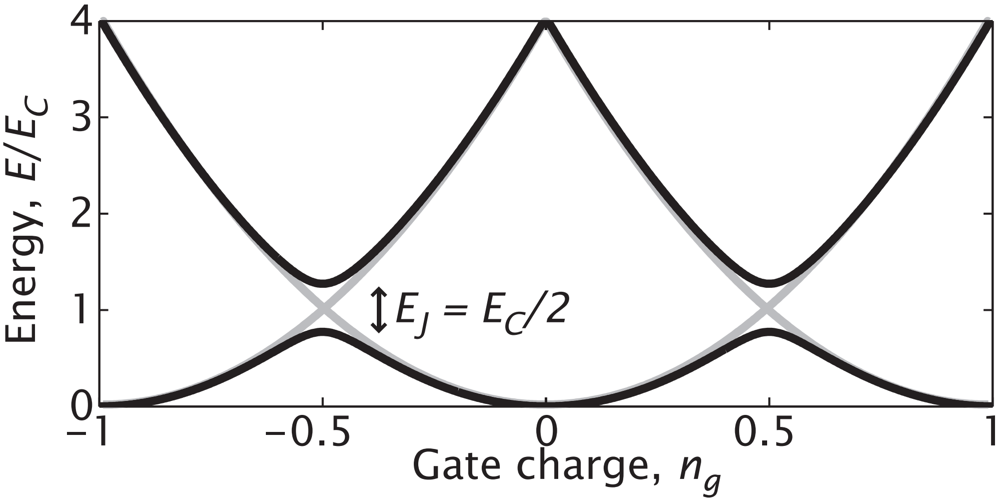

Fig. 3.2: Energy diagram of the lowest two Cooper pair box states (black) and uncoupled Cooper pair states (gray). Josephson coupling introduces anticrossings at the degeneracy points at half-integer gate charge values with the energy gap equal to the Josephson energy E_J. Josephson energy is set to half of the single-electron charging energy, $E_J = E_C/2$.

pair states for which analytical results were easy to derive and provided intuitive picture of the coupling to mechanics.

Charge-qubit devices [47] have suffered from very short dephasing times which means that the energy splitting between the two lowest eigenstates is very unstable in a real-world experiments. As figure 3.4 shows, the slowly fluctuating electric fields couple longitudinally to the qubit and degrade the phase coherence between the ground and excited state. This problem can be alleviated by working at the "sweet spot" of gate charge where the dispersion curve is flat and no longitudinal coupling to fluctuators exist, namely $n_g = 0.5$.

The sweet spot alone has not rendered charge qubits coherent enough for certain applications, even though it has to be noted that very long energy relaxation times (of order tens of microseconds) can now be reached with such devices [48]. As we noted in the last section, at the degeneracy point the tunnel coupling modified the eigenstates such that gate charge modulations coupled transversely to the qubit instead of the detrimental longitudinal coupling. The slow charge fluctuations are unable to excite the qubit and the coherence of the qubit is improved. This type of approach was used to develop the charge insensitive version of charge qubit, transmon, for which the E_J/E_C ratio is much higher and the eigenstates are not simple Cooper pair states. In this section, I will review the essential properties of transmon qubits following mostly Ref. [49].

As noted above, increasing the E_J/E_C ratio reduces the coupling of charge fluctuations to $\hat{\sigma}_z$ component of the qubit, which is essentially the same as suppressing the charge dispersion of the qubit transition. The peak-to-peak value of the mth qubit eigenstate ($m = 0, 1, 2, \ldots$) as a function of the gate charge, $|\epsilon_m|$, is exponentially suppressed as a function of E_J/E_C. In the limit $E_J/E_C \gg 1$, this can be approximated as

$$|\epsilon_m| = E_C \frac{2^{4m+5}}{m!} \sqrt{\frac{2}{\pi}} \left(\frac{E_J}{2E_C} \right)^{\frac{m}{2}+\frac{3}{4}} e^{-\sqrt{8E_J/E_C}}. \tag{3.7}$$

To get an idea of protection against charge noise, this can be compared to a charge qubit operated at the gate charge sweet point $n_g = 0.5$ where only the second order derivative with respect to n_g remains. Equation (3.6) implies that the transition energy is given by

$$E_{01} = \sqrt{16E_C^2(1 - 2n_g)^2 + E_J^2}, \tag{3.8}$$

giving

$$\left. \frac{\partial^2 E_{01}}{\partial n_g^2} \right|_{n_g=\frac{1}{2}} = \frac{(8E_C)^2}{E_J}. \tag{3.9}$$

In the limit of high E_J/E_C ratio, the dependency of eigenstate energy on gate charge is sinusoidal and the maximum of the second order derivative is given by

$$\frac{\partial^2 E_{01}}{\partial n_g^2} = 2\pi^2(|\epsilon_1| - |\epsilon_0|). \tag{3.10}$$

For $E_J/E_C = 0.1$, Eq. (3.9) gives $640E_C$ while for $E_J/E_C = 50$ Eq. (3.10) gives $9.4 \times 10^{-4} E_C$. The transition frequency E_{01} of such a transmon-regime qubit is therefore five orders of magnitude less sensitive at an arbitrary gate charge point as compared to the charge qubit operated at the gate charge sweet spot.

In terms of charge dispersion, it would be beneficial to increase the E_J/E_C ratio to arbitrarily large values. However, it turns out that the system eigenlevels become more and more equispaced as the ratio grows. Eventually the time-domain control pulses would also start to excite the E_{12} transition and the system would no longer be operable as a simple two-level system. Approximative expressions for the eigenenergies can be derived by expanding the transmon Hamiltonian in

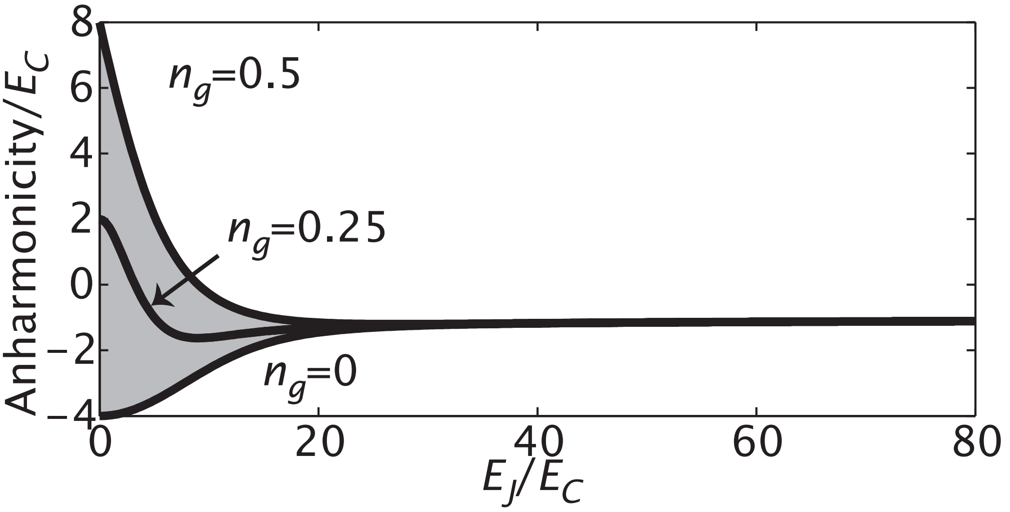

Fig. 3.3: Anharmonicity, $E_{12} - E_{01}$, of the lowest two qubit transitions as a function of the E_J/E_C ratio and normalized with the charging energy. As expected from the analytical approximation, the system never becomes completely harmonic but the anharmonicity determined by the charging energy remains.

the superconducting phase difference up to the fourth order [49], which, for the mth eigenstate energy, gives

$$E_m \simeq -E_J + \sqrt{8E_C E_J}\left(m + \frac{1}{2}\right) - \frac{E_C}{12}(6m^2 + 6m + 3). \qquad (3.11)$$

For transition frequencies, this approximation thus gives $E_{n-1,n} \simeq \sqrt{8E_C E_J} - nE_C$ which has the anharmonicity correction as compared to the Josephson plasma frequency, see Eq. (3.14). The absolute anharmonicity between any adjacent transitions is thus $E_{12} - E_{01} \simeq -E_C$. The numerically computed absolute anharmonicity between the first two transitions is plotted in Fig. 3.3.

Based on the absolute anharmonicity, we can obtain the minimum control pulse duration by considering the spread of Fourier transform of the pulse $\tau \sim 1/E_C$. For a typical control pulse width of ten nanoseconds, this gives $E_C/h = 100$ MHz corresponding to a capacitance of 200 fF. From this point of view, it would be advantageous to keep E_C at this minimum value and use as high E_J as allowed by the microwave wiring and equipment. However, using very high capacitance compromises the mechanical coupling, as we will see from Eq. (3.28), as the divider gets large.

As noted above, the effects of charge noise can be suppressed by increasing the E_J/E_C ratio. Since the qubit is to be operated at the cryostat base temperature around 25 mK, it is good to keep the qubit transition frequency $\omega_a/2\pi$ above $\gtrsim$4 GHz such that the qubit can be initialized and that thermal fluctuations do not decohere the qubit evolution. On the other hand, frequencies higher than 10 GHz start to become more difficult to manage without dedicated equipment. Therefore, the Josephson energy has to be increased simultaneously as the charging energy is reduced.

To get a rough estimate of how the qubit transition frequency depends on these parameters, we consider the following coarse model which forces the qubit to be interpreted as an LC resonator. The resonant frequency of such a harmonic oscillator is

$$\frac{\omega}{2\pi} = \frac{1}{2\pi}\frac{1}{\sqrt{LC}}. \tag{3.12}$$

The Josephson junction can be viewed as a nonlinear inductor whose inductance L_J depends on the order parameter phase difference φ across the junction

$$L_J(\varphi) = \left(\frac{\Phi_0}{2\pi}\right)^2 \frac{1}{E_J \cos\varphi}, \tag{3.13}$$

where Φ_0 is the magnetic flux quantum. Taking $L_J(0)$ and using the definition of the charging energy yields

$$\frac{\omega}{2\pi} = \frac{\sqrt{8E_J E_C}}{h}, \tag{3.14}$$

which is known as the Josephson plasma frequency [50].

Aiming for $\omega_a/2\pi = 5$ GHz and an E_J/E_C ratio of 20, implies a charging energy $E_C/h = 400$ MHz which corresponds roughly to 50 fF. The required Josephson energy translates into the normal state resistance of an aluminum junction (see Eq. (3.4))

$$R_n = \frac{k_B}{3.8e^2(E_J/h)}, \tag{3.15}$$

giving $R_n = 18$ kΩ.

The model discussed above forces the circuit to be treated as a harmonic oscillator for which the level spacing is constant for all transitions. As we will see, increasing the E_J/E_C ratio reduces the anharmonicity and we expect the model to work better in this regime.

We also found out that the capacitance required ($\sim$ 50 fF) is an order of magnitude larger than the capacitance of a small (100 × 100 nm^2) tunnel junction. To measure the state of such an island whose eigenstates are not Cooper pair states anymore, read-out schemes that detect electrical charge differences are not suitable. Therefore, an on-chip electrical cavity [51, 52] (or 3d cavity [53, 54]) is used. In the following, we consider the coupling to this type of cavity and the read-out of the qubit state.

3.1.3 Qubit read-out

The benefits of a higher E_J/E_C ratio in qubits was first utilized in the design of the quantronium [55]. The read-out problem of these high E_J/E_C devices was solved by introducing an on-chip cavity for read-out. In the scheme, the qubit island is capacitively coupled to an electrical cavity for reading out the qubit state [56]. In planar transmon designs, this can be implemented by fabricating the qubit next to the center strip of a coplanar waveguide (CPW) resonator [52] or microstrip resonator [57]. The voltage oscillations of the CPW resonator couple to the gate charge of the qubit and hence to maximize the coupling, the qubit is placed at the voltage antinode of the resonator mode with which it is to be coupled. The resonator can be modeled by an LC resonator [51] and quantized yielding the coupling [49]

$$\hat{H}_c = \hbar g'(\hat{n} - n_g)(\hat{a} + \hat{a}^\dagger), \tag{3.16}$$

where $g' = 2\beta e V^0_{\mathrm{rms}}/\hbar$. β is the fraction of qubit capacitance to CPW resonator C'_g divided by the total capacitance of the qubit, $\beta = C'_g/C_\Sigma$. $V^0_{\mathrm{rms}} = \sqrt{\hbar\omega_r/C_r}$ is the rms of vacuum voltage fluctuations between the center strip of the CPW resonator and ground plane, where ω_r is the resonant frequency of the CPW resonator mode and C_r is the total capacitance of the cavity.

As expected, the coupling between the qubit and mechanics, see Eq. (3.27), is of the exactly the same form as the coupling between the qubit and the cavity in Eq. (3.16). Therefore, both in the charge-qubit limit at the gate charge sweet spot as well as in the transmon regime, the coupling is transversal in the qubit eigenbasis. The energy non-conserving terms $\hat{a}\hat{\sigma}_-$ and $\hat{a}^\dagger\hat{\sigma}_+$ can be neglected if the coupling is not in the ultrastrong regime $g'_x/\omega_r \gtrsim 0.1$ [58, 59]. Neglecting these rapidly rotating terms corresponding to exciting and de-exciting the qubit and cavity simultaneously, the total Hamiltonian can be written as

$$\hat{H} = \hbar\omega_a\frac{\hat{\sigma}_z}{2} + \hbar\omega_r\hat{a}^\dagger\hat{a} + \hbar g'_x(\hat{a}^\dagger\hat{\sigma}_- + \hat{a}\hat{\sigma}_+) + \hbar\left(e_d(t)\hat{a}^\dagger e^{-i\omega_d t} + e^*_d(t)\hat{a}e^{i\omega_d t}\right), \tag{3.17}$$

where the last term is the measurement tone applied to the CPW resonator input with amplitude $e_d(t)$ and frequency ω_d. The first three terms of the Hamiltonian constitute the famous Jaynes-Cummings Hamiltonian.

To minimize the effects of the cavity on the qubit (e.g. Purcell effect [60]), the measurement of the qubit is often done in the limit of large detuning between the qubit and the cavity, $|\Delta| = |\omega_a - \omega_r| \ll g_x'$. In this so-called dispersive limit, the Jaynes-Cummings Hamiltonian can be diagonalized in the first order of parameter g_x'/Δ with a Schrieffer-Wolff transformation [61, 49]. Denoting the unitary transformation of the basis by

$$\hat{U} = e^{\hat{S}}, \tag{3.18}$$

where $\hat{S}$ is an antihermitian operator and separating the Jaynes-Cummings Hamiltonian into two parts, $\hat{H} = \hat{H}_0 + \hat{H}_1$

$$\hat{H}_0 = \hbar\omega_a \frac{\hat{\sigma}_z}{2} + \hbar\omega_r \hat{a}^\dagger \hat{a} \tag{3.19}$$

$$\hat{H}_1 = \hbar g_x' (\hat{a}^\dagger \hat{\sigma}_- + \hat{a}\hat{\sigma}_+). \tag{3.20}$$

The transformed Hamiltonian is given by a series using Baker-Hausdorff relation

$$\begin{aligned}\tilde{H} &= e^{\hat{S}} \hat{H} e^{-\hat{S}} = \hat{H} + \left[\hat{S}, \hat{H}\right] + \frac{1}{2!}\left[\hat{S}, \left[\hat{S}, \hat{H}\right]\right] + \ldots \qquad (3.21)\\ &= \hat{H}_0 + \hat{H}_1 + \left[\hat{S}, \hat{H}_0\right] + \left[\hat{S}, \hat{H}_1\right] + \frac{1}{2}\left[\hat{S}, \left[\hat{S}, \hat{H}_0\right]\right] + \frac{1}{2}\left[\hat{S}, \left[\hat{S}, \hat{H}_1\right]\right] + \mathcal{O}(\hat{S}^3).\end{aligned}$$

Choosing $\hat{S}$ such that it eliminates $\hat{H}_1$ in the first order leads to the requirement $\left[\hat{S}, \hat{H}_0\right] = -\hat{H}_1$. Thus,

$$\begin{aligned}\tilde{H} &= \hat{H}_0 + \left[\hat{S}, \hat{H}_1\right] - \frac{1}{2}\left[\hat{S}, \hat{H}_1\right] + \frac{1}{2}\left[\hat{S}, \left[\hat{S}, \hat{H}_1\right]\right] + \mathcal{O}(\hat{S}^3)\\ &= \hat{H}_0 + \frac{1}{2}\left[\hat{S}, \hat{H}_1\right] + \mathcal{O}(\hat{S}^2).\end{aligned} \tag{3.22}$$

Choosing $\hat{S} = -g_x'/\Delta(\hat{a}^\dagger \hat{\sigma}_- - \hat{a}\hat{\sigma}_+)$ fulfills $\left[\hat{S}, \hat{H}_0\right] = -\hat{H}_1$ and gives

$$\hat{H}_{\text{eff}} = \hat{H}_0 + \frac{1}{2}\left[\hat{S}, \hat{H}_1\right] = \hbar\omega_a \frac{\hat{\sigma}_z}{2} + \hbar\omega_r \hat{a}^\dagger \hat{a} + \hbar\chi \left(\hat{a}^\dagger \hat{a} + \frac{1}{2}\right) \hat{\sigma}_z, \tag{3.23}$$

where $\chi = g_x'^2/\Delta$ and the zero point of energy has been shifted by $-1/2\hbar\chi$. Equation (3.23) indicates that the state of the qubit shifts the frequency of the resonator by $\Delta\omega_r = \pm\hbar\chi$ thus allowing for the qubit read-out. On the other hand, the qubit transition frequency depends on the number of photons in the cavity, a phenomenon known as the Stark shift [62, 63]. In the case of a transmon, one should include the effect of the third state to derive the correct shift

χ, see [49]. The dispersive Hamiltonian can be also diagonalized exactly [64] which becomes necessary if the second order terms start to play a role. The effective Hamiltonian given here is sufficient if $n \ll n_{\text{crit}} = \Delta^2/4g_x'^2$. In the new basis, the driving term in Eq. (3.17) is transformed into effective driving

$$\begin{aligned}\hat{H}_{d,\text{eff}} = e^{\hat{S}}\hat{H}_d e^{-\hat{S}} =& \hbar \left(e_d(t)\hat{a}^\dagger e^{-i\omega_d t} + e_d^*(t)\hat{a}e^{i\omega_d t}\right) \\ &+\hbar\frac{g_x'}{\Delta}\left(e_d(t)\hat{\sigma}_+ e^{-i\omega_d t} + e_d^*(t)\hat{\sigma}_- e^{i\omega_d t}\right), \end{aligned} \tag{3.24}$$

which also contains a term that is directly driving the qubit. Therefore, the small components of the cavity in the qubit eigenstates allows the qubit to be driven through the cavity input line by choosing $\omega_d \approx \omega_a$.

3.2 Coupling of motion to the island charge

The electrostatic energy depends parabolically on the gate charge and is shifted on the gate charge axis by the number of Cooper pairs on the island, see Eq. (3.2). Suppose now that the voltage gate is allowed to move or vibrate freely. The motion of the voltage gate modulates the capacitance of the island to gate. Assuming that the motion is small enough, we can restrict ourselves to consider only linear changes of the total capacitance, $\partial C/\partial x$. The change of electrostatic energy due to the gate motion x is

$$\Delta E_{\text{ch}} = -g(n - n_g)x, \tag{3.25}$$

where the coupling factor $g = 2eV_g\partial_x C_g/C$. Obviously, for each number of Cooper pairs on the island, there is only a single gate charge point where the motion of the gate does not couple to the electrostatic energy of the island, namely $n_g = n$. Looking at the electrostatic energy (see Eq. (3.2) and Fig. 3.2), this naturally corresponds to the points where the derivative $\partial E_{\text{ch}}/\partial n_g$ vanishes.

Theoretically, having one fixed gate to control the static gate charge and one freely vibrating gate to couple mechanical motion does not offer any advantage. Experimentally, however, this can be advantageous from the point of view of filtering. As seen from the equation for the coupling, the mechanically vibrating gate requires high dc voltage but needs to be filtered heavily to prevent any extra decoherence from affecting the qubit. On the other hand, it will turn out that the qubit might need to be driven through a voltage gate with GHz-regime signals, thus requiring a completely different kind of filtering.

3.2.1 Charge qubit

So far we have only considered an isolated island to explicitly show that the coupling between the island and the gate motion exists almost everywhere except at very special points. Let us now consider the coupling of mechanical motion to charge qubit eigenstates. The energy diagram suggests that small modulations of the gate charge do not affect the qubit transition frequencies at gate charge points $n_g = 0$ and $n_g = 0.5$, for example. Outside the degeneracy points, the lowest Cooper pair states are almost exactly the Cooper pair number states. Therefore, it is not surprising that the coupling vanishes at $n_g = 0$ as we have noted already earlier. However, the Cooper pair states are coupled to motion at $n_g = 0.5$ whereas the coupling to the Cooper pair box seemingly vanishes at that point due to the anticrossing that the Josephson coupling has induced.

To examine the coupling around the degeneracy points more closely, let us consider the transformation of the Cooper pair basis that diagonalizes the charge qubit Hamiltonian in Eq. (3.6). The transformation is a rotation $R(\theta)$ with the rotation angle given by [51]

$$\theta = \frac{1}{2} \arctan\left(-\frac{E_J}{4E_C(1-2n_g)}\right). \tag{3.26}$$

To get the coupling in the qubit eigenbasis, this transformation has to be applied for the coupling term between the mechanics and the Cooper pair box. In the case of a superconducting island, the coupling is given by $H_{\text{int}} = -2eV_g \frac{\partial_x C_g}{C}(\hat{n} - n_g)\hat{x}$. Assuming that the gate vibrates harmonically around some point with frequency ω_m, we can write the position operator with annihilation and creation operators ($\hat{b}$ and $\hat{b}^\dagger$) as $\hat{x} = x_{\text{zp}}(\hat{b}^\dagger + \hat{b})$. The zero-point motion of the mechanics is given by $x_{\text{zp}} = \sqrt{\hbar/2m\omega_m}$. The coupling then reads

$$\hat{H}_{\text{int}} = -\hbar g(\hat{n} - n_g)(\hat{b}^\dagger + \hat{b}), \tag{3.27}$$

where

$$g = x_{\text{zp}} V_g \frac{\partial_x C_g}{C} 2e/\hbar. \tag{3.28}$$

The total Hamiltonian to transform in the Cooper pair basis is

$$\hat{H} = -2E_C(1-2n_g)\hat{\sigma}_z - \frac{E_J}{2}\hat{\sigma}_x + \frac{\hbar g}{2}(1 - 2n_g + \hat{\sigma}_z)(\hat{b}^\dagger + \hat{b}). \tag{3.29}$$

Using the transformation of basis with the angle given in Eq. (3.26) diagonalizes the first two terms and the coupling term becomes

$$\tilde{H}_{\text{int}} = R(\theta) H_{\text{int}} R^\dagger(\theta) = \frac{\hbar g}{2}(1 - 2n_g + \cos 2\theta \hat{\sigma}_z + \sin 2\theta \hat{\sigma}_x)(\hat{b}^\dagger + \hat{b}). \tag{3.30}$$

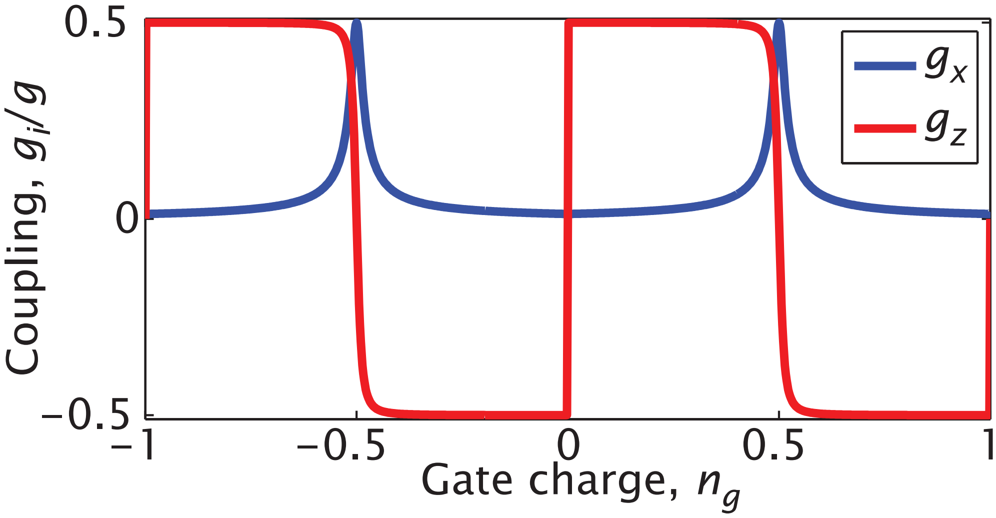

Fig. 3.4: Coupling direction of mechanics to a charge qubit. $E_J = E_C/10$.

Away from the degeneracy point $n_g = 0.5$ and given that $E_J \ll E_C$, the mixing angle is small $\theta \ll 1$ implying $\arctan z \approx z$ and $\cos 2\theta = 1$ as well as $\sin 2\theta = 0$. The coupling has only $\hat{\sigma}_z$ component with strength $\hbar g/2$ and is therefore longitudinal.

At the degeneracy point, the mixing angle becomes equal to $\pi/4$ implying $\cos 2\theta = 0$ and $\sin 2\theta = 1$. The longitudinal coupling thus vanishes exactly at the degeneracy point but the $\hat{\sigma}_x$ component emerges with the strength $\hbar g/2$, equal in magnitude to the longitudinal coupling out of the degeneracy.

To exemplify this limiting case, the amplitude of coupling is schematically represented as a function of the gate charge in Fig. 3.4. The eigenbasis is chosen continuously such that g_x is positive. The E_J/E_C ratio is 0.1 to widen the effects around the degeneracy points and the diagonalization is done numerically with more than two Cooper pair states. As expected, the coupling is mostly longitudinal with the absolute magnitude reaching $g/2$. As can be deduced from the energy diagram in Fig. 3.2, the $\hat{\sigma}_z$ coupling changes sign at every half-integer and integer values of gate charge. The sign is positive with $n_g \in (0, 0.5)$ due to the increasing transition frequency with increasing gate charge and vice versa for $n_g \in (0.5, 1)$.

Close to the degeneracy points, the coupling rotates to $\hat{\sigma}_x$ coupling but does not vanish. At integer values, the $\hat{\sigma}_z$ coupling goes to zero due to anticrossing of the higher Cooper pair states. The lower part of this anticrossing between Cooper pair states $|-1\rangle$ and $|1\rangle$ is just visible in Fig. 3.2 at $n_g = 0$.

We have thus carefully shown that the flatness of spectrum does not indicate that no coupling exists. In the case of a charge qubit, one could mistakenly take the degeneracy point to be uncoupled from gate charge modulations. We have shown that this is the case for longitudinal coupling but the underlying coupling to Cooper pair states is transformed to transversal coupling [65]. A very similar situation will be encountered in the so-called transmon regime where the dispersion curves of qubit transition become completely flat with respect to the gate charge. We will show that the coupling to mechanical motion is just transformed to $\hat{\sigma}_x$ direction as was the case here.

3.2.2 Transmon

To conclude this section, we consider the direction of transmon coupling to mechanics. Writing the coupling term of Eq. (3.27) in uncoupled qubit eigenbasis gives

$$H_{\text{int}} = -\hbar \sum_{i,j} g_{ij} |i\rangle\langle j| (\hat{b}^\dagger + \hat{b}), \tag{3.31}$$

where $|i\rangle$ is the ith eigenstate of the system and

$$g_{ij} = g\langle i|\hat{n} - n_g|j\rangle. \tag{3.32}$$

With a high E_J/E_C ratio, the gate charge n_g does not affect g_{ij}. In this limit, similarly to how the approximate eigenenergies were derived, the matrix element can be approximated [49] by fourth order expansion of the phase. Asymptotically the Cooper pair number operator can be expressed as proportional to the momentum operator of the harmonic oscillator that approximates the transmon. In this limit,

$$|\langle j+1|\hat{n}|j\rangle| \approx \sqrt{\frac{j+1}{2}} \left(\frac{E_J}{8E_C}\right)^{1/4}, \tag{3.33}$$

while $|\langle j+k|\hat{n}|j\rangle| \to 0$ and $|\langle j|\hat{n}|j\rangle| \to 0$ as $E_J/E_C \to \infty$ for $k > 0$.

By restricting to the two lowest states, the coupling can be written using Pauli matrices as

$$H_{\text{int}} = -\hbar \left(g_x\hat{\sigma}_x + g_y\hat{\sigma}_y + g_z\hat{\sigma}_z\right)(\hat{b}^\dagger + \hat{b}), \tag{3.34}$$

where

$$g_x = g\text{Re}\langle 0|\hat{n} - n_g|1\rangle, \tag{3.35}$$

$$g_y = g\text{Im}\langle 0|\hat{n} - n_g|1\rangle, \tag{3.36}$$

$$g_z = g\left(\langle 1|\hat{n} - n_g|1\rangle - \langle 0|\hat{n} - n_g|0\rangle\right)/2. \tag{3.37}$$

The numerical diagonalizations of the coupling to the qubit eigenbasis is shown in Fig. 3.5. The $\hat{\sigma}_y$ component is not shown since it vanishes everywhere.

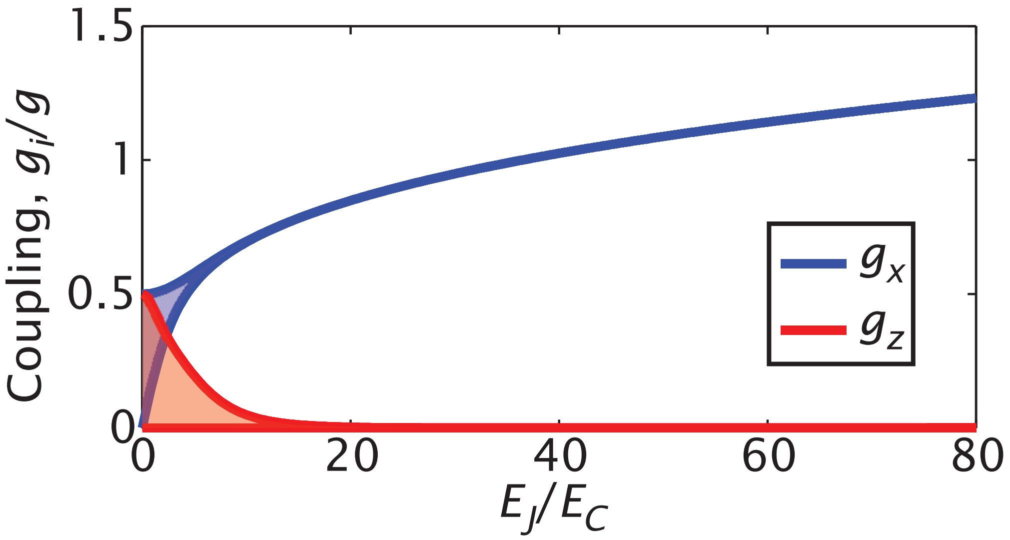

Fig. 3.5: Absolute values of mechanics coupling to $\hat{\sigma}_x$ and $\hat{\sigma}_z$ in the qubit eigenbasis for the Cooper pair box with different E_J/E_C ratio. The shaded regions denote the coupling at different gate charge points with the lines implying the minimum and maximum coupling. Obviously, the dependency on gate charge vanishes with increasing E_J/E_C ratio as does the longitudinal coupling.

3.3 Motional qubit sidebands

So far we have concluded that mechanical motion is coupled to charge-based qubits since it modulates the capacitance and therefore the gate charge, resulting in Eq. (3.34). In practice however, the two system are almost perfectly detuned, $\omega_m \sim \omega_a/100$. Therefore even ultrastrong coupling ($g \sim \omega_m$) does not on its own results in dramatic changes in the evolution of the two systems. To probe the coupling and to intertwine the evolutions, one can introduce an additional drive tone to qubit which brings the states of the combined system on resonance and allows swapping quanta between the two. The scheme is much the same as in experiments where the transition of a trapped ion is coupled to the harmonic motion of the ion in the trapping potential [66].

3.3.1 Floquet representation

Let us first consider the case where qubit excitation drive at ω_s is applied to a charge qubit operated away from the gate charge sweet spot, $n_g \neq 0.5$. In this case, driving the Josephson energy term drives $\hat{\sigma}_x$ of the qubit, see Eq. (3.6). The total Hamiltonian in the qubit eigenbasis is given by

$$\begin{aligned}\hat{H} =& \hat{H}_0 + \hat{H}_1(t) \\ =& \underbrace{\frac{\hbar\omega_a}{2}\hat{\sigma}_z + \hbar\omega_m \hat{b}^\dagger \hat{b} - \hbar g_z \hat{\sigma}_z (\hat{b}^\dagger + \hat{b})}_{\hat{H}_0} + \underbrace{\hbar\Omega_x \cos(\omega_s t)\hat{\sigma}_x}_{\hat{H}_1(t)},\end{aligned} \tag{3.38}$$

where Ω_x denotes the strength of the drive and all other couplings except $\hat{\sigma}_z$ have vanished.

To derive an analytical formula for the Rabi frequency that describes the oscillation frequency between the two parts of the systems, we move to a frame where the time-dependency of the Hamiltonian vanishes. One way to accomplish this is to use Floquet representation [67]. Mathematically this corresponds to Fourier expanding the time-dependent field and constructing field-dressed states of the qubit. This eliminates the fast time scale of the excitation drive (ω_s) and leaves only the slow time scale modulation of the envelope function ($\Omega_x(t)$), which we assume to evolve adiabatically so that the system eigenstates follow the Floquet states [68]. The Floquet picture formalism is reviewed in appendix D.

To derive the Floquet Hamiltonian $\hat{H}_F$, we just need the Fourier components of $\cos(\omega_s t) = (\exp(i\omega_s t) + \exp(-i\omega_s t))/2$. Thus, $\langle \alpha n|\hat{H}_F|\beta n\rangle = \langle\alpha|\hat{H}_0|\beta\rangle + n\hbar\omega_s$, where α and β denote undriven qubit eigenstates and n is the Floquet index. Furthermore, $\langle \alpha n|\hat{H}_F|\beta m\rangle = \hbar\Omega_x/2\langle\alpha|\hat{\sigma}_x|\beta\rangle$ for $m = n \pm 1$ and zero otherwise. To derive analytical formulas in the limit of weak driving, we can restrict the Floquet Hamiltonian to two Floquet blocks, $m = 0$ and $m = -1$, which correspond to zero or one quantum taken from the driving field. In this case, the Floquet Hamiltonian reads

$$\hat{H}_F = \begin{pmatrix} \hat{H}_0 & \hbar\Omega_x/2\left(\hat{\sigma}_x \otimes \hat{I}\right) \\ \hbar\Omega_x/2\left(\hat{\sigma}_x \otimes \hat{I}\right) & \hat{H}_0 - \hbar\omega_s \end{pmatrix}. \tag{3.39}$$

Here we have denoted the composite state of the qubit, mechanics, and Floquet state as $|q\rangle \otimes |n\rangle \otimes |m\rangle = |q, n, m\rangle$.

In the case of perfectly red-detuned drive and in the absence of loss we can restrict further to only two mechanical Fock states, n and $n - 1$. We can employ perturbation theory to take into account the effect of all non-diagonal terms in the Floquet Hamiltonian. Specifically, we use perturbation theory to derive an effective Hamiltonian which acts only within a manifold of energy levels which are well separated in energy from the other states, see complement CI in [69].

In our case, the manifold we study in the Floquet picture is composed of states $|0, n, m\rangle$ and $|1, n-1, m-1\rangle$. Our treatment thus requires that

$$|\langle i, \alpha|\lambda\hat{V}|m, \gamma\rangle| \ll |E_{i,\alpha} - E_{m,\gamma}|, \quad \alpha \neq \gamma \tag{3.40}$$

where $|m, \gamma\rangle$ denotes the mth eigenstate of manifold γ and the perturbation is written as $\lambda\hat{V}$ with λ being a dimensionless parameter. In the charge-qubit regime, this requirement converts to

$$|g_z|\sqrt{n}, \Omega_x/2 \ll \omega_m. \tag{3.41}$$

The matrix elements of the effective Floquet Hamiltonian $\hat{H}_F^{\text{eff}}$ are given by

$$\begin{aligned} \langle i|\hat{H}_F^{\text{eff}}|f\rangle &= E_i\delta_{if} + \langle i, \alpha|\lambda\hat{V}|f, \alpha\rangle \\ &+ \frac{1}{2}\sum_{m,\gamma\neq\alpha} \langle i, \alpha|\lambda\hat{V}|m, \gamma\rangle\langle m, \alpha|\lambda\hat{V}|f, \gamma\rangle \left(\frac{1}{E_{i\alpha} - E_{m\gamma}} + \frac{1}{E_{f\alpha} - E_{m\gamma}}\right), \end{aligned} \tag{3.42}$$

where the manifold under study is denoted with α.

In the case of perfectly red detuned drive, the two states are perfectly degenerate so that $E_i = E_f$ in the equation describing their effective coupling and the transition amplitude between them is given by

$$A = \sum_{m,\gamma\neq\alpha} \frac{\langle i, \alpha|\lambda V|m, \gamma\rangle\langle m, \alpha|\lambda V|f, \gamma\rangle}{E_i - E_m}, \tag{3.43}$$

where $|m\rangle$ is the intermediate state through which the system virtually transits. Note that the second term on the left in Eq. (3.42) vanishes since there is no direct coupling between the states. In the case of second order coupling between states $|0, n, m\rangle$ and $|1, n-1, m-1\rangle$, the transition can happen via states $|0, n-1, m\rangle$ and $|1, n, m-1\rangle$, see Fig. 3.6(a). Thus, the total amplitude is

$$A = \hbar\Omega_x \frac{g_z\sqrt{n}}{\omega_m}. \tag{3.44}$$

Writing out once more the effective coupling due to the second order coupling

$$\hat{H}_{\text{int}} = \hbar\Omega_x \frac{g_z}{\omega_m}(\hat{b}^\dagger\hat{\sigma}_- + \hat{b}\hat{\sigma}_+). \tag{3.45}$$

We therefore see that the system obeys Jaynes-Cummings Hamiltonian where the two systems appear resonant while the coupling g_z is degraded by factor Ω_x/ω_m. The systems are thus capable of swapping quantum back and forth if

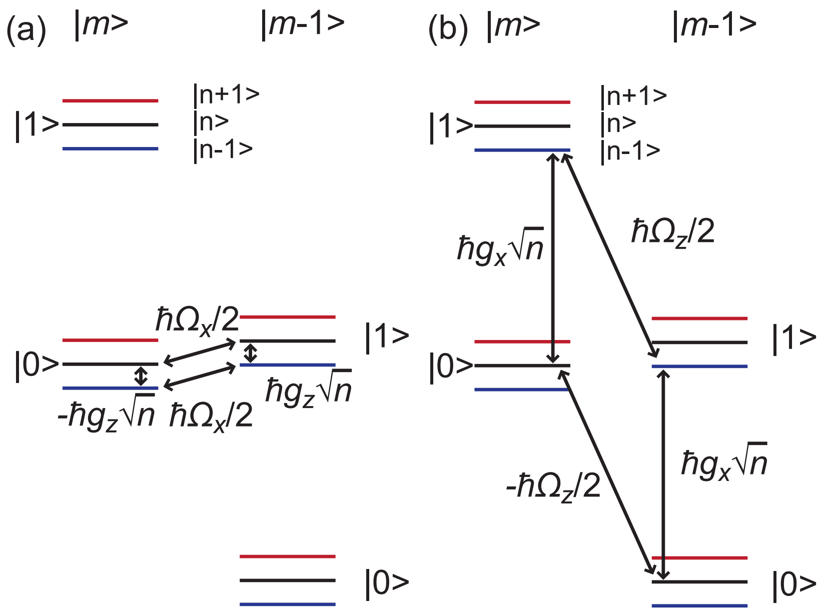

Fig. 3.6: Schematics of the red-sideband transitions of the qubit-mechanics system. (a) Charge-qubit regime and (b) transmon regime. In the uncoupled qubit eigenbasis, both are second-order transitions. However, the intermediate state in the transmon regime is an order of magnitude further than in the charge-qubit regime. This results in larger denominator in the expression for the effective coupling between states $|0, n\rangle$ and $|1, n-1\rangle$ (see Eq. (3.43)) therefore resulting in smaller coupling as compared to the longitudinal coupling case.

allowed by the coherence. The Rabi frequency can be increased with stronger drive. Even the drive is detuned from the qubit by ω_m, the $\hat{\sigma}_x$ drive will start to directly excite the qubit through the first-order term with higher drive powers. This is a drawback as compared to the following transmon regime in which the $\hat{\sigma}_z$ drive of the qubit can not excite the qubit.

In the transmon regime and in the absence of driving, the mechanics couples transversely to the qubit,

$$\hat{H}_0 = \frac{\hbar\omega_a}{2}\hat{\sigma}_z + \hbar\omega_m\hat{b}^\dagger\hat{b} - \hbar g_x\hat{\sigma}_x(\hat{b}^\dagger + \hat{b}). \tag{3.46}$$

This coupling is depicted in the Floquet representation with the vertical lines in Fig. 3.6(b). To complete the second order transition route between states $|0, n, m\rangle$ and $|1, n-1, m-1\rangle$, the qubit drive $\hat{H}_1(t)$ has to preserve the state and thus couple to $\hat{\sigma}_z$. Driving in $\hat{\sigma}_z$ direction produces an extra minus sign to the path via $|0, n, m-1\rangle$, thus resulting in constructive interference between the two paths. The total amplitude given by Eq. (3.43) is

$$A = \hbar\Omega_z \frac{g_x\sqrt{n}}{\omega_a - \omega_m}. \tag{3.47}$$

Comparing Eqs. (3.44) and (3.47), we note that with g_z coupling, the effective coupling is not affected by large detuning between the qubit and mechanics. The coupling constant g_z itself is degraded if the E_J/E_C ratio is increased (see Fig. 3.5) because the coupling becomes transversal. However, if the qubit frequency is increased by reducing the total capacitance C (that is, increasing E_C), the effective coupling only grows (see Eq. (3.28)). Unfortunately, this is naturally the regime where also the undesired coupling to electrical defects increases and therefore is not the best option for present superconducting systems.

In the transmon regime, the effective coupling Eq. (3.47) has the detuning between the two systems in the denominator. Increasing E_J will increase qubit frequency proportional to $E_J^{1/2}$ (Eq. (3.11)) while the coupling increases only proportional to $E_J^{1/4}$ (Eq. (3.33)). In total, the effective coupling will be decreased only slowly with E_J while the sensitivity to charge fluctuations is decreased exponentially [49].

In this section, we derived analytical formulas for the red-sideband transitions using Floquet formalism to suppress the time-dependencies of the drive. This served as an example for the use of Floquet representation but it also provided a very intuitive picture of the sideband transition. We could have similarly derived also the blue-sideband transition amplitudes in which the n would be replaced by $n+1$ in Eqs. (3.44) and (3.47). In the next section, we will derive sideband transitions using a less intuitive but more general derivation based on transformation of the basis.

3.3.2 Rotating frame

Consider now the qubit-mechanics Hamiltonian in the transmon regime with the qubit driven longitudinally,

$$\hat{H}(t) = \frac{\hbar\omega_a}{2}\hat{\sigma}_z + \hbar\omega_m\hat{b}^\dagger\hat{b} + \hbar g_x\hat{\sigma}_x(\hat{b}^\dagger + \hat{b}) + \hbar\Omega_z\cos(\omega_s t)\hat{\sigma}_z. \tag{3.48}$$

To obtain analytical results, the time-dependency needs to be dealt with. We can remove it by moving to a non-uniformly rotating basis [70] by transforming the qubit eigenbasis $|\Psi'(t)\rangle = \hat{U}(t)|\Psi\rangle$,

$$\hat{U}(t) = e^{i\frac{\Omega_z}{\omega_s}\sin(\omega_s t)\hat{\sigma}_z}. \tag{3.49}$$

The Hamiltonian in the new eigenbasis is given by

$$\hat{H}'(t) = \hat{U}(t)\hat{H}(t)\hat{U}^{\dagger}(t) + i\hbar\frac{\partial\hat{U}(t)}{\partial t}\hat{U}^{\dagger}(t). \tag{3.50}$$

The rotation was chosen such that the last term

$$i\hbar\frac{\partial\hat{U}(t)}{\partial t}\hat{U}^{\dagger}(t) = -\hbar\Omega_z\cos(\omega_s t)\hat{\sigma}_z, \tag{3.51}$$

exactly cancels the time-dependency of the original Hamiltonian. Furthermore, since $\hat{\sigma}_z$ commutes with the transformation, the time-dependency of the qubit is transferred to the mechanical coupling. Using the Baker-Hausdorff relation in evaluation, $\hat{\sigma}_x$ is transformed to

$$\hat{U}(t)\hat{\sigma}_x\hat{U}^{\dagger}(t) = e^{i\alpha}\hat{\sigma}'_{+} + e^{-i\alpha}\hat{\sigma}'_{-}, \tag{3.52}$$

where $\alpha = \frac{2\Omega_z}{\omega_s}\sin(\omega_s t)$ and $\hat{\sigma}'_{+}$ ($\hat{\sigma}'_{-}$) is the raising (lowering) operator for the qubit in the new eigenbasis. Dropping the apostrophes, the Hamiltonian in the non-uniformly rotating frame reads

$$\begin{aligned}\hat{H}(t) &= \frac{\hbar}{2}\omega_a\hat{\sigma}_z + \hbar g_x(\hat{b}^{\dagger} + \hat{b})(e^{i\alpha}\hat{\sigma}_{+} + e^{-i\alpha}\hat{\sigma}_{-}) + \hbar\omega_b\hat{b}^{\dagger}\hat{b} \qquad (3.53)\\ &= \frac{\hbar}{2}\omega_a\hat{\sigma}_z + \hbar g_x(e^{-i\alpha}\hat{b}^{\dagger}\hat{\sigma}_{-} + e^{i\alpha}\hat{b}\hat{\sigma}_{+}) + \hbar g_x(e^{i\alpha}\hat{b}^{\dagger}\hat{\sigma}_{+} + e^{-i\alpha}\hat{b}\hat{\sigma}_{-}) + \hbar\omega_b\hat{b}^{\dagger}\hat{b},\end{aligned}$$

where in the second line I have regrouped the terms such that the first coupling term resembles the Jaynes-Cummings coupling and the second coupling term resembles the anti-Jaynes-Cummings coupling (apart from the phase factors $e^{\pm i\alpha}$). Looking at Eq. (3.53), it seems that time-dependencies can be removed by transforming the mechanics basis accordingly. However, since α has a very complicated time-dependency, we will eventually have to resort to rotating-wave approximation. To get a clearer picture of time-dependencies, we can expand using Jacobi-Anger relations

$$\begin{aligned}\hat{U}(t)\hat{\sigma}_x\hat{U}^{\dagger}(t) = &\left\{J_0\left(\frac{2\Omega_z}{\omega_s}\right) + \sum_{n=1}^{\infty} J_n\left(\frac{2\Omega_z}{\omega_s}\right)\left[e^{in\omega_s t} + (-1)^n e^{-in\omega_s t}\right]\right\}\hat{\sigma}_{+}\\ &+\left\{J_0\left(\frac{2\Omega_z}{\omega_s}\right) + \sum_{n=1}^{\infty} J_n\left(\frac{2\Omega_z}{\omega_s}\right)\left[e^{-in\omega_s t} + (-1)^n e^{in\omega_s t}\right]\right\}\hat{\sigma}_{-}.\end{aligned} \tag{3.54}$$

The form of time-dependency in Eq. (3.54) suggests the need to also transform the mechanics eigenbasis with $\hat{U}_m(t) = e^{-i\omega_s t\hat{b}^{\dagger}\hat{b}}$ such that the transformation commutes with $\hat{b}^\dagger\hat{b}$ and gives

$$i\hbar\frac{\partial\hat{U}_m(t)}{\partial t}\hat{U}_m^\dagger(t) = +\,\hbar\omega_s\hat{b}^\dagger\hat{b}, \tag{3.55}$$

$$\hat{U}_m(t)\hat{b}^\dagger\hat{U}_m^\dagger(t) = \hat{b}^\dagger e^{-i\omega_s t}, \tag{3.56}$$

$$\hat{U}_m(t)\hat{b}\hat{U}_m^\dagger(t) = \hat{b}e^{i\omega_s t}. \tag{3.57}$$

Thus, the doubly transformed Hamiltonian reads

$$\begin{aligned}\hat{H}(t) = \frac{\hbar}{2}\omega_a\hat{\sigma}_z &+ \hbar g_x(e^{-i(\alpha+\omega_s t)}\hat{b}^\dagger\hat{\sigma}_- + e^{i(\alpha+\omega_s t)}\hat{b}\hat{\sigma}_+) \\ &+ \hbar g_x(e^{i(\alpha-\omega_s t)}\hat{b}^\dagger\hat{\sigma}_+ + e^{-i(\alpha-\omega_s t)}\hat{b}\hat{\sigma}_-) + \hbar(\omega_m+\omega_s)\hat{b}^\dagger\hat{b}.\end{aligned} \tag{3.58}$$

Consider now a qubit driven close to the red sideband such that the anti-Jaynes-Cummings terms can be neglected. Making rotating wave approximation and neglecting terms which oscillate with at least $e^{\pm i\omega_s t}$,

$$\hat{H}(t) = \frac{\hbar}{2}\omega_a\hat{\sigma}_z - \hbar g_x J_1\left(\frac{2\Omega_z}{\omega_s}\right)(\hat{b}^\dagger\hat{\sigma}_- + \hat{b}\hat{\sigma}_+) + \hbar(\omega_m+\omega_s)\hat{b}^\dagger\hat{b}, \tag{3.59}$$

which is again the standard Jaynes-Cummings Hamiltonian for which all kinds of analytical results exist. By choosing the optimal detuning for the qubit drive $\omega_s = \omega_a - \omega_m$,

$$\hat{H}(t) = \frac{\hbar}{2}\omega_a\hat{\sigma}_z - \hbar g_x J_1\left(\frac{2\Omega_z}{\omega_a-\omega_b}\right)(\hat{b}^\dagger\hat{\sigma}_- + \hat{b}\hat{\sigma}_+) + \hbar\omega_a\hat{b}^\dagger\hat{b}. \tag{3.60}$$

In the limit of weak driving, $2\Omega_z \ll \omega_a - \omega_b$, the transition amplitude between states $|g,n\rangle$ and $|e,n-1\rangle$ is given approximately by

$$A = \hbar g_x J_1\left(\frac{2\Omega_z}{\omega_a-\omega_b}\right)\sqrt{n} \approx \hbar g_x\frac{\Omega_z\sqrt{n}}{\omega_a-\omega_b}, \tag{3.61}$$

which agrees with the Floquet picture derivation in Eq. (3.47).

Equation (3.61) confirms what is clear intuitively that by increasing the qubit drive, one can not surpass the limits of information transfer dictated by the rate of coupling g_x between the systems. Actually, it is limited roughly to $\approx 0.58g_x$ given by the first maximum of J_1. In practice, the qubit drive is limited to the regime where the qubit transition frequency is linearly modulated as a function of external parameter, which in the transmon regime is the magnetic flux through the superconducting quantum interference device (SQUID) loop. With larger modulations, motional averaging of the qubit transition frequency [71] starts to take place, severely complicating the sideband measurement.

3.4 Strong gate drive

In the following, we will consider a qubit driven with a strong sinusoidal classical field applied to the gate. The drive can be either high amplitude motion of the mechanics that affects the capacitance or gate charge oscillations induced purely by voltage drive. In both cases, the frequency of the modulation is taken to be far below the transition frequency of the qubit so that it does not cause transitions. And on the other hand, the modulation is assumed to be faster than the relaxation time scale of the qubit so that the qubit eigenstates are transformed into field-dressed states by the driving field. A proper way to take into account the different time scales would be to model the system with a master equation including decoherence terms for the qubit. We however simply use the Schrödinger equation which is justified if the modulation frequency is a lot faster than the qubit decoherence rates [71].

First, we will consider mechanical motion excited to high amplitude with a voltage drive applied to the mechanical gate. Here, the high amplitude motion refers to gate charge modulations large enough to probe the nonlinearity of the transition frequency on the gate charge. We will develop the qubit quasienergy states using Floquet formalism in which the time-dependency of a finite-dimensional system is transformed into a time-independent problem of infinite system, see App. D.

The Hamiltonian we consider is given by (see Fig. 3.1 for circuit diagram)

$$\begin{aligned}\hat{H}(t) = 4E_C(\hat{n}-n_g(t))^2 - E_{J+}(\Phi_{\mathrm{dc}})/2\sum_n \left(|n\rangle\langle n+1| + |n+1\rangle\langle n|\right) \quad (3.62)\\ -E_{J-}(\Phi_{\mathrm{dc}})/2\sum_n i\left(|n\rangle\langle n+1| - |n+1\rangle\langle n|\right),\end{aligned}$$

where the gate charge is sinusoidally modulated, $n_g(t) = n_g + \Delta n_g \cos(\omega_m t)$ and the symmetric and antisymmetric parts of the Josephson coupling are given by

$$E_{J+}(\Phi_{\mathrm{dc}}) = (E_{J1}+E_{J2})\cos\left(\pi\frac{\Phi_{\mathrm{dc}}}{\Phi_0}\right), \quad (3.63)$$

$$E_{J-}(\Phi_{\mathrm{dc}}) = (E_{J1}-E_{J2})\sin\left(\pi\frac{\Phi_{\mathrm{dc}}}{\Phi_0}\right), \quad (3.64)$$

where E_{J1} and E_{J2} are the Josephson energies of the individual junctions, Φ_{dc} is the constant flux through the SQUID loop, and Φ_0 is the flux quantum. The Hamiltonian can be split into two parts such that

$$\hat{H}(t) = \hat{H}_0 + \delta\hat{H}(t) = \hat{H}_0 + 8E_C(\hat{n}-n_g(t))\Delta n_g\cos(\omega_m t), \quad (3.65)$$

where $\hat{H}_0$ denotes the static part of the Hamiltonian (obtained from Eq. (3.62) with $n_g(t) = n_g$). The corresponding Floquet Hamiltonian can be represented as a tridiagonal block matrix

$$\hat{H}_F = \begin{pmatrix} \ddots & \ddots & & & \\ \ddots & \hat{H}_0 + \omega_s & \hat{H}^{[+1]} & & \\ & \hat{H}^{[-1]} & \hat{H}_0 & \hat{H}^{[+1]} & \\ & & \hat{H}^{[-1]} & \hat{H}_0 - \omega_s & \ddots \\ & & & \ddots & \ddots \end{pmatrix}, \qquad (3.66)$$

where only the first off-diagonal Floquet terms of Fourier series remain corresponding to the fundamental frequency $\pm\omega_m$, $\hat{H}^{[\pm 1]} = 4E_C(\hat{n} - n_g(t))\Delta n_g$.

To obtain a computable problem, the representation dimension of the operator blocks in Cooper pair number states have to be chosen such that the qubit eigenstates are modeled accurately enough. This requires taking into account a sufficient amount of Cooper pair number states determined by the E_J/E_C ratio and in this case also by the amplitude of the gate charge modulation Δn_g. The number of Floquet blocks is determined by Δn_g and the desired number of levels of the qubit to be modeled. Higher levels have stronger dependency on the gate charge so that they get more strongly dressed by the driving field and they therefore require more Floquet blocks to be included.

3.4.1 Quasienergies and dynamic Stark shift

Using the parameters from the experiment presented in Publication **IV**, transition energy is presented in Fig. 3.7 as a function of gate charge modulation amplitude. Here, the number of Floquet blocks used in the modeling is 2001 and the number of Cooper pair states is 21. The gate charge modulation is induced by a voltage drive resonant with the mechanics. The modulation thus has both a mechanical and an electrical component which affects the response if the drive frequency is not perfectly matched with the mechanical resonance. This situation will be discussed in the next section.

Quasienergies oscillate with Bessel-like dependency on the gate charge amplitude. Transition energies appear to periodically converge towards a single point at amplitudes independent of the gate charge. This can be analytically modeled by assuming sinusoidal charge dispersion (see the supplementary material of Publication **IV**). According to the analytical model, transition energies cross each other at exactly the same gate charge amplitude which makes the transition completely independent of gate charge. Deviations from the perfect sinusoidal gate charge dependency and eigenstates composed of many Cooper pair

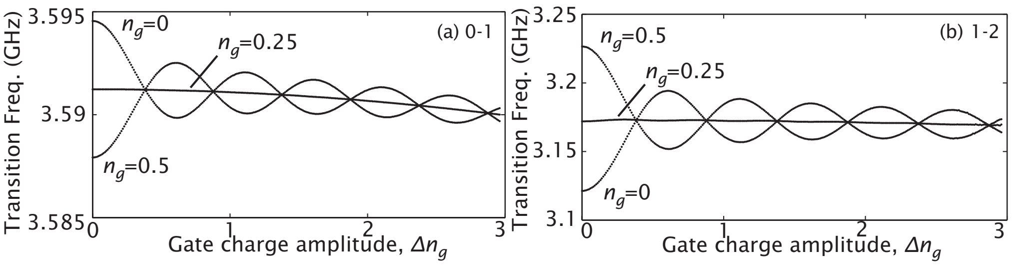

Fig. 3.7: Quasienergy transition as a function of gate charge amplitude. (a) Lowest transition 0-1 and (b) transition 1-2. The normalized flux is set to 0.32.

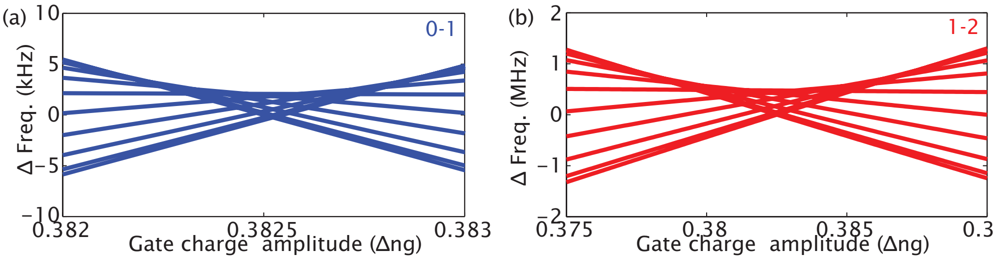

Fig. 3.8: Zoomed-in plot of the quasienergies around the first crossing point shown in Fig. 3.7.

states however break this perfect crossing point and introduce minute differences. Magnification of the first crossing point is shown in Fig. 3.8 displaying the minimum of charge dependencies of the two lowest transitions.

For the 0-1 transition, the minimum charge dependency is 2.4 kHz and for the 1-2 transition, the minimum charge dependency is 475 kHz. In units of charging energy, these values correspond to 7.4 $10^{-6}E_C$ and 1.5 $10^{-3}E_C$. Using equation (3.7), these peak-to-peak amplitudes correspond to E_J/E_C ratios of 61 and 32 calculated for the lowest transition ($m = 1$). Therefore, even the higher transition 1-2 becomes reasonably well protected from low frequency charge noise and operable as a qubit as long as the relaxation out of the two levels can be suppressed sufficiently. These ratios represent a formidable increase in the effective E_J/E_C ratio; the original ratio being 20 at normalized flux 0.32. In analogy to charge qubit sweet spots, I term these crossing points dynamical sweet spots.

3.4.2 Ac Stark shift

Figure 3.7 shows transition frequencies bending downwards as the gate charge modulation amplitude is increased. The effect is more visible in Fig. 3.7(a) al-though the absolute effect is larger in Fig. 3.7(b). Analyzing this shift by looking at the 0-1 transition as a function of gate charge amplitude at $n_g = 0.25$ where the dynamic Stark shift is minimized, one finds that the shift is parabolic in gate charge amplitude according to the Floquet analysis and thus linear in mechanics occupation, $\Delta n_g \propto x \propto \sqrt{\hat{b}^\dagger \hat{b}}$.

We derived in Eq. (3.23) that

$$\hat{H} = \hbar\omega_a \frac{\hat{\sigma}_z}{2} + \hbar\omega_m \hat{b}^\dagger \hat{b} + \hbar g_x (\hat{b}^\dagger \hat{\sigma}_- + \hat{b}\hat{\sigma}_+), \tag{3.67}$$

can be diagonalized as

$$\hat{H}_{\text{eff}} = \hbar\omega_a \frac{\hat{\sigma}_z}{2} + \hbar\omega_m \hat{b}^\dagger \hat{b} + \hbar\chi_m \left(\hat{b}^\dagger \hat{b} + \frac{1}{2}\right)\hat{\sigma}_z, \tag{3.68}$$

where $\chi_m = g_x^2/(\omega_a - \omega_m)$. Similarly, in the case of longitudinal coupling, the Hamiltonian

$$\hat{H} = \hbar\omega_a \frac{\hat{\sigma}_z}{2} + \hbar\omega_m \hat{b}^\dagger \hat{b} + \hbar g_z \hat{\sigma}_z (\hat{b}^\dagger + \hat{b}) \tag{3.69}$$

can be diagonalized with a similar transformation,

$$\hat{S} = \frac{g_z}{\omega_m} \hat{\sigma}_z \left(\hat{b}^\dagger - \hat{b}\right). \tag{3.70}$$

It turns out that this transformation diagonalizes the Hamiltonian exactly since

$$\left[\hat{S}, \hat{H}\right] = -\hbar g_z \hat{\sigma}_z \left(\hat{b}^\dagger + \hat{b}\right) - 2\frac{\hbar g_z^2}{\omega_m}\hat{I} \tag{3.71}$$

$$\left[\hat{S}, \left[\hat{S}, \hat{H}\right]\right] = 2\frac{\hbar g_z^2}{\omega_m}\hat{I}, \tag{3.72}$$

and all the higher commutators are zero. The transformed Hamiltonian is

$$\hat{H}_{\text{eff}} = \hbar\omega_a \frac{\hat{\sigma}_z}{2} + \hbar\omega_m \hat{b}^\dagger \hat{b} - \frac{\hbar g_z^2}{\omega_m}\hat{I}. \tag{3.73}$$

Therefore, longitudinal coupling between the qubit and mechanics does not result in the eigenfrequency of one system depend on the occupation of the other. We have thus assured ourselves that longitudinal coupling can not produce Stark shifts. This is to be separated from the dynamical Stark shift of quasienergies described in section 3.4.1.

Thus one would expect to find the largest ac Stark shifts in regions where g_x is maximized, that is, in the transmon regime. The above derivations based on two level approximation are, however, misleading since in the transmon regime, one has to also consider the effect of higher qubit levels, see [49]. Roughly speaking, the second excited state pushes down the first excited state so that the ac Stark shift actually becomes negative at certain gate charge points in the transmon regime.

To obtain an intuitive interpretation of the decrease of transition frequencies as a function of gate drive amplitude, we can try to portray it as arising from an averaged ac Stark shift. That is, we assume that with high enough drive, the Stark shift of the dressed qubit state is given by averaging the Stark shifts of underlying undriven qubit states over the gate period. To estimate if this is plausible, the shift of transitions 0-1 and 1-2 due to adding one quantum to the mechanics is plotted in Fig. 3.9(a) as a function of the gate charge and at the same flux point as Fig. 3.7. Correspondingly, the transition frequencies 0-1 and 1-2 are plotted in Fig. 3.9(b) and the transversal couplings in the qubit eigenbasis are plotted in Fig. 3.9(c). The figures show that even though the transversal coupling hardly depends on the gate charge, the ac Stark shift depends due to the dependency of the second excited state on the gate charge point. As the energy gap between states 1-2 increases, the Stark shift push down due to level 2 on level 1 reduces and the Stark shift of transition 0-1 becomes positive around $n_g = 0.5$. A similar mechanism changes the sign of the transition 1-2 Stark shift due to the energy gap 2-3 which is not depicted in the figures.

To estimate the effect of ac Stark shift in the limit of high modulation, we take the average over the gate charge period to obtain $\chi_m^{\mathrm{ave}} = -0.88$ Hz for the 0-1 transition and $\chi_m^{\mathrm{ave}} = -2.57$ Hz for the 1-2 transition. To convert gate charge amplitudes to corresponding mechanical occupations and vice versa, we can employ sideband Rabi measurements that are carried out at the dynamical sweet spot. In the experiments presented in Publication **IV**, the sideband Rabi frequency is roughly three times slower than with the drive frequency exactly at the qubit transition frequency. Using Eq. (3.44) and the average Z coupling of 200 kHz, this gives a mechanical occupation of 14 400 at the dynamical sweet spot (equal to $\Delta n_g = 0.3825$). Using this conversion, the ac Stark shift is plotted in Fig. 3.10 as a function of gate charge amplitude.

To compare this half analytical, half numerical estimation, predictions of full Floquet treatment is plotted at gate charge $n_g = 0.25$ at which point the effects of motional averaging are minimized. Comparing the analytical estimation to the Floquet approach, it is clear that the interpretation of uniformly averaged Stark shift is not perfect but yet still gives a reasonable fit considering the very rough conversion done using the Rabi frequencies.

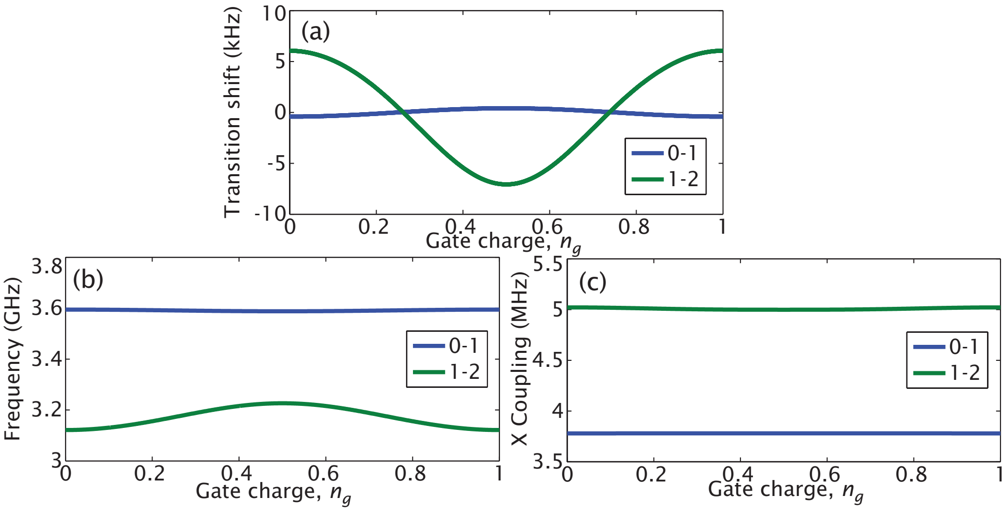

Fig. 3.9: Transition frequencies and transversal coupling in the undriven qubit eigenbasis at flux = 0.32. (a) Stark shift computed by diagonalizing the Hamiltonian at different gate charge points. (b) Transition frequencies of the two lowest transitions as a function of gate charge. (c) Transversal coupling to mechanics for the two lowest transitions. Obviously, the transversal coupling is almost independent of gate charge. Therefore, it is the dependence of eigenstates on gate charge that results in ac Stark shift changing with gate charge.

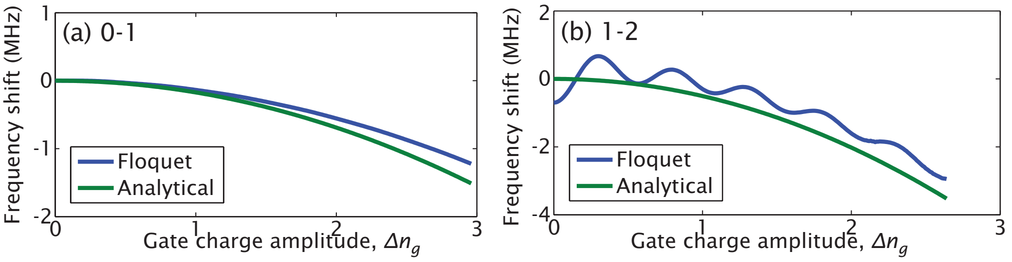

Fig. 3.10: ac Stark shift. Estimation for the linear ac Stark shift with high gate drive amplitudes for the (a) 0-1 and (b) 1-2 transitions based on averaged shift over the gate period. The conversion to units of gate charge amplitude is done using the sideband Rabi measurement. As a reference, a prediction from a full Floquet simulation is plotted with static gate charge $n_g = 0.25$.

3.4.3 Combined effect of the gate drive and mechanical motion

As the gate charge modulation is induced by mechanical motion that is excited by a voltage drive, the gate charge modulation is composed of two components (see the supplementary material of **IV**),

$$n_g(t) = n_g + \frac{C_g(t)V_g(t)}{2e} \approx n_g + \frac{\Delta C_g(t)V_g}{2e} + \frac{C_g\Delta V_g(t)}{2e}, \tag{3.74}$$

where $C_g(t) = C_g + \Delta C_g \cos(\omega_g t + \Theta)$ and $V_g(t) = V_g + \Delta V_g \cos(\omega_g t)$. ω_g is the angular frequency of the applied gate drive and Θ is the phase difference between the applied drive and the induced mechanical motion, $x(t) = A\cos(\omega_g t + \Theta)$,

$$\begin{aligned} A =& \frac{V_g \Delta V_g \partial C_g/\partial x}{m\sqrt{\omega_g^2\omega_m^2/Q_m^2 + (\omega_g^2 - \omega_m^2)^2}}, & (3.75)\\ \tan\Theta =& \frac{\omega_m\omega_g}{Q_m(\omega_m^2 - \omega_g^2)}, & (3.76)\end{aligned}$$

where Q_m is the mechanical resonator quality factor (see Eq. (2.13)) and ω_m is the mechanical resonant frequency. Defining gate charge amplitude due to the mechanical motion and due to the direct drive,

$$\begin{aligned} \Delta n_g^m =& A\frac{\partial C_g}{\partial x}\frac{V_g}{2e}, & (3.77)\\ \Delta n_g^d =& \frac{C_g \Delta V_g}{2e}, & (3.78)\end{aligned}$$

the gate charge can be written as

$$n_g(t) = n_g + \Delta n_g^m \cos(\omega_g t + \Theta) + \Delta n_g^d \cos(\omega_g t) = n_g + \Delta n_g \cos(\omega_g t + \theta), \tag{3.79}$$

where

$$\begin{aligned} \Delta n_g =& \sqrt{\Delta n_{g,m}^2 + \Delta n_{g,d}^2 + 2\Delta n_{g,m}\Delta n_{g,d}\cos\Theta}, & (3.80)\\ \tan\theta =& -\frac{\Delta n_{g,m}\sin\Theta}{\Delta n_{g,d} + \Delta n_{g,m}\cos\Theta}. & (3.81)\end{aligned}$$

An example of the total effective gate charge amplitude in the presence of both mechanical motion and the voltage drive inducing the motion is shown in Fig. 3.11. The red line denotes the gate charge amplitude if only mechanical motion is present, while the black line denotes the amplitude with the directly affecting

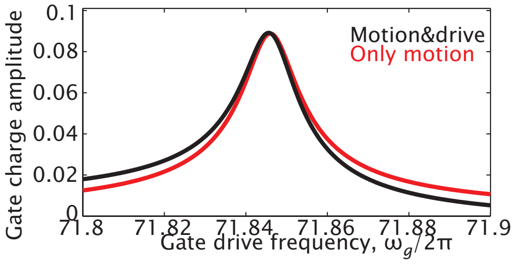

Fig. 3.11: Total gate charge modulation amplitude with both gate motion and drive.

voltage drive taken into account. Exactly at the mechanical resonance, the mechanical motion lags $\Theta = \pi/2$ in phase the gate drive. With a frequency below the resonance, the drive and motion will add up to each other and the amplitude is higher than expected from simple motion modulation. With frequencies above the resonance, drive will cancel part of the motion induced amplitude. Figure 3.11 is plotted assuming gate voltage $V_g = 0.8$ V to underline the asymmetry effect. With higher gate voltages the asymmetry around the mechanical resonant frequency becomes smaller because the motional gate charge modulation starts to dominate the direct voltage modulation of gate charge.

3.4.4 Dynamical sweet spot with voltage modulation

As we saw above, the gate charge modulation of a suitably chosen amplitude will make the quasienergies of the system almost independent of the static gate charge. This indicates that electrical fluctuators affecting the qubit gate charge would not couple to the transition frequency and thus would not dephase the qubit. From this point of view, the gate charge modulation acts like a continuous spin echo [72] cancelling noise that is slower than the modulation.

In this section, we try to formulate the above proposition of protection from voltage noise more formally. We desire to couple the qubit to mechanics while simultaneously adding extra low-frequency voltage drive to protect the qubit from dephasing. We consider the Floquet Hamiltonian of the previous section where the qubit Hamiltonian is replaced with a qubit-mechanics Hamiltonian. The Hamiltonian is thus

$$\hat{H} = \hat{H}_0 + \hbar g(\hat{n} - n_g)(\hat{b}^\dagger + \hat{b}) + \hbar\omega_m \hat{b}^\dagger \hat{b} + 8E_C(\hat{n} - n_g(t))\Delta n_g \cos(\omega_g t), \quad (3.82)$$

where $\hat{H}_0$ is the static qubit Hamiltonian and ω_g is the frequency of the gate charge modulation. Similarly to the study of qubit-mechanics coupling in the

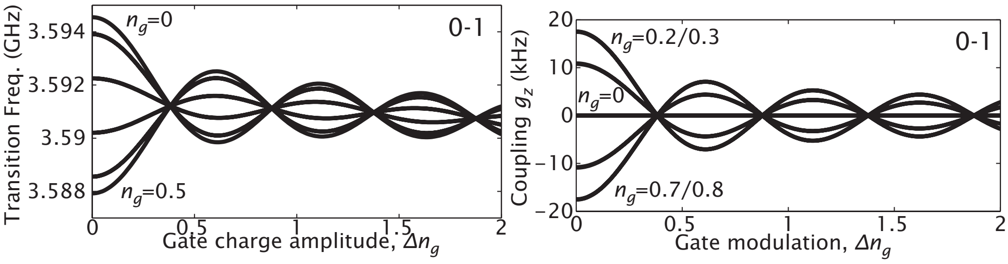

Fig. 3.12: Coupling of mechanics to qubit with driven gate. (a) Transition frequency between the ground and the first excited state as a function of the gate modulation amplitude at six gate charge points, $n_g = [0, ..., 0.5]$. (b) Longitudinal coupling between the mechanics and qubit at different gate charge points.

transmon regime, we can study the coupling term between the qubit and mechanics in the quasienergy state basis and write

$$\hat{H}_{\text{int}} = \hbar \sum_{i,j} g_{ij} |i\rangle\langle j| (\hat{b}^\dagger + \hat{b}), \tag{3.83}$$

where $|i\rangle$ is the quasienergy state of the system including only the static qubit Hamiltonian and the gate charge drive. The coupling terms in the new basis are

$$g_{ij} = g\langle i|\hat{n} - n_g|j\rangle. \tag{3.84}$$

To model the measurements of Publication **IV**, the mechanics coupling to $\hat{\sigma}_z$ is presented in the quasienergy basis in Fig. 3.12. In Fig. 3.12(a), the transition frequency between the ground and the first excited state is depicted at six different static gate charge points, $n_g = [0, ..., 0.5]$. Other gate charge points are omitted for clarity, but all the lines cross each other roughly at the same point as these lines.

In Fig. 3.12(b), the longitudinal coupling is given as a function of the gate modulation assuming $g/2\pi = 4.5$ MHz at different gate charge points. The transversal coupling is not shown but it remains roughly constant at around $g_x = 3.8$ MHz. The figure indicates that the longitudinal coupling does indeed vanish at the dynamical sweet spots while transversal coupling remains. Thus, unpreventable coupling to defects does not decohere the qubit while the desired coupling to mechanics can be maintained by longitudinal sideband drive of the qubit.

The results suggest to try a similar technique with qubits in the charge-qubit regime. As we have noted earlier, the coupling to mechanics would be maximized with low total capacitance of the qubit. If the gate voltage drive would create quasienergy states to which the two-level fluctuators slower than the drive would not couple longitudinally, the system could be used as a very sensitive as well as coherent measurement device for the mechanical resonator.

3.5 Master equation model

The total system is composed of a mechanical resonator, a superconducting qubit, and a co-planar waveguide cavity which measures the state of the qubit. The evolution of the system state can be modeled using a Master equation approach which incorporates decoherence that is caused by the surrounding environment. These loss terms are essential to include because they enable energy to escape and allow sideband cooling, for example. Solving the full time dynamics, however, is a substantial computational task for two coupled systems let alone for the three-partite system discussed here.

In this section, we derive a set of coupled differential equations which model the time-evolution of system expectation values. Such equations are computationally far less intensive to solve and yet still provide expectation values which are relevant in actual experiments. To obtain a finite set of differential equations, approximations have to be made about correlations between the operators. On one hand, these approximations reduce the computational load by disregarding unnecessary information, but on the other hand, they make the model fail in certain physical situations. For example, the Rabi frequency between the mechanics and the qubit depends on the number of quanta in the mechanical resonator. For pure Fock states, the mechanical occupation is expected to oscillate with a well-defined frequency. If losses are included, the actual state will evolve into a mixed state with the occupation expectation value now representing the oscillations with two different frequencies. The approach with differential equations can model this only if sufficiently high order correlations are taken into account and if the infinite series is truncated correctly.

In the following, we present a set of equations that are reduced to as few equations as reasonable to model the physics we are interested in. Two ways of factorizing are introduced; one is suitable for the general case but fails for red-detuned drive close to the mechanical ground state. The other factorization, however, is able to model the limits of sideband cooling where mechanical occupation above one is unlikely.

3.5.1 Master equation

The evolution of the density operator $\hat{\rho}$ can be described in the presence of coupling to the environment by the master equation [73]

$$\begin{aligned}\dot{\hat{\rho}} =& -\frac{i}{\hbar}\left[\hat{H}_S, \hat{\rho}\right] + \kappa\mathcal{D}[\hat{a}]\hat{\rho} + \kappa_m(N_m+1)\mathcal{D}[\hat{b}]\hat{\rho} + \kappa_m N_m \mathcal{D}[\hat{b}^\dagger]\hat{\rho} \\ & + \gamma_1\mathcal{D}[\hat{\sigma}_-]\hat{\rho} + \frac{\gamma_\phi}{2}\mathcal{D}[\hat{\sigma}_z]\hat{\rho}, \end{aligned} \tag{3.85}$$

where $\mathcal{D}[\hat{A}]\hat{\rho} = \hat{A}\hat{\rho}\hat{A}^\dagger - \hat{A}^\dagger\hat{A}\hat{\rho}/2 - \hat{\rho}\hat{A}^\dagger\hat{A}/2$ and $\hat{H}_S$ is the total system Hamiltonian including the qubit, CPW cavity, mechanics, their interactions, and externally applied drives

$$\begin{aligned}\hat{H}_S =& \frac{\hbar}{2}\omega_a\hat{\sigma}_z + \hbar\omega_r\hat{a}^\dagger\hat{a} + \hbar\omega_m\hat{b}^\dagger\hat{b} + \hbar\chi\hat{\sigma}_z\left(\hat{a}^\dagger\hat{a} + \frac{1}{2}\right) + \hbar g_x(\hat{b}^\dagger + \hat{b})\hat{\sigma}_x \\ & + \hbar g_z(\hat{b}^\dagger + \hat{b})\hat{\sigma}_z + \hbar\Omega_x(t)\hat{\sigma}_x\cos(\omega_s t) + \hbar\Omega_z(t)\hat{\sigma}_z\cos(\omega_s t), \end{aligned} \tag{3.86}$$

where ω_r is the frequency of the electrical cavity and $\Omega_x(t)$ ($\Omega_z(t)$) is the envelope for the qubit drive in $\hat{\sigma}_x$ ($\hat{\sigma}_z$) direction. κ is the decay rate of the electrical cavity, κ_m is the decay rate of the mechanics, and $\gamma_1 = 1/T_1$ is the decay rate of the qubit. γ_ϕ is the pure dephasing rate of the qubit.

To lighten the computational load, we can solve only the time evolution of expectation values and avoid solving the full system dynamics. The expectation value of operator $\hat{A}$ is given by

$$\langle\hat{A}\rangle = \mathrm{tr}\left\{\hat{A}\hat{\rho}\right\}. \tag{3.87}$$

In the Schrödinger picture, the operators are time-independent and the expectation value time-evolution is simply given by

$$\frac{\mathrm{d}\langle\hat{A}\rangle}{\mathrm{dt}} = \mathrm{tr}\left\{\hat{A}\frac{\mathrm{d}\hat{\rho}}{\mathrm{dt}}\right\}. \tag{3.88}$$

The time dynamics are now given by a coupled set of ordinary differential equations. The expectation value equations for lower order operators will in general include terms of higher order expectation values and the set of equations is initially infinite. This reflects the fact that no approximation has been made so far and no computational gain can therefore be expected versus solving the full time dynamics. To truncate the infinite series, approximations have to be made regarding the correlations of the operators such that $\langle\hat{A}\hat{B}\rangle \approx \langle\hat{A}\rangle\langle\hat{B}\rangle$, where $\hat{A}$ and $\hat{B}$ are some operators. In the following, we consider how this choice of factorization can be made for a qubit coupled to mechanics.

3.5.2 Qubit and mechanical resonator

Let us first neglect the CPW cavity in order to concentrate on qubit-mechanics coupling. Intuitively, one should include at least some correlation between the qubit and the mechanics to reproduce sideband transitions correctly. In the transmon regime, the coupling is transversal and considering the effect of coupling on higher order correlations, e.g., for $\langle\hat{b}\hat{\sigma}_y\rangle$

$$\frac{\mathrm{d}\langle\hat{b}\hat{\sigma}_y\rangle}{\mathrm{dt}} = -2g_x\langle(\hat{b}^\dagger\hat{b} + \hat{b}\hat{b} + 1/2)\hat{\sigma}_z\rangle, \tag{3.89}$$

one ends up with a choice for factorization. To retain the correlation between mechanics occupation and qubit occupation, we approximate the correlation by factorizing

$$\begin{aligned}\frac{\mathrm{d}\langle\hat{b}\hat{\sigma}_y\rangle}{\mathrm{dt}} =& - 2g_x\langle\hat{b}^\dagger\hat{b}\hat{\sigma}_z\rangle - 2g_x\langle\hat{b}\hat{b}\hat{\sigma}_z\rangle - g_x\langle\hat{\sigma}_z\rangle \\ \approx& - 2g_x\langle\hat{b}^\dagger\hat{b}\hat{\sigma}_z\rangle - 2g_x\langle\hat{b}\rangle\langle\hat{b}\hat{\sigma}_z\rangle - g_x\langle\hat{\sigma}_z\rangle. \end{aligned} \tag{3.90}$$

The highest correlation which we keep track of is $\langle\hat{b}^\dagger\hat{b}\hat{\sigma}_z\rangle$. Time evolution for that has a term due to the transversal coupling

$$\begin{aligned}\frac{\mathrm{d}\langle\hat{b}^\dagger\hat{b}\hat{\sigma}_z\rangle}{\mathrm{dt}} =& 4g_x\mathrm{Re}\langle\hat{b}^\dagger\hat{b}\hat{b}\hat{\sigma}_y\rangle + 2g_x\mathrm{Re}\langle\hat{b}\hat{\sigma}_y\rangle \\ \approx& 4g_x\langle\hat{b}^\dagger\hat{b}\rangle\mathrm{Re}\langle\hat{b}\hat{\sigma}_y\rangle + 2g_x\mathrm{Re}\langle\hat{b}\hat{\sigma}_y\rangle \\ \approx& 4g_x\langle\hat{b}^\dagger\hat{b}\rangle\mathrm{Re}\langle\hat{b}\hat{\sigma}_y\rangle + 2g_x\langle\hat{\sigma}_z\rangle\mathrm{Im}\langle\hat{b}\hat{\sigma}_x\rangle, \end{aligned} \tag{3.91}$$

where we have used $\mathrm{Re}\langle\hat{b}\hat{\sigma}_y\rangle = \mathrm{Re}\langle\hat{b}\hat{\sigma}_z\hat{\sigma}_z\hat{\sigma}_y\rangle = \mathrm{Im}\langle\hat{b}\hat{\sigma}_z\hat{\sigma}_x\rangle \approx \langle\hat{\sigma}_z\rangle\mathrm{Im}\langle\hat{b}\hat{\sigma}_x\rangle$.

Writing out all the equations with only $\hat{\sigma}_x$ coupling and $\hat{\sigma}_z$ drive considered

$$d_t\langle b\rangle = - ig_x\langle\hat{\sigma}_x\rangle - i\omega_m\langle b\rangle \tag{3.92}$$

$$d_t\langle\hat{\sigma}_z\rangle = + 4g_x\mathrm{Re}\langle b\hat{\sigma}_y\rangle \tag{3.93}$$

$$d_t\langle\hat{\sigma}_x\rangle = - \omega_a\langle\hat{\sigma}_y\rangle - 2\Omega_z(t)\langle\hat{\sigma}_y\rangle\cos(\omega_s t) \tag{3.94}$$

$$d_t\langle\hat{\sigma}_y\rangle = + \omega_a\langle\hat{\sigma}_x\rangle - 4g_x\mathrm{Re}\langle b\hat{\sigma}_z\rangle + 2\Omega_z(t)\langle\hat{\sigma}_x\rangle\cos(\omega_s t) \tag{3.95}$$

$$d_t\langle b\hat{\sigma}_z\rangle = + 2g_x\langle\hat{b}^\dagger b\rangle\langle\hat{\sigma}_y\rangle + g_x\langle\hat{\sigma}_y\rangle + 2g_x\langle b\rangle\langle b\hat{\sigma}_y\rangle - i\omega_m\langle b\hat{\sigma}_z\rangle \tag{3.96}$$

$$d_t\langle b\hat{\sigma}_x\rangle = - \omega_a\langle b\hat{\sigma}_y\rangle - ig_x - i\omega_m\langle b\hat{\sigma}_x\rangle - 2\Omega_z(t)\langle b\hat{\sigma}_y\rangle\cos(\omega_s t) \tag{3.97}$$

$$\begin{aligned}d_t\langle b\hat{\sigma}_y\rangle =& + \omega_a\langle b\hat{\sigma}_x\rangle - 2g_x\langle\hat{b}^\dagger b\hat{\sigma}_z\rangle - g_x\langle\hat{\sigma}_z\rangle - 2g_x\langle b\rangle\langle b\hat{\sigma}_z\rangle - i\omega_m\langle b\hat{\sigma}_y\rangle \\ &+ 2\Omega_z(t)\langle b\hat{\sigma}_x\rangle\cos(\omega_s t)\end{aligned} \tag{3.98}$$

$$d_t\langle\hat{b}^\dagger b\rangle = - 2g_x\mathrm{Im}\langle b\hat{\sigma}_x\rangle \tag{3.99}$$

$$d_t\langle\hat{b}^\dagger b\hat{\sigma}_z\rangle = + 4g_x\langle\hat{b}^\dagger b\rangle\mathrm{Re}\langle b\hat{\sigma}_y\rangle + 2g_x\langle\hat{\sigma}_z\rangle\mathrm{Im}\langle b\hat{\sigma}_x\rangle, \tag{3.100}$$

where we have neglected the loss terms and approximated $\langle\hat{b}^\dagger\hat{b}\hat{\sigma}_y\rangle \approx \langle\hat{b}^\dagger\hat{b}\rangle\langle\hat{\sigma}_y\rangle$, $\langle\hat{b}\hat{b}\hat{\sigma}_y\rangle \approx \langle\hat{b}\rangle\langle\hat{b}\hat{\sigma}_y\rangle$.

In order to find the essential terms for sideband Rabi oscillations, consider the initial state of mechanics being a Fock state and the initial state of the qubit being either the ground or the excited state. Approximating $\mathrm{Re}\langle b\hat{\sigma}_z\rangle = 0$ implies that both $\langle\hat{\sigma}_x\rangle$ and $\langle\hat{\sigma}_y\rangle$ remain zero throughout the evolution. Furthermore, since initially $\langle\hat{b}\rangle = 0$, also the expectation value of the mechanical annihilation operator remains zero. This in turn implies that not only the real part but $\langle b\hat{\sigma}_z\rangle = 0$. The set of five equations then reads

$$d_t\langle\hat{\sigma}_z\rangle = +\,4g_x\mathrm{Re}\langle b\hat{\sigma}_y\rangle \tag{3.101}$$

$$d_t\langle b\hat{\sigma}_x\rangle = -\,\omega_a\langle b\hat{\sigma}_y\rangle - ig_x - i\omega_m\langle b\hat{\sigma}_x\rangle - 2\Omega_z(t)\langle b\hat{\sigma}_y\rangle\cos(\omega_s t) \tag{3.102}$$

$$\begin{aligned} d_t\langle b\hat{\sigma}_y\rangle = &+\,\omega_a\langle b\hat{\sigma}_x\rangle - 2g_x\langle\hat{b}^\dagger b\hat{\sigma}_z\rangle - g_x\langle\hat{\sigma}_z\rangle - i\omega_m\langle b\hat{\sigma}_y\rangle \\ &+ 2\Omega_z(t)\langle b\hat{\sigma}_x\rangle\cos(\omega_s t) \end{aligned} \tag{3.103}$$

$$d_t\langle\hat{b}^\dagger b\rangle = -\,2g_x\mathrm{Im}\langle b\hat{\sigma}_x\rangle \tag{3.104}$$

$$d_t\langle\hat{b}^\dagger b\hat{\sigma}_z\rangle = +\,4g_x\langle\hat{b}^\dagger b\rangle\mathrm{Re}\langle b\hat{\sigma}_y\rangle + 2g_x\langle\hat{\sigma}_z\rangle\mathrm{Im}\langle b\hat{\sigma}_x\rangle. \tag{3.105}$$

This set of five equations is sufficient to reproduce both the red and blue sideband Rabi oscillations. In Fig. 3.13, the mechanics and qubit population expectation values are plotted when the qubit $\hat{\sigma}_z$ drive is perfectly tuned to the red sideband. For perfect detuning, the driving frequency is shifted by $2\hbar\chi_m\hat{b}^\dagger\hat{b}$ to take into account the ac Stark shift, see Eq. (3.68). The qubit is initially in the ground state and mechanics is in Fock state $|1\rangle$, $|2\rangle$, or $|3\rangle$. In Fig. 3.13(b), the analytically expected Rabi oscillation of the qubit is also plotted based on Eq. (3.47), $\langle\hat{\sigma}_z\rangle = 2\sin(At)^2 - 1$. The numerical calculation agrees very well with the analytical formula, thus showing that we managed to keep all the necessary terms in our choice of factorization. Similarly on the blue sideband, the five equations are able to reproduce the analytical results.

It is worth noting that the only nonlinear term in these five equations (Eqs. (3.101-3.105)) is in the equation for the highest order term $\langle\hat{b}^\dagger b\hat{\sigma}_z\rangle$, see Eq. (3.105). It is therefore exactly this term that produces the necessary nonlinear dependency of the Rabi frequencies as a function of the mechanical occupation. Any approximation which linearizes this term would render the sideband Rabi frequencies independent of phonon number.

Furthermore, the qubit drive is here assumed to be classical with no quantum or classical noise (Eq. (3.86))). Therefore the model does not take into account the phase noise of drive which becomes important in the ground-state sideband

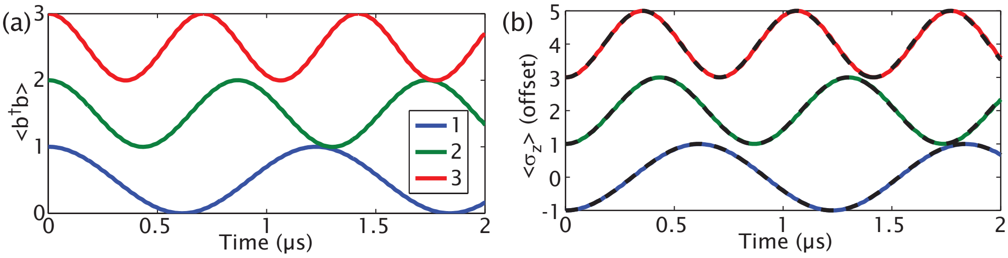

Fig. 3.13: Sideband Rabi oscillations in the transmon regime with no losses. Expectation value for (a) mechanics population and (b) qubit $\hat{\sigma}_z$-operator (offset for clarity). The driving frequency was chosen to be perfectly detuned (taking into account the Stark shift due to the mechanics occupation). The parameters used were $\omega_a/2\pi = 5\text{GHz}$, $\omega_m/2\pi = 100\text{MHz}$, $g_x/2\pi = 20\text{MHz}$, and $\Omega_z(t)/2\pi = 100\text{MHz}$. The dashed lines in (b) are plotted using $\langle\hat{\sigma}_z\rangle = 2\sin(At)^2 - 1$ with A given by Eq. (3.47).

cooling with a mechanical resonator coupled to a harmonic cavity, see for example [31].

Also, since only two levels of the qubit are considered, the Stark shift is greatly exaggerated by the model in the transmon regime where the third level almost cancels the Stark shift. Since the drive is classical and no two-photon coupling terms are present, even the inclusion of a third energy level would not take into account two photon excitations of the qubit from ground state to the second excited state, a phenomenon which is observed with strong qubit drives.

The measurement of qubit state using the CPW cavity can be taken into account by adding the terms that correspond to the cavity presented in Ref. [74]. Simply adding these terms is equal to neglecting higher order correlations between all these three systems and is a reasonable approximation in many situations. The computational load of these extra equations is very small and here they are neglected to keep the set of equations as small as possible.

3.5.3 Inclusion of losses

The loss terms for the five equations (3.101)-(3.105) are

$$d_t\langle\hat{\sigma}_z\rangle^{\text{loss}} = -\gamma_1\left(1 + \langle\hat{\sigma}_z\rangle\right) \tag{3.106}$$

$$d_t\langle b\hat{\sigma}_x\rangle^{\text{loss}} = -\frac{\gamma_1}{2}\langle b\hat{\sigma}_x\rangle - \gamma_\phi\langle b\hat{\sigma}_x\rangle - \frac{\kappa_m}{2}\langle b\hat{\sigma}_x\rangle \tag{3.107}$$

$$d_t\langle b\hat{\sigma}_y\rangle^{\text{loss}} = -\frac{\gamma_1}{2}\langle b\hat{\sigma}_y\rangle - \gamma_\phi\langle b\hat{\sigma}_y\rangle - \frac{\kappa_m}{2}\langle b\hat{\sigma}_y\rangle \tag{3.108}$$

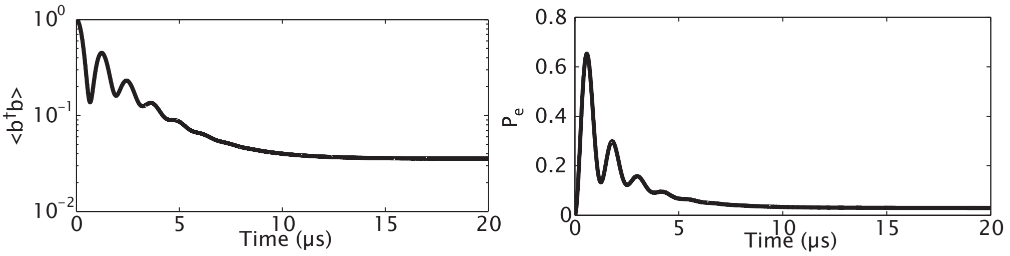

Fig. 3.14: Expectation values of the mechanics and qubit excited state occupation with the qubit driven at the red-detuned mechanical sideband. The parameters used are $\omega_a/2\pi = 5$ GHz, $\omega_m/2\pi = 100$ MHz, $g_x/2\pi = 20$ MHz, $\Omega_z(t)/2\pi = 100$ MHz, Q=100,000, $T = 25$ mK, and $\gamma_1 = \gamma_\phi = 1$ MHz. Initial state is $|0,1\rangle$

$$d_t\langle\hat{b}^\dagger b\rangle^{\text{loss}} = -\kappa_m\left(\langle\hat{b}^\dagger b\rangle - N_m\right) \tag{3.109}$$

$$d_t\langle\hat{b}^\dagger b\hat{\sigma}_z\rangle^{\text{loss}} = -\gamma_1\left(\langle\hat{b}^\dagger b\rangle + \langle\hat{b}^\dagger b\hat{\sigma}_z\rangle\right) - \kappa_m\left(\langle\hat{b}^\dagger b\hat{\sigma}_z\rangle - N_m\langle\hat{\sigma}_z\rangle\right), \tag{3.110}$$

where $N_m = \left(e^{\hbar\omega_b/k_bT_m} - 1\right)^{-1}$. With these terms taken into account, the approximations of the previous section break down. As the number of excitations start to leak out of the system, the Rabi frequency becomes unphysically dependent on the expected phonon number which can be non-integer. To study the sideband cooling limit, we can break the Rabi frequency dependency by approximating $\langle\hat{b}^\dagger\hat{b}\hat{b}\hat{\sigma}_y\rangle \approx 0$, which changes the Eq. (3.105) to

$$d_t\langle\hat{b}^\dagger b\hat{\sigma}_z\rangle = +2g_x\text{Re}\langle b\hat{\sigma}_y\rangle. \tag{3.111}$$

With this approximation, the rate of sideband transitions is fixed to the same as with one quantum in the mechanical resonator and is thus not valid for modeling resonator states which have a nonnegligible contribution from two or higher quanta occupations. The approximation, however, allows us to model asymptotic cooling limits where the expected phonon occupancy lies below one.

In figure 3.14, a modeled cooling run is shown with the mechanics starting from a phonon occupancy of one. The thermal bath for mechanics is taken to be at 25 mK which corresponds to an average occupancy of 4.7 quanta if $\omega_m/2\pi =$ 100 MHz. The initial state is thus not a thermal state. Nevertheless, the final occupancy of 0.036 quanta gives an estimate for the efficiency of the cooling scheme [75, 76]. The final occupancy of the mechanics is shown in Fig. 3.15 as a function of the sideband drive frequency detuning from the qubit transition frequency.

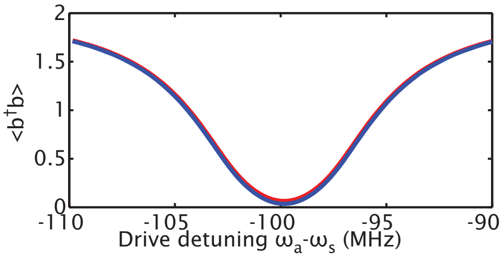

Fig. 3.15: Expectation value of mechanics occupation (blue solid line) with the qubit driven around the red-detuned mechanical sideband. The red solid line denotes the total number of excitation of the system including the qubit. At the occupation minimum of mechanics, the qubit excited state occupation is 0.030 and the mechanics occupation is 0.036. The parameters used are $\omega_a/2\pi = 5$ GHz, $\omega_m/2\pi = 100$ MHz, $g_x/2\pi = 20$ MHz, $\Omega_z(t)/2\pi = 100$ MHz, Q=100,000, $T = 25$ mK, and $\gamma_1 = \gamma_\phi = 1$ MHz. Initial state is $|0, 1\rangle$ and the simulation time is 50 μs.

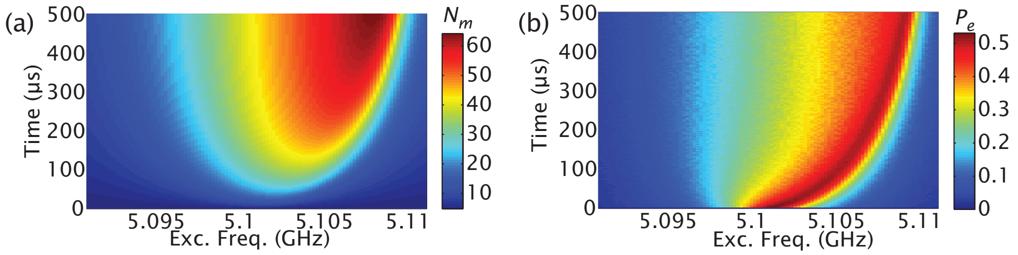

Fig. 3.16: Expectation values of the (a) mechanics and (b) qubit excited state with the qubit driven around the blue-detuned mechanical sideband. The two-level model exaggerates the Stark shift and thus the qubit transition frequency shifts noticeably up in frequency. The parameters used are as in Fig. 3.15 except that the initial state of mechanics is thermal state at 25 mK.

Starting from the thermal occupation of mechanics, the code can also be used to model experiments with a blue-detuned qubit drive, see Fig. 3.16. The master equation simulation is based on a two-level approximation of the transmon qubit which in the transmon limit fails to correctly predict the Stark shift. Therefore in Fig. 3.16, the qubit eigenfrequency is strongly affected by the added phonons and equilibrium is approached very slowly and the resulting lineshapes of qubit and mechanics are very asymmetric. The computational load, however, is light and the addition of the third qubit eigenlevel should allow for the blue-detuned sideband regime to be modeled correctly.

Chapter 4

Summary and conclusions

We have so far managed to demonstrate coherent manipulation of qubit state using a classical mechanical field and a sideband qubit drive. The analysis that I have presented here shows that it is possible to extend this coherent coupling deeper into the transmon qubit regime. To obtain the required level of coupling, the qubit-mechanics coupling has to be enhanced only moderately by either physical changes to the resonator or by applying a larger gate voltage. Applying as large longitudinal driving to the qubit as possible, coherent state transfer from qubit to mechanics and back should be attained with coherence times around microseconds.

Master equation modeling indicates that the mechanical resonator can be cooled close to quantum ground state using the qubit as a dissipative channel. Combined with the state transfer above, this should enable creation of highly nonclassical quantum states to be prepared into the mechanical resonator with negative Wigner densities.

In the regime of linear optomechanics, we have demonstrated that a mechanical resonator coupled to an electrical resonator can be operated as a low-noise amplifier of electrical signals. We have also shown that, in principle, such a system could be used as a quantum-limited amplifier if the mechanical resonator could be cooled to its ground state.

The stamp technique presented in Publication **VI** possibly allows realizing small gaps between the mechanical resonator and the gate. An aluminum membrane transferred using micromanipulation should always lie very close to the electrodes such that some part of it is vibrating just a few nanometers away from it. If the aluminum resonator is large, such that it can extend over both ends of a meandering cavity and if it is supported by both of them, large optomechanical coupling to the cavity should be reached.

In a wider perspective, the field of optomechanics has just begun. The trend towards evermore macroscopic mechanical resonators can soon enable fundamental tests of reality. It has been proposed that optomechanical systems could be used to probe the quantized nature of gravitation in a table-top experiment [77].

As more and more physical implementations of optomechanical systems cross over to the strong coupling regime, opportunities arise to employ them as transducers between otherwise incompatible degrees of freedom [78, 79]. An optical network could be used for communicating quantum states and for creating entanglement between distant mechanical resonators. Such composite systems can be used to test Bell's inequality between mechanical systems that are far apart, for example, by boarding one of them on a satellite.

Realizing the strong coupling between qubits and mechanical resonators connects the toolbox of optomechanics to be used in quantum information processing. As the environment of qubits has to be carefully engineered to prevent decoherence, mechanical resonators could be potentially used as clean interfaces for coupling quantum coherent systems and storing quantum information.

The potential of enhancing optomechanical coupling with Josephson junctions is not confined to qubits only. A recent proposal outlines Josephson enhanced optomechanical coupling which can bring optomechanics in to the regime of single phonon strong coupling [80]. Such a strong coupling can provide crucial nonlinear components and could be used for example in single photon detection.

References

[1] Cavendish, H. Experiments to determine the density of the earth. *Phil. Trans. R. Soc. Lond.* **88**, 469–526 (1798). URL `http://dx.doi.org/10.1098/rstl.1798.0022`.

[2] Coulomb, C. Où l'on détermine, suivant quelles lois le fluide magnétique, ainsi que le fluide électrique, agissent, soit par répulsion, soit par attraction. *Mémoires de L'Académie Royale des sciences* **88**, 578–611 (1788). URL `http://www.academie-sciences.fr/activite/archive/dossiers/Coulomb/Coulomb_pdf/Mem1785_p578.pdf`.

[3] Binnig, G., Quate, C. F. & Gerber, C. Atomic force microscope. *Phys. Rev. Lett.* **56**, 930–933 (1986). URL `http://link.aps.org/doi/10.1103/PhysRevLett.56.930`.

[4] Clubb, D., Buu, O., Bowley, R., Nyman, R. & Owers-Bradley, J. Quartz tuning fork viscometers for helium liquids. *Journal of Low Temperature Physics* **136**, 1–13 (2004). URL `http://dx.doi.org/10.1023/B%3AJOLT.0000035368.63197.16`.

[5] Kepler, J. *De cometis libelli tres* (A. Apergeri, 1619).

[6] Lebedew, P. Untersuchungen über die druckkräfte des lichtes. *Ann. Phys.* **311**, 433–458 (1901). URL `http://dx.doi.org/10.1002/andp.19013111102`.

[7] Nichols, E. F. & Hull, G. F. A preliminary communication on the pressure of heat and light radiation. *Phys. Rev. (Series I)* **13**, 307–320 (1901). URL `http://link.aps.org/doi/10.1103/PhysRevSeriesI.13.307`.

[8] Dorsel, A., McCullen, J. D., Meystre, P., Vignes, E. & Walther, H. Optical bistability and mirror confinement induced by radiation pressure. *Phys.*

Rev. Lett. **51**, 1550–1553 (1983). URL `http://link.aps.org/doi/10.1103/PhysRevLett.51.1550`.

[9] Aufmuth, P. & Danzmann, K. Gravitational wave detectors. *New Journal of Physics* **7**, 202 (2005). URL `http://stacks.iop.org/1367-2630/7/i=1/a=202`.

[10] Arcizet, O., Cohadon, P. F., Briant, T., Pinard, M. & Heidmann, A. Radiation-pressure cooling and optomechanical instability of a micromirror. *Nature* **444**, 71–74 (2006). URL `http://dx.doi.org/10.1038/nature05244`.

[11] Gröblacher, S., Hammerer, K., Vanner, M. R. & Aspelmeyer, M. Observation of strong coupling between a micromechanical resonator and an optical cavity field. *Nature* **460**, 724–727 (2009). URL `http://dx.doi.org/10.1038/nature08171`.

[12] Verhagen, E., Deleglise, S., Weis, S., Schliesser, A. & Kippenberg, T. J. Quantum-coherent coupling of a mechanical oscillator to an optical cavity mode. *Nature* **482**, 63–67 (2012). URL `http://dx.doi.org/10.1038/nature10787`.

[13] Safavi-Naeini, A. H. *et al.* Electromagnetically induced transparency and slow light with optomechanics. *Nature* **472**, 69–73 (2011). URL `http://dx.doi.org/10.1038/nature09933`.

[14] Teufel, J. D., Harlow, J. W., Regal, C. A. & Lehnert, K. W. Dynamical backaction of microwave fields on a nanomechanical oscillator. *Phys. Rev. Lett.* **101**, 197203 (2008). URL `http://link.aps.org/doi/10.1103/PhysRevLett.101.197203`.

[15] Sillanpää, M. A., Sarkar, J., Sulkko, J., Muhonen, J. & Hakonen, P. J. Accessing nanomechanical resonators via a fast microwave circuit. *Applied Physics Letters* **95**, 011909–011909–3 (2009). URL `http://dx.doi.org/10.1063/1.3173826`.

[16] Sulkko, J. *et al.* Strong gate coupling of high-Q nanomechanical resonators. *Nano Letters* **10**, 4884–4889 (2010). URL `http://pubs.acs.org/doi/abs/10.1021/nl102771p`.

[17] Teufel, J. D. *et al.* Circuit cavity electromechanics in the strong-coupling regime. *Nature* **471**, 204–208 (2011). URL `http://dx.doi.org/10.1038/nature09898`.

[18] O'Connell, A. D. *et al.* Quantum ground state and single-phonon control of a mechanical resonator. *Nature* **464**, 697–703 (2010). URL `http://dx.doi.org/10.1038/nature08967`.

[19] Teufel, J. D. *et al.* Sideband cooling of micromechanical motion to the quantum ground state. *Nature* **475**, 359–363 (2011). URL `http://dx.doi.org/10.1038/nature10261`.

[20] Chan, J. *et al.* Laser cooling of a nanomechanical oscillator into its quantum ground state. *Nature* **478**, 89–92 (2011). URL `http://dx.doi.org/10.1038/nature10461`.

[21] Fabre, C. *et al.* Quantum-noise reduction using a cavity with a movable mirror. *Phys. Rev. A* **49**, 1337–1343 (1994). URL `http://link.aps.org/doi/10.1103/PhysRevA.49.1337`.

[22] Mancini, S. & Tombesi, P. Quantum noise reduction by radiation pressure. *Phys. Rev. A* **49**, 4055–4065 (1994). URL `http://link.aps.org/doi/10.1103/PhysRevA.49.4055`.

[23] Mancini, S., Man'ko, V. I. & Tombesi, P. Ponderomotive control of quantum macroscopic coherence. *Phys. Rev. A* **55**, 3042–3050 (1997). URL `http://link.aps.org/doi/10.1103/PhysRevA.55.3042`.

[24] Caves, C. M., Thorne, K. S., Drever, R. W. P., Sandberg, V. D. & Zimmermann, M. On the measurement of a weak classical force coupled to a quantum-mechanical oscillator. I. Issues of principle. *Rev. Mod. Phys.* **52**, 341–392 (1980). URL `http://link.aps.org/doi/10.1103/RevModPhys.52.341`.

[25] Palomaki, T. A., Teufel, J. D., Simmonds, R. W. & Lehnert, K. W. Entangling mechanical motion with microwave fields. *Science* **342**, 710–713 (2013). URL `http://www.sciencemag.org/content/342/6159/710.abstract`.

[26] Raimond, J. M., Brune, M. & Haroche, S. Manipulating quantum entanglement with atoms and photons in a cavity. *Rev. Mod. Phys.* **73**, 565–582 (2001). URL `http://link.aps.org/doi/10.1103/RevModPhys.73.565`.

[27] Leibfried, D., Blatt, R., Monroe, C. & Wineland, D. Quantum dynamics of single trapped ions. *Rev. Mod. Phys.* **75**, 281–324 (2003). URL `http://link.aps.org/doi/10.1103/RevModPhys.75.281`.

[28] Song, X. *et al.* Stamp transferred suspended graphene mechanical resonators for radio frequency electrical readout. *Nano Letters* **12**, 198–202 (2012). URL `http://pubs.acs.org/doi/abs/10.1021/nl203305q`.

[29] Liboff, R. L. *Introductory Quantum Mechanics*, chap. 7.2. (Addison-Wesley, 2003).

[30] Hertzberg, J. B. *Back-action evading measurements of nanomechanical motion approaching quantum limits*. Ph.D. thesis, University of Maryland (2009). URL `http://www.kschwabresearch.com/files/publications/hertzberg_thesis.pdf`.

[31] Aspelmeyer, M., Kippenberg, T. J. & Marquardt, F. Cavity Optomechanics. *ArXiv e-prints* (2013). URL `http://arxiv.org/abs/1303.0733`.

[32] Bose, S., Jacobs, K. & Knight, P. L. Preparation of nonclassical states in cavities with a moving mirror. *Phys. Rev. A* **56**, 4175–4186 (1997). URL `http://link.aps.org/doi/10.1103/PhysRevA.56.4175`.

[33] Genes, C., Vitali, D., Tombesi, P., Gigan, S. & Aspelmeyer, M. Ground-state cooling of a micromechanical oscillator: Comparing cold damping and cavity-assisted cooling schemes. *Phys. Rev. A* **77**, 033804 (2008). URL `http://link.aps.org/doi/10.1103/PhysRevA.77.033804`.

[34] Giovannetti, V. & Vitali, D. Phase-noise measurement in a cavity with a movable mirror undergoing quantum brownian motion. *Phys. Rev. A* **63**, 023812 (2001). URL `http://link.aps.org/doi/10.1103/PhysRevA.63.023812`.

[35] Wilson-Rae, I., Nooshi, N., Zwerger, W. & Kippenberg, T. J. Theory of ground state cooling of a mechanical oscillator using dynamical backaction. *Phys. Rev. Lett.* **99**, 093901 (2007). URL `http://link.aps.org/doi/10.1103/PhysRevLett.99.093901`.

[36] Marquardt, F., Chen, J. P., Clerk, A. A. & Girvin, S. M. Quantum theory of cavity-assisted sideband cooling of mechanical motion. *Phys. Rev. Lett.* **99**, 093902 (2007). URL `http://link.aps.org/doi/10.1103/PhysRevLett.99.093902`.

[37] Dobrindt, J. M. & Kippenberg, T. J. Theoretical analysis of mechanical displacement measurement using a multiple cavity mode transducer.

Phys. Rev. Lett. **104**, 033901 (2010). URL `http://link.aps.org/doi/10.1103/PhysRevLett.104.033901`.

[38] Caves, C. M. Quantum limits on noise in linear amplifiers. *Phys. Rev. D* **26**, 1817–1839 (1982). URL `http://link.aps.org/doi/10.1103/PhysRevD.26.1817`.

[39] Clerk, A. A., Devoret, M. H., Girvin, S. M., Marquardt, F. & Schoelkopf, R. J. Introduction to quantum noise, measurement, and amplification. *Rev. Mod. Phys.* **82**, 1155–1208 (2010). URL `http://link.aps.org/doi/10.1103/RevModPhys.82.1155`.

[40] Fleischhauer, M., Imamoglu, A. & Marangos, J. P. Electromagnetically induced transparency: Optics in coherent media. *Rev. Mod. Phys.* **77**, 633–673 (2005). URL `http://link.aps.org/doi/10.1103/RevModPhys.77.633`.

[41] Tinkham, M. *Introduction to Superconductivity: Second Edition* (Dover publications, 2004).

[42] Cottet, A. *Implementation of a quantum bit in a superconducting circuit*. Ph.D. thesis, Université Pierre et Marie Curie-Paris VI (2002). URL `http://www.phys.ens.fr/~cottet/ACottetThesis.pdf`.

[43] Josephson, B. D. Coupled superconductors. *Rev. Mod. Phys.* **36**, 216–220 (1964). URL `http://link.aps.org/doi/10.1103/RevModPhys.36.216`.

[44] Büttiker, M. Zero-current persistent potential drop across small-capacitance Josephson junctions. *Phys. Rev. B* **36**, 3548–3555 (1987). URL `http://link.aps.org/doi/10.1103/PhysRevB.36.3548`.

[45] Ambegaokar, V. & Baratoff, A. Tunneling between superconductors. *Phys. Rev. Lett.* **10**, 486–489 (1963). URL `http://link.aps.org/doi/10.1103/PhysRevLett.10.486`.

[46] Cochran, J. F. & Mapother, D. E. Superconducting transition in aluminum. *Phys. Rev.* **111**, 132–142 (1958). URL `http://link.aps.org/doi/10.1103/PhysRev.111.132`.

[47] Nakamura, Y., Pashkin, Y. A. & Tsai, J. S. Coherent control of macroscopic quantum states in a single-Cooper-pair box. *Nature* **398**, 786–788 (1999). URL `http://dx.doi.org/10.1038/19718`.

[48] Zaretskey, V., Suri, B., Novikov, S., Wellstood, F. C. & Palmer, B. S. Spectroscopy of a Cooper-pair box coupled to a two-level system via charge and critical current. *Phys. Rev. B* **87**, 174522 (2013). URL `http://link.aps.org/doi/10.1103/PhysRevB.87.174522`.

[49] Koch, J. *et al.* Charge-insensitive qubit design derived from the Cooper pair box. *Phys. Rev. A* **76**, 042319 (2007). URL `http://link.aps.org/doi/10.1103/PhysRevA.76.042319`.

[50] Josephson, B. in "Quantum fluids", edited by D. F. Brewer, pp. 174 (North-Holland Publishing Company, Amsterdam, 1966) .

[51] Blais, A., Huang, R.-S., Wallraff, A., Girvin, S. M. & Schoelkopf, R. J. Cavity quantum electrodynamics for superconducting electrical circuits: An architecture for quantum computation. *Phys. Rev. A* **69**, 062320 (2004). URL `http://link.aps.org/doi/10.1103/PhysRevA.69.062320`.

[52] Wallraff, A. *et al.* Strong coupling of a single photon to a superconducting qubit using circuit quantum electrodynamics. *Nature* **431**, 162–167 (2004). URL `http://dx.doi.org/10.1038/nature02851`.

[53] Paik, H. *et al.* Observation of high coherence in Josephson junction qubits measured in a three-dimensional circuit QED architecture. *Phys. Rev. Lett.* **107**, 240501 (2011). URL `http://link.aps.org/doi/10.1103/PhysRevLett.107.240501`.

[54] Rigetti, C. *et al.* Superconducting qubit in a waveguide cavity with a coherence time approaching 0.1 ms. *Phys. Rev. B* **86**, 100506 (2012). URL `http://link.aps.org/doi/10.1103/PhysRevB.86.100506`.

[55] Vion, D. *et al.* Manipulating the quantum state of an electrical circuit. *Science* **296**, 886–889 (2002). URL `http://www.sciencemag.org/content/296/5569/886.abstract`.

[56] Buisson, O. & Hekking, F. Entangled states in a Josephson charge qubit coupled to a superconducting resonator. In Averin, D., Ruggiero, B. & Silvestrini, P. (eds.) *Macroscopic Quantum Coherence and Quantum Computing*, 137–145 (Springer US, 2001). URL `http://dx.doi.org/10.1007/978-1-4615-1245-5_14`.

[57] Kockum, A. F. *et al.* Detailed modelling of the susceptibility of a thermally populated, strongly driven circuit-QED system. *Journal of Physics*

B: Atomic, Molecular and Optical Physics **46**, 224014 (2013). URL `http://stacks.iop.org/0953-4075/46/i=22/a=224014`.

[58] Forn-Díaz, P. *et al.* Observation of the Bloch-Siegert shift in a qubit-oscillator system in the ultrastrong coupling regime. *Phys. Rev. Lett.* **105**, 237001 (2010). URL `http://link.aps.org/doi/10.1103/PhysRevLett.105.237001`.

[59] Niemczyk, T. *et al.* Circuit quantum electrodynamics in the ultrastrong-coupling regime. *Nat Phys* **6**, 772–776 (2010). URL `http://dx.doi.org/10.1038/nphys1730`.

[60] Houck, A. A. *et al.* Controlling the spontaneous emission of a superconducting transmon qubit. *Phys. Rev. Lett.* **101**, 080502 (2008). URL `http://link.aps.org/doi/10.1103/PhysRevLett.101.080502`.

[61] Schrieffer, J. R. & Wolff, P. A. Relation between the Anderson and Kondo Hamiltonians. *Phys. Rev.* **149**, 491–492 (1966). URL `http://link.aps.org/doi/10.1103/PhysRev.149.491`.

[62] Schuster, D. I. *et al.* ac stark shift and dephasing of a superconducting qubit strongly coupled to a cavity field. *Phys. Rev. Lett.* **94**, 123602 (2005). URL `http://link.aps.org/doi/10.1103/PhysRevLett.94.123602`.

[63] Ong, F. R. *et al.* Circuit QED with a nonlinear resonator: ac-Stark shift and dephasing. *Phys. Rev. Lett.* **106**, 167002 (2011). URL `http://link.aps.org/doi/10.1103/PhysRevLett.106.167002`.

[64] Boissonneault, M., Gambetta, J. M. & Blais, A. Dispersive regime of circuit QED: photon-dependent qubit dephasing and relaxation rates. *Phys. Rev. A* **79**, 013819 (2009). URL `http://link.aps.org/doi/10.1103/PhysRevA.79.013819`.

[65] Marquardt, F. & Bruder, C. Superposition of two mesoscopically distinct quantum states: Coupling a Cooper-pair box to a large superconducting island. *Phys. Rev. B* **63**, 054514 (2001). URL `http://link.aps.org/doi/10.1103/PhysRevB.63.054514`.

[66] Diedrich, F., Bergquist, J. C., Itano, W. M. & Wineland, D. J. Laser cooling to the zero-point energy of motion. *Phys. Rev. Lett.* **62**, 403–406 (1989). URL `http://link.aps.org/doi/10.1103/PhysRevLett.62.403`.

[67] Martin, I., Shnirman, A., Tian, L. & Zoller, P. Ground-state cooling of mechanical resonators. *Phys. Rev. B* **69**, 125339 (2004). URL `http://link.aps.org/doi/10.1103/PhysRevB.69.125339`.

[68] Shirley, J. H. Solution of the Schrödinger equation with a Hamiltonian periodic in time. *Phys. Rev.* **138**, B979–B987 (1965). URL `http://link.aps.org/doi/10.1103/PhysRev.138.B979`.

[69] Cohen-Tannoudji, C., Dupont-Roc, J. & Grynberg, G. *Atom-Photon Interactions: Basic Processes and Applications* (J. Wiley, New York, 1992).

[70] Tuorila, J. *et al.* Stark effect and generalized Bloch-Siegert shift in a strongly driven two-level system. *Phys. Rev. Lett.* **105**, 257003 (2010). URL `http://link.aps.org/doi/10.1103/PhysRevLett.105.257003`.

[71] Li, J. *et al.* Motional averaging in a superconducting qubit. *Nat Commun* **4**, 1420 (2013). URL `http://dx.doi.org/10.1038/ncomms2383`.

[72] Nakamura, Y., Pashkin, Y. A., Yamamoto, T. & Tsai, J. S. Charge echo in a Cooper-pair box. *Phys. Rev. Lett.* **88**, 047901 (2002). URL `http://link.aps.org/doi/10.1103/PhysRevLett.88.047901`.

[73] Gardiner, C. W. & Zoller, P. *Quantum noise: a handbook of Markovian and non-Markovian quantum stochastic methods with applications to quantum optics* (Springer, 2004), 3rd edn.

[74] Bianchetti, R. *et al.* Dynamics of dispersive single-qubit readout in circuit quantum electrodynamics. *Phys. Rev. A* **80**, 043840 (2009). URL `http://link.aps.org/doi/10.1103/PhysRevA.80.043840`.

[75] Jaehne, K., Hammerer, K. & Wallquist, M. Ground-state cooling of a nanomechanical resonator via a Cooper-pair box qubit. *New Journal of Physics* **10**, 095019 (2008). URL `http://dx.doi.org/10.1088/1367-2630/10/9/095019`.

[76] Rabl, P. Cooling of mechanical motion with a two-level system: The high-temperature regime. *Phys. Rev. B* **82**, 165320 (2010). URL `http://link.aps.org/doi/10.1103/PhysRevB.82.165320`.

[77] Pikovski, I., Vanner, M. R., Aspelmeyer, M., Kim, M. S. & Brukner, C. Probing planck-scale physics with quantum optics. *Nat Phys* **8**, 393–397 (2012). URL `http://dx.doi.org/10.1038/nphys2262`.

[78] Bagci, T. *et al.* Optical detection of radio waves through a nanomechanical transducer. *arXiv:1307.3467* (2013). URL `http://arxiv.org/abs/1307.3467`.

[79] Andrews, R. *et al.* Reversible and efficient conversion between microwave and optical light. *arXiv:1310.5276* (2013). URL `http://arxiv.org/abs/1310.5276`.

[80] Heikkilä, T. T., Massel, F., Tuorila, J., Khan, R. & Sillanpää, M. A. Enhancing optomechanical coupling via the Josephson effect. *ArXiv e-prints* (2013). URL `http://arxiv.org/abs/1311.3802`. `1311.3802`.

[81] Pinard, M., Hadjar, Y. & Heidmann, A. Effective mass in quantum effects of radiation pressure. *The European Physical Journal D - Atomic, Molecular, Optical and Plasma Physics* **7**, 107–116 (1999). URL `http://dx.doi.org/10.1007/s100530050354`.

[82] Cleland, A. N. *Foundations of nanomechanics: from solid-state theory to device applications* (Springer, 2003).

[83] Sillanpää, M. A., Khan, R., Heikkilä, T. T. & Hakonen, P. J. Macroscopic quantum tunneling in nanoelectromechanical systems. *Phys. Rev. B* **84**, 195433 (2011). URL `http://link.aps.org/doi/10.1103/PhysRevB.84.195433`.

[84] Walls, D. F. & Milburn, G. J. *Quantum optics* (Springer, 2008).

[85] Ingold, G.-L. & Nazarov, Y. V. Charge tunneling rates in ultrasmall junctions. *"Single Charge Tunneling", edited by H. Grabert and M. H. Devoret, NATO ASI Series B, Vol. 294, pp. 21-107 (Plenum Press, New York, 1992)* (1992). URL `http://arxiv.org/abs/cond-mat/0508728`. `cond-mat/0508728`.

[86] Wilson, C. M. *et al.* Coherence times of dressed states of a superconducting qubit under extreme driving. *Phys. Rev. Lett.* **98**, 257003 (2007). URL `http://link.aps.org/doi/10.1103/PhysRevLett.98.257003`.

[87] Wilson, C. M. *et al.* Dressed relaxation and dephasing in a strongly driven two-level system. *Phys. Rev. B* **81**, 024520 (2010). URL `http://link.aps.org/doi/10.1103/PhysRevB.81.024520`.

[88] Autler, S. H. & Townes, C. H. Stark effect in rapidly varying fields. *Phys. Rev.* **100**, 703–722 (1955). URL `http://link.aps.org/doi/10.1103/PhysRev.100.703`.

[89] Son, S.-K., Han, S. & Chu, S.-I. Floquet formulation for the investigation of multiphoton quantum interference in a superconducting qubit driven by a strong ac field. *Phys. Rev. A* **79**, 032301 (2009). URL `http://link.aps.org/doi/10.1103/PhysRevA.79.032301`.

[90] Chu, S.-I. & Telnov, D. A. Beyond the Floquet theorem: generalized Floquet formalisms and quasienergy methods for atomic and molecular multiphoton processes in intense laser fields. *Physics Reports* **390**, 1 – 131 (2004). URL `http://www.sciencedirect.com/science/article/pii/S0370157303003946`.

[91] Gao, J. *et al.* Experimental evidence for a surface distribution of two-level systems in superconducting lithographed microwave resonators. *Applied Physics Letters* **92**, 152505 (2008). URL `http://link.aip.org/link/?APL/92/152505/1`.

[92] Barends, R. *et al.* Minimal resonator loss for circuit quantum electrodynamics. *Applied Physics Letters* **97**, 023508 (2010). URL `http://link.aip.org/link/?APL/97/023508/1`.

[93] Geerlings, K. *et al.* Improving the quality factor of microwave compact resonators by optimizing their geometrical parameters. *Applied Physics Letters* **100**, 192601 (2012). URL `http://link.aip.org/link/?APL/100/192601/1`.

[94] Macintyre, D. S., Ignatova, O., Thoms, S. & Thayne, I. G. Resist residues and transistor gate fabrication. *Journal of Vacuum Science & Technology B: Microelectronics and Nanometer Structures* **27**, 2597–2601 (2009). URL `http://link.aip.org/link/?JVB/27/2597/1`.

[95] Maximov, I., Zakharov, A. A., Holmqvist, T., Montelius, L. & Lindau, I. Investigation of polymethylmethacrylate resist residues using photoelectron microscopy. *Journal of Vacuum Science & Technology B: Microelectronics and Nanometer Structures* **20**, 1139–1142 (2002). URL `http://link.aip.org/link/?JVB/20/1139/1`.

[96] Koppinen, P. J., Vaisto, L. M. & Maasilta, I. J. Complete stabilization and improvement of the characteristics of tunnel junctions by thermal annealing. *Applied Physics Letters* **90**, 053503 (2007). URL `http://link.aip.org/link/?APL/90/053503/1`.

[97] Koppinen, P. *Applications of tunnel junctions in low-dimensional nanostructures*. Ph.D. thesis, University of Jyväskylä (2009). URL `http://urn.fi/URN:ISBN:978-951-39-3582-5`.

[98] Väistö, L. *Tunneliliitosten ominaisuuksien parantaminen lämpökäsittelyllä*. Master's thesis, University of Jyväskylä (2006). URL `http://urn.fi/URN:NBN:fi:jyu-2007453`.

[99] Karulkar, P. C. & Tran, N. C. XPS/AES investigation of cross contamination in a plasma etcher. *Journal of Vacuum Science & Technology B: Microelectronics and Nanometer Structures* **3**, 889–892 (1985). URL `http://link.aip.org/link/?JVB/3/889/1`.

[100] Zorin, A. B. The thermocoax cable as the microwave frequency filter for single electron circuits. *Rev. Sci. Instr.* **66**, 4296–4300 (1995). URL `http://dx.doi.org/10.1063/1.1145385`.

Appendix A

Effective mass

In the standard treatment, the motion of a mechanical resonator is reduced to the dynamics of a single parameter. This is achieved by defining a dimensionless mode function $\vec{u}(\vec{r})$ where $\vec{u}$ is the vector displacement of the mechanical object at point $\vec{r}$. The time-dependent displacement of a vibration mode can then be expressed in terms of scalar global amplitude $x(t)$ as $\vec{u}(\vec{r}, t) = x(t)\vec{u}(\vec{r})$.

The ambiguity of effective mass arises from the normalization chosen for the mode function $\vec{u}(\vec{r})$ [81, 31] which determines the normalization of $x(t)$. The effective mass can be rigorously derived by calculating the potential energy of the chosen mode normalization with elastic theory. Equating this potential energy with $m_{\text{eff}}\omega_m^2 x(t)^2/2$ allows determination of the effective mass for the corresponding simple harmonic oscillator.

The Euler-Bernoulli equation for a doubly-clamped beam with no external forces, no initial tension, and no elongation of the beam is given by [82]

$$EI\frac{\partial^4 u(z)}{\partial z^4} = -\rho A\frac{\partial^2 u(z)}{\partial t^2}, \tag{A.1}$$

where E is Young's modulus, I is the bending moment, ρ is the material density, A is the cross-section of the beam, and z is the position along the beam. Above we have assumed that the bending moment is independent of position. The lowest mode solution is given by

$$u_1(z) = -a_1\left[\cos(\beta_1 z) - \cosh(\beta_1 z)\right] + b_1\left[\sin(\beta_1 z) - \sinh(\beta_1 z)\right], \tag{A.2}$$

where $\beta_1 = 4.73004/L$, L is the length of the beam, and $a_1/b_1 = 1.01781$. In Fig. A.1, two different normalizations for $u_1(z)$ are shown. The solid line in red denotes the normalization with which $x(t)$ describes the evolution of the maximum deflection of the beam. The solid black line on the other hand corresponds

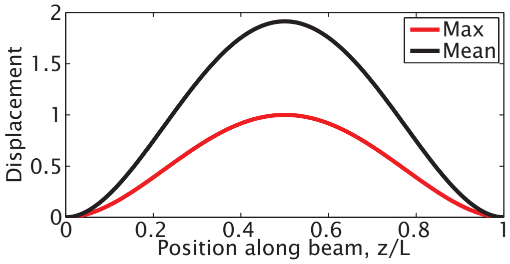

Fig. A.1: The lowest mode function of a doubly-clamped beam resonator normalized to give unit amplitude (denoted with red) and unit displacement of the center-of-mass (black).

to normalization in which $x(t)$ describes the motion of the center-of-mass of the beam.

According to the Euler-Bernoulli theory, the potential energy due to the internal stresses is given by [83]

$$V(t) = \frac{1}{2}EI\left(\frac{\partial^2 u(z)}{\partial z^2}\right)^2 x(t)^2, \tag{A.3}$$

where the global amplitude $x(t)$ is explicitly written down and separated from the normalized $u(z)$. A rectangular beam has a bending moment of $I = tw^3/12$, where t is the evaporated thickness of a beam vibrating in-plane and w is the width of the beam. Numerically evaluating Eq. (A.3) with a rectangular beam and equating the result with $V = m_{\text{eff}}\omega_m^2 x(t)^2/2$ yields $m_{\text{eff}} = 0.396m$ and $m_{\text{eff}} = 1.45m$ for $x(t)$ describing maximum deflection and center-of-mass motion, respectively.

Naturally, the different effective masses yield different zero-point fluctuation amplitudes, $x_{\text{zp}} = \sqrt{\hbar/2m_{\text{eff}}\omega_m}$. In contrast, the optomechanical vacuum coupling g_0 given by Eq. (2.2) does not depend on the chosen normalization since the capacitance derivative also depends on the normalization and cancels out the change in x_{zp}.

In the publications involved in this thesis, $x(t)$ is defined such that it describes the maximum deflection of the beam or membrane. Therefore, the zero-point motion amplitude in the publications does not relate directly to the center-of-mass fluctuations but rather to the fluctuations of the maximum deflection of the mechanical resonator.

Appendix B

Input-output formalism

The treatment given here is based mostly on Chapter 5.3. of Ref. [73]. The treatment is basically also the same as in Chapter 7. of Ref. [84] with a slightly different notation. The latter reference has a number of typos in the chapter we are interested in and therefore I would recommend using the first reference. In this appendix, the notation is a mix of both references.

Roughly speaking, using input-output formalism means explicitly taking into account the environment to which the system of interest is coupled to. Consider first the simplest possible system to which the input-output formalism can be applied. The system is composed of a Fabry-Perot cavity, the infinite reservoir of harmonic oscillators and the coupling between the cavity and the oscillators. The Hamiltonian of the total system is given by

$$\hat{H} = \hat{H}_S + \hat{H}_R + \hat{V}, \tag{B.1}$$

where

$$\begin{aligned} \hat{H}_S =& \hbar\Omega\hat{a}^\dagger\hat{a}, && \text{(B.2)} \\ \hat{H}_R =& \hbar\int_{-\infty}^{\infty} \mathrm{d}\omega\omega\hat{b}^\dagger(\omega)\hat{b}(\omega), && \text{(B.3)} \\ \hat{V} =& i\hbar\int_{-\infty}^{\infty} \mathrm{d}\omega g(\omega)\left[\hat{b}^\dagger(\omega)\hat{a} - \hat{a}^\dagger\hat{b}(\omega)\right], && \text{(B.4)} \end{aligned}$$

where $g(\omega)$ is the coupling strength as a function of frequency. Note that $\hat{b}(\omega)$ refers here to the harmonic oscillators of the environment and not to the mechanical resonator $\hat{b}$ of the system itself.

In what follows, we will solve the Heisenberg equations of motion for the annihilation operators of the cavity and the reservoir. In the Heisenberg representation, the state vector stays constant and the time-evolution for the operator $\hat{A}$ is given by

$$\frac{d}{dt}\hat{A} = \frac{i}{\hbar}\left[\hat{H},\hat{A}\right] + \frac{\partial \hat{A}}{\partial t}. \tag{B.5}$$

B.1 Equation for the reservoir operator

Thus,

$$\dot{\hat{b}}(t,\omega) = \frac{i}{\hbar}\left[\hat{H},\hat{b}(\omega)\right] + \underbrace{\frac{\partial \hat{b}(\omega)}{\partial t}}_{=0} \tag{B.6}$$

$$= \frac{i}{\hbar}\underbrace{\left[\hat{H}_S,\hat{b}(\omega)\right]}_{=0} + \frac{i}{\hbar}\left[\hat{H}_R,\hat{b}(\omega)\right] + \frac{i}{\hbar}\left[\hat{V},\hat{b}(\omega)\right]. \tag{B.7}$$

I will write out these in full. We get

$$\frac{i}{\hbar}\left[\hat{H}_R,\hat{b}(\omega)\right] = i\int_{-\infty}^{\infty} \mathrm{d}\omega'\omega' \left[\hat{b}^\dagger(\omega')\hat{b}(\omega'),\hat{b}(\omega)\right], \text{where} \tag{B.8}$$

$$\left[\hat{b}^\dagger(\omega')\hat{b}(\omega'),\hat{b}(\omega)\right] = \hat{b}^\dagger(\omega')\underbrace{\left[\hat{b}(\omega'),\hat{b}(\omega)\right]}_{=0} + \underbrace{\left[\hat{b}^\dagger(\omega'),\hat{b}(\omega)\right]}_{=-\delta(\omega-\omega')}\hat{b}(\omega'). \tag{B.9}$$

Therefore,

$$\frac{i}{\hbar}\left[\hat{H}_R,\hat{b}(\omega)\right] = -i\omega\hat{b}(\omega). \tag{B.10}$$

The third term in Eq. (B.7) is given by

$$\frac{i}{\hbar}\left[\hat{V},\hat{b}(\omega)\right] = -\int_{-\infty}^{\infty} \mathrm{d}\omega' \{g(\omega')\underbrace{\left[\hat{b}^\dagger(\omega'),\hat{b}(\omega)\right]}_{=-\delta(\omega-\omega')}\hat{a} - \hat{a}^\dagger \underbrace{\left[\hat{b}(\omega'),\hat{b}(\omega)\right]}_{=0}\} \tag{B.11}$$

$$= g(\omega)\hat{a}. \tag{B.12}$$

By combining these two results, we get the equation for the reservoir oscillators

$$\dot{\hat{b}}(t,\omega) = -i\omega\hat{b}(\omega) + g(\omega)\hat{a}. \tag{B.13}$$

B.2 Equation for the cavity operator

The equation of motion for the cavity annihilation operator in the Heisenberg representation is given by

$$\dot{\hat{a}} = \frac{i}{\hbar}\left[\hat{H}, \hat{a}\right] + \underbrace{\frac{\partial \hat{a}}{\partial t}}_{=0} \tag{B.14}$$

$$= \frac{i}{\hbar}\left[\hat{H}_S, \hat{a}\right] + \frac{i}{\hbar}\underbrace{\left[\hat{H}_R, \hat{a}\right]}_{=0} + \frac{i}{\hbar}\left[\hat{V}, \hat{a}\right]. \tag{B.15}$$

The third term is given by

$$\frac{i}{\hbar}\left[\hat{V}, \hat{a}\right] = -\int_{-\infty}^{\infty} \mathrm{d}\omega g(\omega)\left\{\hat{b}^\dagger \underbrace{\left[\hat{a}, \hat{a}\right]}_{=0} - \underbrace{\left[\hat{a}^\dagger, \hat{a}\right]}_{=-1} \hat{b}(\omega)\right\}$$

$$= -\int_{-\infty}^{\infty} \mathrm{d}\omega g(\omega)\hat{b}(\omega). \tag{B.16}$$

At this point, we can leave the actual system Hamiltonian unspecified in order to be able to include other objects into the system, such as the mechanical resonator coupled to the cavity. Therefore,

$$\dot{\hat{a}} = \frac{i}{\hbar}\left[\hat{H}_S, \hat{a}\right] - \int_{-\infty}^{\infty} \mathrm{d}\omega g(\omega)\hat{b}(\omega). \tag{B.17}$$

B.3 Solution to the equations

Let us first examine the reservoir operator equation. If the equation was homogenous, that is,

$$\dot{\hat{b}}(t, \omega) = -i\omega\hat{b}(t, \omega), \tag{B.18}$$

it is easy to assure oneself that the general solution is of the form

$$\hat{b}(t, \omega) = Ce^{-i\omega t}\hat{b}(\omega), \tag{B.19}$$

where C is determined by the boundary conditions. Using an initial condition $b_0(\omega) = b(t_0, \omega)$ in which $t_0 < t$, this obviously yields

$$\hat{b}(t, \omega) = e^{-i\omega(t-t_0)}\hat{b}_0(\omega). \tag{B.20}$$

For the solution to the full inhomogeneous equation, we just have to add a solution to this homogenous solution. By differentiating with respect to time, one can assure that

$$\hat{b}(t,\omega) = e^{-i\omega(t-t_0)}\hat{b}_0(\omega) + g(\omega)\int_{t_0}^{t} dt' e^{-i\omega(t-t')}\hat{a}(t') \tag{B.21}$$

solves Eq. (B.13) and gives the correct initial state. Similarly, we could have specified final conditions for the reservoir as $b_1(\omega) = b(t_1,\omega)$ where $t_1 > t$. This gives

$$\hat{b}(t,\omega) = e^{-i\omega(t-t_1)}\hat{b}_1(\omega) - g(\omega)\int_{t}^{t_1} dt' e^{-i\omega(t-t')}\hat{a}(t'). \tag{B.22}$$

Substituting Eq. (B.21) into Eq. (B.17) gives

$$\begin{aligned}\dot{\hat{a}} = \frac{i}{\hbar}\left[\hat{H}_S,\hat{a}\right] - \int_{-\infty}^{\infty} \mathrm{d}\omega g(\omega) e^{-i\omega(t-t_0)}\hat{b}_0(\omega) \\ - \int_{-\infty}^{\infty} \mathrm{d}\omega g(\omega)^2 \int_{t_0}^{t} dt' e^{-i\omega(t-t')}\hat{a}(t').\end{aligned} \tag{B.23}$$

Following now the arguments of [84] , we make the first approximation towards Markovian evolution and claim the coupling strength $g(\omega)$ to be independent of frequency. We can now write

$$g(\omega)^2 = \frac{\kappa}{2\pi}. \tag{B.24}$$

Thus,

$$\begin{aligned}\dot{\hat{a}} = \frac{i}{\hbar}\left[\hat{H}_S,\hat{a}\right] & -\sqrt{\frac{\kappa}{2\pi}}\int_{-\infty}^{\infty} \mathrm{d}\omega e^{-i\omega(t-t_0)}\hat{b}_0(\omega) \\ & -\frac{\kappa}{2\pi}\int_{t_0}^{t} dt \int_{-\infty}^{\infty} \mathrm{d}\omega e^{-i\omega(t-t')}\hat{a}(t')\end{aligned} \tag{B.25}$$

$$= \frac{i}{\hbar}\left[\hat{H}_S,\hat{a}\right] -\sqrt{\kappa}\underbrace{\frac{1}{\sqrt{2\pi}}\int_{-\infty}^{\infty} \mathrm{d}\omega e^{-i\omega(t-t_0)}\hat{b}_0(\omega)}_{=\hat{a}_{\mathrm{in}}(t)} -\frac{\kappa}{2}\hat{a}(t), \tag{B.26}$$

where we have used the identities

$$\frac{1}{2\pi}\int_{-\infty}^{\infty} \mathrm{d}\omega e^{-i\omega(t-t')} = \delta(t-t'), \tag{B.27}$$

$$\int_{t_0}^{t} dt' \delta(t-t')\hat{a}(t') = \frac{1}{2}\hat{a}(t), \tag{B.28}$$

and defined the input field operator by

$$\hat{a}_{\text{in}}(t) = \frac{1}{\sqrt{2\pi}} \int_{-\infty}^{\infty} \mathrm{d}\omega e^{-i\omega(t-t_0)} \hat{b}_0(\omega). \tag{B.29}$$

Writing in terms of the input operator, we get the quantum Langevin equation for the cavity operator

$$\dot{\hat{a}} = \frac{i}{\hbar} \left[\hat{H}_S, \hat{a}\right] - \frac{\kappa}{2} \hat{a}(t) - \sqrt{\kappa} \hat{a}_{\text{in}}. \tag{B.30}$$

We can also define the output field operator as

$$\hat{a}_{\text{out}}(t) = \frac{1}{\sqrt{2\pi}} \int_{-\infty}^{\infty} \mathrm{d}\omega e^{-i\omega(t-t_1)} \hat{b}_1(\omega), \tag{B.31}$$

in terms of which the quantum Langevin equation is given by

$$\dot{\hat{a}} = \frac{i}{\hbar} \left[\hat{H}_S, \hat{a}\right] + \frac{\kappa}{2} \hat{a}(t) - \sqrt{\kappa} \hat{a}_{\text{out}}. \tag{B.32}$$

Looking at Eqs. (B.30) and (B.32), we see that the input and output fields are related by

$$\hat{a}_{\text{out}} - \hat{a}_{\text{in}} = \sqrt{\kappa} \hat{a}(t). \tag{B.33}$$

Note that the way of defining the input (Eq. (B.29)) and output fields (Eq. (B.31)) affects the signs in the final quantum Langevin equations. In the literature, the convention to define these field operators varies.

Appendix C

Charging energy

C.1 Canonical treatment

In this section, we will derive the charging energy [41] for the simplest possible model of a qubit island coupled to a mechanical resonator. This allows us to explicitly point out the approximations made on the way and consider their validity.

Consider the circuit depicted in Fig. C.1. To derive the Hamiltonian, consider first the Lagrangian which consists of the electrostatic energies stored in the two capacitors,

$$\mathcal{L} = \frac{1}{2}C_J V_1^2 + \frac{1}{2}C_g(x)(V_1 - V_g)^2, \tag{C.1}$$

where V_1 is the voltage on the island and the ground is explicitly set to zero voltage. The voltage on the superconducting island is equal to the derivative of the superconducting phase $V_1 = \dot{\theta}_1$, which is equal to the phase difference across the junction. Denoting $C = C_J + C_g(x)$,

$$\mathcal{L} = \frac{1}{2}C\dot{\theta}_1^2 - C_g(x)V_g\dot{\theta}_1 + \frac{1}{2}C_g(x)V_g^2. \tag{C.2}$$

Fig. C.1: Circuit diagram of the simplified system.

The last term looks like a constant term but let us keep it for a while.

We can now calculate the canonical conjugate for the phase on the island

$$p_{\theta_1} = \frac{d\mathcal{L}}{d\dot{\theta}_1} = C\dot{\theta}_1 - C_g(x)V_g. \tag{C.3}$$

Expressing the Lagrangian in terms of the phase on the island and its conjugate variable gives

$$\mathcal{L} = \frac{1}{2C}(C_g(x)V_g + p_{\theta_1})^2 - \frac{C_g(x)}{C}V_g(C_g(x)V_g + p_{\theta_1}) + \frac{1}{2}C_g(x)V_g^2. \tag{C.4}$$

Assuming that an ideal voltage source is directly connected to the mechanics, the terms independent of island variables can be dropped out since they only shift the zero energy level. This leaves

$$\mathcal{L} = \frac{1}{2C}(C_g(x)V_g + p_{\theta_1})^2 - \frac{C_g(x)}{C}V_g(C_g(x)V_g + p_{\theta_1}). \tag{C.5}$$

The charge q on the island is given by $q = C_J V_1 + C_g(x)(V_1 - V_g) = C\dot{\theta}_1 - C_g(x)V_g$ which we find equal to the conjugate variable of island phase p_{θ_1} given in Eq. (C.3). The total charge on the island is quantized to units of Cooper pairs and we can write it as $q = -2ne$ where n denotes the number of Cooper pairs. Furthermore, normalizing the induced charge on the gate electrode to the units of Cooper pairs and writing $n_g = C_g(x)V_g/2e$ we get

$$\mathcal{L} = 4E_C(n_g - n)^2 - 8E_C n_g(n_g - n), \tag{C.6}$$

where we have introduced the single electron charging energy $E_C = e^2/2C$.

To obtain the appropriate Hamiltonian, we have to reduce the work that is automatically done by the ideal voltage source. The voltage source can be considered to be a huge capacitor C_s holding charge q_s so that the output voltage is $V_g = q_s/C_s$. If a small amount of charge $dq_s \ll q_s$ flows out of the capacitor, the change in the electrostatic energy is given by

$$dE = \frac{q^2}{2C_s} - \frac{(q + dq)^2}{2C_s} \approx -dq\frac{q_s}{C_s} = -dqV_g. \tag{C.7}$$

The charge on the gate satisfies $dq = C_g(V_g - V_1)$ indicating that the work done by the voltage source is given by

$$W = \int dE = -V_g \int dq = -C_g V_g \int d(V_g - V_1) = -C_g V_g (V_g - V_1) \tag{C.8}$$

$$\simeq C_g V_g \dot{\theta}_1 = 8E_C n_g(n_g - n), \tag{C.9}$$

where we have again dropped terms that are independent of island variables in the last row. Finally, the charging energy Hamiltonian is given by

$$H = \mathcal{L} - W = 4E_C(n_g - n)^2. \qquad \text{(C.10)}$$

C.2 Effect of the environment

The treatment for the charging energy given in the last section relies on a very strong assumption. Namely, that the ideal voltage source is directly connected to the mechanical gate and it does work instantaneously as the gate charge is changed due to mechanical motion, see Eq. (C.9). In practice, however, the voltage source is connected to the gate through heavy filtering that cuts off frequencies around the mechanical resonant frequency. Therefore, the voltage source can not provide the energy at the mechanical frequency which eventually enhances the coupling between the mechanics and the system that is capacitively coupled to its motion. Furthermore, since the work done by the voltage source is directly proportional to the position of the mechanical motion, the ideal voltage source would constantly measure the mechanics, which surely is unwanted in most quantum information processing schemes involving mechanics.

First, it is good to note what happens if the voltage source does not do any work. Equation (C.6) implies that if no work is done by the source,

$$H = \mathcal{L} = 4E_C(n_g - n)^2 - 8E_C n_g(n_g - n) = 4E_C\left(n^2 - n_g^2\right). \qquad \text{(C.11)}$$

We thus see that the qubit Cooper pair states would no longer be coupled to the gate charge and thus uncoupled from the mechanical motion.

It therefore appears that we need to include into consideration the electrical environment of the mechanics. Similar considerations were carried out in the 1990's when physicists were deriving the requirements for the electrical environment for the Coulomb blockade to be observable [85].

In a typical system, the gate capacitance is very small, of the order of femtofarads, and it is completely dominated by the parasitic capacitances in the gate line on the chip which are orders of magnitude larger. These parasitic capacitances will be polarized by the gate voltage applied by the voltage source regardless of the heavy filtering between them. The change of charge on the mechanical gate is very small in comparison to the charge stored in these parasitic capacitors and they will act as an effective voltage source for the mechanical gate.

We would thus need to model the environment with an impedance given by this electrical environment. The analysis is not done here but it should provide bounds on the losses that the electrical environment can have in order for the voltage enhanced coupling scheme to work. The environmental impedance might also be important from the point of view of qubit losses since the qubit island is very strongly coupled to it by the static capacitance provided by the mechanical resonator. One might anticipate that the environment should be as reactive as possible to prevent lossy modes from coupling to the qubit.

Appendix D

Floquet representation

The Floquet picture provides a semiclassical treatment of a quantum system coupled to a driving field in which the field is considered classical. It is especially useful with strong driving fields [86, 87] since it is a nonperturbative method. The Floquet theorem was first used for monochromatic fields by Autler-Townes [88] and formalism was elaborated to the form presented here by Shirley [68]. Since then, the formalism has been generalized beyond the conventional treatment to cover various specific problems.

In this appendix, we will review the Floquet theory based mostly on [70, 89, 90].

D.1 Floquet picture

Consider a time-independent quantum system that is described by a Hamiltonian $\hat{H}_0$ and is driven by a monochromatic classical field $\hat{V}(t)$ such that $\hat{V}(t + 2\pi/\omega) = \hat{V}(t)$. The total Hamiltonian is given by $\hat{H} = \hat{H}_0 + \hat{V}(t)$ and the Schrödinger equation can be written as

$$\left(\hat{H} - i\hbar\partial/\partial t\right)\Psi(t) = 0. \tag{D.1}$$

Similar to Bloch states, the field-dressed states can be written according to the Floquet theorem [68] as

$$\Psi(t) = e^{-i\epsilon t/\hbar}\Phi(t), \tag{D.2}$$

where ϵ is the quasienergy of the state and $\Phi(t)$ is a periodic function with the same periodicity as the driving field $\Phi(t + 2\pi/\omega) = \Phi(t)$. Substituting the form of the solution, as given in Eq. (D.2), into the Schrödinger equation Eq. (D.1), one obtains a Schrödinger-like equation for $\Phi(t)$

$$\left(\hat{H}(t) - \epsilon\right)\Phi(t) = -i\hbar\frac{\partial\Phi(t)}{\partial t}. \tag{D.3}$$

Since now both the Hamiltonian and quasienergy state $\Phi(t)$ are periodic with the same periodicity $\tau = 2\pi/\omega$, we can expand them using their Fourier components as

$$\Phi(t) = \sum_{\alpha} \sum_{m=-\infty}^{\infty} c_{\alpha}^{m} e^{im\omega t} |\alpha\rangle, \tag{D.4}$$

$$H(t) = \sum_{\alpha,\beta} \sum_{n=-\infty}^{\infty} h_{\alpha\beta}^{n} e^{in\omega t} |\alpha\rangle\langle\beta|, \tag{D.5}$$

where $|\alpha\rangle$ (and $|\beta\rangle$) denotes a vector of a complete orthonormal set spanning the original Hilbert space of the problem. Substituting these back into Eq. (D.3), one gets

$$\sum_{n,m} \sum_{\alpha,\beta} h_{\alpha\beta}^{n} e^{i(n+m)\omega t} c_{\beta}^{m} |\alpha\rangle - \epsilon \sum_{m,\alpha} c_{\alpha}^{m} e^{im\omega t} |\alpha\rangle = -\hbar\omega \sum_{m,\alpha} c_{\alpha}^{m} e^{im\omega t} |\alpha\rangle, \tag{D.6}$$

which yields the equation for each component c_{α}^{k},

$$\sum_{m} \sum_{\beta} h_{\alpha\beta}^{k-m} c_{\beta}^{m} + k\hbar\omega c_{\alpha}^{k} = \epsilon c_{\alpha}^{k}. \tag{D.7}$$

We can express this in a matrix form as

$$H_F c = \epsilon c, \tag{D.8}$$

where c is a column vector composed of the coefficients c_{α}^{k} and matrix H_F components are given by

$$\langle \alpha n | H_F | \beta m \rangle = h_{\alpha\beta}^{n-m} + m\hbar\omega \delta_{n,m} \delta_{\alpha,\beta}. \tag{D.9}$$

We have thus transformed the time-dependent problem of Eq. (D.1) into the time-independent eigenvalue problem of Eq. (D.8). We have, however, expanded the dimensionality of the problem to infinity. Even if the original Hilbert space is described using a finite set $\{|\alpha\rangle\}$, the index k in Eq. (D.7) runs from $-\infty$ to ∞. Nevertheless, this infinite dimensional problem can be approximated with a truncated Hamiltonian which size depends on the strength of the classical drive.

As a final note, we observe from Eq. (D.2) that if ϵ and $\Phi(t)$ solve the equation, also $\epsilon + m\omega$ and $\exp(im\omega t)\Phi(t)$ are solutions with an arbitrary integer m, since

$$\Psi'(t) = e^{-i\epsilon' t/\hbar} \Phi'(t) = e^{-i(\epsilon+m\omega)t/\hbar} e^{im\omega t} \Phi(t) = e^{-i\epsilon t/\hbar} \Phi(t) = \Psi(t). \tag{D.10}$$

Therefore these solutions are physically identical. Their physical interpretation can, however, be different in the sense that m can be interpreted as the number of quanta given to the system by the driving field. Here, this is truly an interpretation since the driving field was taken to be classical from the outset.

Appendix E

Longitudinal qubit drive

To drive mechanical qubit sidebands in the transmon regime, one needs to apply longitudinal driving to the qubit. Furthermore, to prevent undesired direct excitation of the qubit, the transversal component of driving needs to be kept sufficiently small. In this appendix, we consider qubit drive via the gate and the flux line and transform the drives into the unperturbed qubit eigenbasis. The goal is to find out how pure longitudinal driving can be attained with these two control lines.

E.1 Diagonalized drives

Driving the qubit via the gate, the drive is proportional to $\hat{n} - n_g$. Therefore, the gate drive is similarly to mechanics coupling transversal in the transmon regime and can not be used to drive the qubit longitudinally. Flux drive is thus necessary.

The total drive written in the Cooper pair basis is given by

$$\begin{aligned} H_{\text{Drive}} =& 8E_C(\hat{n} - n_g)\Delta n_g \cos(\omega t) \\ &+ \frac{E_{J1} + E_{J2}}{2}\pi\frac{\Phi_{\text{ac}}}{\Phi_0}\sin\left(\pi\frac{\Phi_{\text{dc}}}{\Phi_0}\right)\Big(|n+1\rangle\langle n| + |n\rangle\langle n+1|\Big)\cos(\omega t + \phi) \\ &- \frac{E_{J1} - E_{J2}}{2}\pi\frac{\Phi_{\text{ac}}}{\Phi_0}\cos\left(\pi\frac{\Phi_{\text{dc}}}{\Phi_0}\right)i\Big(|n+1\rangle\langle n| - |n\rangle\langle n+1|\Big)\cos(\omega t + \phi), \end{aligned} \tag{E.1}$$

where the first term is due to the gate drive, the second is due to the symmetric part of Josephson energy, and the last term due to the asymmetric part. Both control tones have the same frequency but their relative phase offset is denoted by ϕ. The form of flux drive implies that the qubit drive caused by to the symmetric part of Josephson energy vanishes at $\Phi_{\text{dc}} = 0$, which corresponds to the

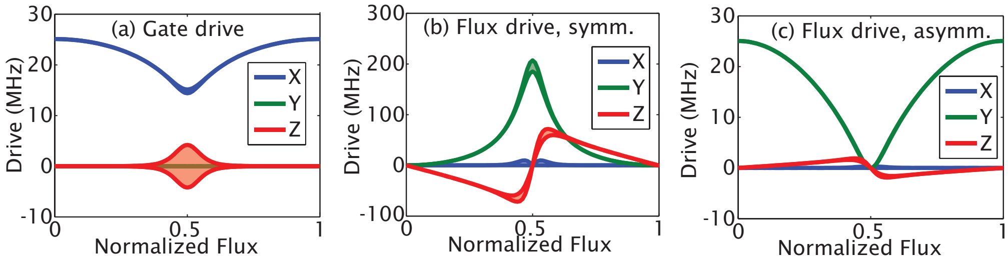

Fig. E.1: Qubit drives diagonalized to the qubit eigenbasis. (a) Gate drive, (b) drive due to symmetric Josephson energy, and (c) drive due to the asymmetric part of Josephson energy. The drive amplitude is 1 % of gate charge or flux period. Lines denote the minimum and maximum values and the shaded area the gate charge dependency. The qubit parameters are identical to the fourth Publication of this thesis.

flux point of maximum Josephson energy. In contrast, at this flux point, the drive related to asymmetric Josephson energy is maximized. Since the Josephson energy only has a symmetric component at $\Phi_{\mathrm{dc}} = 0$, the drive at this flux sweet spot has a vanishing longitudinal component.

To confirm the logic and to get a full picture, drives are numerically diagonalized to the qubit eigenbasis. The diagonalized drives are presented in Fig. E.1 with the parameters from Publication **IV** and drives that correspond to 1 % of the gate or flux period.

Clearly, to remain in the transmon regime while applying longitudinal driving, normalized flux close to but not exactly equal to zero should be used. The flux drive will inevitably have a non-vanishing transversal component which can be mostly compensated for with a suitably chosen gate drive.

E.2 Cancelling the transversal drive component

By denoting the gate drive with A and the flux drive with B, the total qubit drive can be written as

$$\begin{aligned}\hat{H}_{\mathrm{Drive}} = & A_x^{01}\left(\hat{\sigma}_+^{01}e^{i\omega t} + \hat{\sigma}_-^{01}e^{-i\omega t}\right) + A_z^{01}\hat{\sigma}_z^{01}\cos(\omega t) + B_z^{01}\hat{\sigma}_z^{01}\cos(\omega t+\phi) \\ & + B_x^{01}\left(\hat{\sigma}_+^{01}e^{i(\omega t+\phi)} + \hat{\sigma}_-^{01}e^{-i(\omega t+\phi)}\right) + B_y^{01}\left(-i\hat{\sigma}_+^{01}e^{i(\omega t+\phi)} + i\hat{\sigma}_-^{01}e^{-(i\omega t+\phi)}\right),\end{aligned} \tag{E.2}$$

where ϕ is the phase shift between the drives with identical frequency. At the gate charge sweet spots ($n_g = 0$ and $n_g = 0.5$), numerical diagonalization confirms that B_x^{01} vanishes. Therefore, to cancel the transversal driving at $n_g = 0.5$,

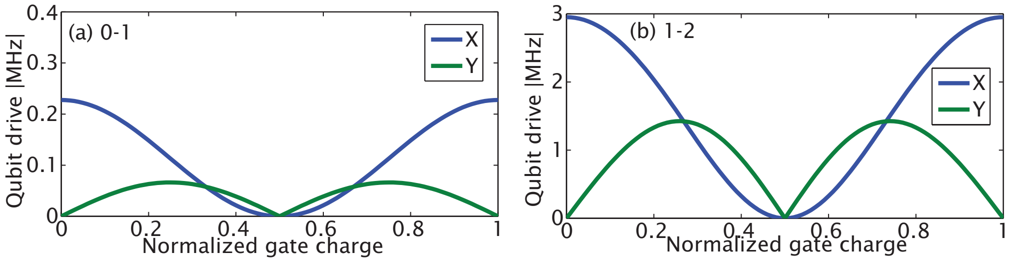

Fig. E.2: Uncancelled transversal qubit drives in (a) 0-1 and (b) 1-2 transition. The flux drive is chosen such that the amplitude corresponds to flux modulation of 1/100 of the flux period. Gate drive is chosen to cancel the transversal component at $n_g = 0.5$.

we choose $\phi = -\pi/2$. This yields

$$\begin{aligned}\hat{H}_{\text{Drive}} &= \left(A_x^{01} - B_y^{01}\right)\left(\hat{\sigma}_+^{01} e^{i\omega t} + \hat{\sigma}_-^{01} e^{-i\omega t}\right) + B_x^{01}\left(-i\hat{\sigma}_+^{01} e^{i(\omega t+\phi)} + i\hat{\sigma}_-^{01} e^{-i(\omega t+\phi)}\right)\\ &\quad + \sqrt{\left(A_z^{01}\right)^2 + \left(B_z^{01}\right)^2}\,\hat{\sigma}_z^{01}\sin(\omega t+\varphi) \qquad \text{(E.3)}\\ &\widehat{=} \left(A_x^{01} - B_y^{01}\right)\hat{\sigma}_x\cos(\omega t) + B_x^{01}\hat{\sigma}_y\cos(\omega t)\\ &\quad + \sqrt{\left(A_z^{01}\right)^2 + \left(B_z^{01}\right)^2}\,\hat{\sigma}_z^{01}\sin(\omega t+\varphi),\end{aligned}$$

where $\varphi = \arcsin(A_z^{01}/\sqrt{(A_z^{01})^2 + (B_z^{01})^2})$. At $n_g = 0.5$, the $\hat{\sigma}_x$-driving becomes zero, $B_x^{01} = 0$, and the driving can be made longitudinal simply by choosing $A_x^{01} = B_y^{01}$.

Away from the transmon-regime limit, the drive directions depend on the gate charge and they can not be cancelled by a single choice of relative phase and amplitude. The uncancelled transversal qubit drives are shown in Fig. E.2(a) at flux $\Phi/\Phi_0 = 0.32$ as a function of gate charge. The flux drive is set to 1 % of the flux period and the gate drive amplitude is chosen to cancel the $\hat{\sigma}_x$ drive at $n_g = 0.5$. This gives a gate drive amplitude that is 0.75 % of the gate period and yields at the sweet spot an $\hat{\sigma}_z$ drive just below 15 MHz. In a case where the gate charge is uncontrolled, the transversal drive is thus at most 2 % of the longitudinal drive. In figure E.2(b), the uncancelled part is presented for the case in which the 1-2 transition is operated as the qubit.

When only two levels are considered, the transversal driving can be cancelled sufficiently well. With a higher E_J/E_C ratio, the driving directions become practically independent of gate charge. Towards the charge-qubit regime the scheme becomes more difficult and gate charge control is practically required because the transversal driving easily becomes very large as the gate deviates from the charge sweet spot.

Appendix F

Qubit-mechanics fabrication

F.1 Marker wafer dicing

To start with, spin the resists before dicing. The biggest problem with regard to dirty chips is the dust from the substrate itself that attaches itself very strongly to the chip surfaces. The resist on top of the wafer protects the surface from the dust that is inevitably present in dicing; dust is especially likely to be present with sapphire chips. Attach blue tape on top of the wafer for the protection of both the resist and the silicon surface and bake it for approximately 10 mins @ 50 C° oven.

After dicing, remove the tape on top of the chips one-by-one with tweezers and rinse each of them swiftly with isopropanol (IPA). The chips are ready for SEM (scanning electron microscope) patterning. One should check the chips with an optical microscope to confirm that there are no extra particles on the chip. If there is a large dust particle or particles, the chip can be rotated so that the dust particle will appear in a place where it does not prevent the device from functioning. If substrate powder on a chip makes it unsuitable for patterning, it is best to clean the chip with acetone and repeat the resist spinning.

Note: dicing sapphire substrate is a bit trickier since the resist is easily washed away by water during the process. If this happens, sapphire chips are full of extremely fine sapphire powder which is very difficult to get rid of and thus can be detrimental for fabrication. One could try hard-baking the resist to make it more resistant (30 min bake of the resist layer). The wafers have also been covered with an optical resist which seems to be more water-proof than the PMMA or copolymer resists.

F.2 Spinning the resist layers

If the process is started with diced, resist-coated chips, one can continue to SEM patterning. It should be made sure however that the resist coating has been done relatively recently, maybe at maximum of 3-6 months ago. The resists will age in a way that they stick too tightly on to the substrate. The aging of a resist can be observed as dimmer spots in the SEM patterning as well as through difficulties in the lift-off after aluminum evaporation.

Before the spin-coating, the chips should be cleaned.

1. 10 minutes in acetone on a 95°C hot plate. A water bath can be used to hold the acetone beaker in order to prevent overheating.
2. 10 minutes at 30 % ultrasound in either acetone or IPA. If chips without markers are used, full power in ultrasound can be used. The 100 % ultrasound can occasionally damage the small markers so this is not recommended for chips with markers.
3. After ultrasound, the chips should be rinsed in IPA and dried with nitrogen so that no stains from solvent evaporation are left on the chips.

These steps only take away the material that is soluble in acetone or IPA. The biggest problem that is faced with cleaning is the removal of substrate particles or substrate dust on the chips. One way to get rid of them is physically scrubbing them off. To do this, dip a cotton tip in acetone and with relatively strong pressure, sweep the surface of the chip clean. This can be quite demanding because the silicon chips are brittle and too hard grip with tweezers will break off even more particles from the chip edges. After sweeping for a while, the results should be checked with an optical microscope and the process should be continued until the chip looks clean. Overall this is very laborious work and should be avoided by protecting the chips carefully during dicing and handling the chips that are ready with tweezers so gently that no extra dust is being created. Another option for cleaning is to spin the chip at 6000 rpm and rinse the chip using an IPA or acetone wash bottle, see Fig. F.1.

When spinning, one should always remember not to put or dip plastic syringes into the containers where the resists are stored. They might contaminate all of the resist in the bottle. One should use glass syringes and fill them with one dip to minimize external contact with resists. The other option is to use extra small beakers into which the resists are first poured and then use any kind of syringe. The resist should not be returned to its container after it has been in any syringe.

Fig. F.1: Cleaning a silicon chip in a spinner. On the left, a silicon chip edge prior to cleaning. On the right, a chip after spinning at 6000 rpm and rinsing with IPA. Most of the silicon particles have been removed.

This also implies that one syringe is used for only one resist so that the resists are not being mixed through the remains that are left in syringes.

The resist recipe I have been using is

1. Copolymer EL10, 60 s at 4000 rpm and 90 s bake at 155°C (the small hot plate shows higher temperatures so this corresponds to 150°C).

2. PMMA A3, 60 s at 4000 rpm and 90 s bake at 185°C.

If nonconducting substrates are used (e.g., sapphire), the final layer is espacer, and the recipe is 60 s at 4000 rpm and 90 s bake at 100°C. The espacer should be kept in the fridge and only taken out to fill the syringe. There seems to be no need to heat it up to room temperature in the syringe in order for it to work. When using espacer, remember to use the lid when spinning and change the cleanroom wipes thet protect the spinner from spills after you are done.

In the above recipe, I baked the resists only for 90 s. The resist can be made stickier by baking for a longer time (15 to 30 mins) so that more solvent is allowed to evaporate. This can be useful for some applications (for example the dicing protective covers) but it also makes the lift-off more challenging.

F.3 Bottom layer fabrication

F.3.1 SEM pattern for the bottom layer

Not many practical tips can be given here because electron microscopes are different. However, the alignment with the markers should be done exactly the same way every time in order to get the same alignment for all the different layers. An important fact is that there is a small offset (on the order of micrometers) when using different patterning currents and different magnifications. Furthermore, it is possible that these offsets change overtime and can not be removed completely by measuring them and compensating in the run file. Therefore, when aligning something very precisely, I would recommend using the same magnification and current for both layers. This way one can easily attain alignment offsets on the order of 100-200nm.

F.3.2 Development of the bottom layer

When choosing the electron doses and development times, one can choose either to maximize the contrast between the PMMA and copolymer layer development or to maximize the reproducibility. The former means using higher doses and development times of 3 to 5 seconds. I have been using the latter one where the doses are smaller but the development time is roughly 30 seconds. Smaller development times have been observed to develop the underlying copolymer layer more relative to the PMMA on top which allows larger undercuts to be fabricated. The problem there is that the short development time is not very reproducible.

For the doses in my pattern (area dose 300-400 μC/cm^2), I have been using the development recipe

1. 28-30 s at 1:3 MIBK:IPA
2. Rinse with IPA to stop the development
3. Blow dry with nitrogen
4. Check with an optical microscope

F.3.3 Evaporation for the bottom layer in Micronova

Evaporation, and especially the oxidation, should be done in a chamber in which the conditions remain the same over time. It seems that even small amounts of impurities in the vacuum chamber affect the oxidation rate and ultimately the obtained junction resistance.

The surface losses in superconducting devices have been shown to be the dominant loss mechanism in superconducting resonators [91, 92, 93]. It is also shown that a thin resist film remains on the substrate even on the exposed areas of 2 to 3 nm in thickness with granules up to 20 nm thick [94, 95]. Therefore it seems that cleaning the substrate, depositing the metal, and patterning the structure is the desirable fabrication method. Using the shadow evaporation technique however requires depositing the resist on top of the substrate. For applications requiring low losses of the cavity, the qubit and the cavity are thus best fabricated in two different steps. If they are fabricated simultaneously in one step, one should use oxygen ashing to remove the remaining resist film from the exposed areas even though it widens the Josephson junction arms. It has been shown that cleaning the substrate surface prior to shadow evaporation with oxygen plasma in a RIE (using Oxford Plasmalab 80 Plus with a typical power of 30 W, a pressure of 40 mTorr, and a duration of 30 seconds) slows the aging effect of junctions, that is, junction resistance becomes more stable as a function of time [96, 97, 98].

I have been doing a short cleaning of the substrate surfaces after the development by using the Reactive Ion Etcher (RIE) in Micronova with the recipe,

1. 15 s at 45:5 O2:Argon (Pressure 250 mTorr, rf power 50 W)

This should remove resist remains and thereby increase the adhesion of the evaporated metal as well as reduce two-level fluctuators at substrate-metal interface.

For evaporation, I have been using the Micronova evaporator

2. Pump down to roughly 3e-7 mbar for 15 mins. It is beneficial to evacuate the chamber to roughly the same pressure since this will affect the resistances obtained
3. Evaporate 20 nm of aluminum from +25 degrees. Evaporation rate around 1-2 Å/s.
4. Oxidize 50 s at 0.14 mbar oxygen.
5. Evaporate 40 nm of aluminum from -25 degrees. Evaporation rate around 2-4 Å/s.

To minimize the junction size (to get a 50 nm overlap), I have been using +/-18-20 degrees. Even if the nominal dimension of the junctions are the same, the resulting undercut depends on the areas exposed around the junctions and these might not be directly applicable to different designs.

The nominal dimensions of the Josephson junctions have been two rectangles in L shape of widths 60 nm and 100 nm and area doses of 1000 μC/cm^2 and 1200 μC/cm^2, respectively. The distance between them has been 275 nm. The first angle is chosen such that the metal is evaporated along the 60 nm thick rectangle towards the thicker rectangle. The second evaporation layer is then along and towards the 60 nm thick rectangle.

After the evaporation is done, the lift-off is best done immediately. I have done this one chip at a time,

6. Keep the chip for 3 mins in an almost boiling 95°C acetone beaker immersed in a water bath.
7. Take the acetone beaker off the hot plate and firmly grip the chip with tweezers while keeping the chip in the acetone all the time.
8. Take a plastic syringe and squirt the chip with the hot acetone by keeping the chip in place against the bottom of the beaker with the tweezers. After some 10 to 15 squirts, the aluminum should be washed away except for the places where the resists were developed away. One should continue rinsing with acetone as long as necessary since the lift-off becomes exponentially more difficult if the chip is lifted off the acetone as it will dry immediately.
9. After the extra metal has been rinsed away, lift the chip of the acetone and rinse with IPA
10. Dry with nitrogen and examine under the optical microscope.

If the aluminum seems to be sticking to the substrate surface at step 8, one can try to boil the next chip longer (5 to 10 mins). It is also possible to use ultrasound but that should be the very last option because it often damages the sample by breaking off the smallest parts. Ultrasound usually has to be used if the chip is taken away from the acetone and the optical microscope reveals parts that have not lifted off and would prevent the sample from functioning. With ultrasound it is best to start with low power and short pulses (15 to 30 seconds) and frequently check the chip with an optical microscope.

There are plenty of reasons for a difficult lift-off. The most common ones are an old resist, baking the resist for too long time, too long of a time between evaporation and lift-off, a rough substrate surface to which the resist adheres strongly, and taking the chip out of the acetone too early. It can also be that there is poor adhesion between the metal and the substrate that results in metal which should be left on the chip being ripped away. The adhesion can be improved by treating the chip with a RIE as explained above. The most difficult form of lift-off problem is the one caused by inadequate chip design. Usually the smaller the areas that need lift-off, the more difficult it is. Therefore, one should design the pattern such that the smallest areas are connected to larger ones somehow. Avoiding tight kinks in the pattern can also help allow smooth lifting off of large flakes.

F.3.4 Measuring the Josephson junction resistance

Before moving on to the following fabrication layers, I strongly recommend measuring the test Josephson junctions in the device. It is good to do this every time because even if the process is nominally the same, the resistances rarely seem to be the same. Even among chips of the same batch, there can be $\pm 10\%$ deviations. Even the high resistivity silicon conducts at room temperature so the conducting substrate samples have to be cooled down. At the very least, the samples have to be dipped into liquid nitrogen but some silicon substrates must be cooled all the way to liquid helium temperatures. The room temperature conductivity of silicon gives a contribution of 20 kΩ to infinity so it can completely misguide the measurement of Josephson junction resistances.

1. Bond 2 to 3 wires to the line and 2 to 3 wires to the ground (keep a 50 Ω short in the sample holder SMA connector)
2. Measure if the bonds are conducting (resistance should be a few Ohms), keep the voltmeter grounded to the same potential as the bonder.
3. Ground yourself and scratch off the short between the pads. When scratching the shorts, make sure that the line which is connected to the on-chip short is itself shorted with 50 Ω.
4. Measure to see if the short was scratched off successfully. At this point, one can already prepare the (Fluke III) multimeter for measurement. One should keep a resistor in parallel which is of the same order as the expected Josephson junction resistance (10 to 50 kΩ). On some rare occasions, the current from the resistance measurement breaks the Josephson junction so that it becomes fully conducting (100 Ω). To prevent this, one can use the manual button to move into a range in which the resistance is seen with reasonable accuracy but the current through the junction is lower. The bars

on the screen indicate the voltage difference between the multimeter lines and therefore the current.

5. Fill up a dewar with nitrogen. Ground the nitrogen dewar, the multimeter, and yourself to the same ground. Dip the sample box holding the Josephson junctions into the liquid nitrogen using a BNC cable which has been assigned for this.

6. Lift the sample up from the liquid nitrogen and dip it into a helium dewar which is also grounded to the same ground.

7. After lifting up the sample, heat up the sample, the sample box, and the cables to room temperature with a heat gun so that water condensing on them does not cause any problems.

8. Remove the bonds with tweezers so that they are not left hanging around to cause problems for the next resist spinning/patterning. Also remove the varnish that was holding the chip in the sample holder by wiping the chip against acetone-wetted tissue. If varnish is left on bottom of the chip, it can cause problems when the next lift-off is done since it will be dissolved by the acetone and can migrate on top of the chip. One will most likely notice that the 77 K and 4 K resistances are very often the same and significant differences rarely occur. For samples on sapphire, one can do the exact same as above (bonding, scratching of shorts, careful grounding and voltage control of the multimeter) but leave out the cooling part.

F.3.5 Bonding

Before attaching the sample on to the sample holder, one should scratch the copper surfaces with a scalpel to remove the copper oxide that has formed. Bonding on copper should be very easy and skipping oxide cleaning is one cause for copper bonding problems. Another potential problem is bonding on uneven surfaces or on surfaces which are floppy. For this reason extra care should be taken with the sample holders which have suspended PCB bonding pads. First of all, the thin bonding pads should be cleaned very gently with a brand new scalpel in which the blade is unbroken when inspected with microscope. Secondly, the PCB bonding pads should be pushed down a little bit so that they are slightly inclined downwards. And finally, after attaching the sample to the holder with varnish, the screws in the bottom of the Sample holder should be tightened such that the surface of the chip pushes the PCB board to an even position and does not allow it to bend when bonding.

After loading the bonding program, it is advisable to adjust the sensor measuring the bonding pressure. Press ’mode’, choose 14 with the arrow keys, and the bonder shows the current value for the offset. One can adjust the offset with a screwdriver from a small hole on the right side of the bonder. Set the offset to 30 and click escape two times. Press ’mode’ again and choose 0 to get back to the bonding mode. If one is bonding for a longer period of time or poor sticking of the bonds starts to be a problem, one should check the offset value again.

For the bond to stick well to the surface, the wire should be running directly through the center of the bond needle. Before making the first bond, one can adjust this by feeding some wire so that it can be seen under the microscope. If the bond wire is rolling out too much, for example, to the left, one can move to the right edge of the chip and push the wire against the chip until the wire is running through the center.

On the second bond this obviously cannot be done and the wire position is a bit more difficult to control. The best way is to anticipate which direction the wire is going to come loose in and direct the bonder slightly towards the other direction before making the first bond. This way the bonder can be moved sideways a little bit so that the wire can be caught again under the bonder needle after the first bond is done. Sometimes the bond wire is easier to be controlled if one first moves half way forward in the loop height and the rest of the way in search height.

F.4 Sacrificial layer fabrication

For the sacrificial layer of the mechanical resonator, overexposed PMMA A3 is used such that it is not removed by acetone. The spin rate with which the PMMA resist is spun on the chips crucially affects the final gap between the mechanical resonator and the electrode patterned in the bottom layer. This being the most decisive parameter of the coupling strength, it is worth spending some time optimizing the spin rate. During PMMA resist burning, the thickness will shrink roughly to one third of the original thickness. For the four micrometers wide and five micrometers long bridge resonators used with transmon qubits, a spin rate of 2500 rpm (2800 rpm is the maximum that I have succeeded with) has been consistently produced bridges which do not collapse on to the electrode. With resonators of the same length but only two micrometers wide, a spin rate of 3200 rpm could be used without the bridge collapsing. This translates only to a few nanometer differences in the final gap, however, the final gaps being 50-65 nm and 45-50 nm, respectively.

1. Spin PMMA A3 for 60 s at 2500 rpm and bake for 5 mins at 185°C.
2. Pattern the sacrificial layer with an area dose of 10 000 μC/cm^2
3. Remove the unexposed resist by keeping the chip in 95°C acetone for ten minutes
4. Check the alignment of the sacrificial layer and the bottom layer with an optical microscope

F.5 Mechanical resonator layer fabrication

For the final layer, extra thick resist has been often used since the evaporated thickness of aluminum will be 300 nm. I have also used a resist of normal thickness without problems but it is better to be overcautious. Thinner mechanical resonators have been fabricated but they seemed to produce resonators whose resonant frequency as a function of gate voltage behaved very irregularly. To confirm this with absolute certainty, one would have to fabricate two mechanical resonators on the same chip but this has not been done.

1. Spin Copolymer EL10 for 60 s at 4000 rpm and bake for 90 s at 155°C.
2. Spin second layer of Copolymer EL10, 60 s at 4000 rpm and bake for 90 s at 155°C.
3. Spin PMMA A3 for 60 s at 4000 rpm and bake for 90 s at 185°C.
4. Pattern the mechanical resonator layer
5. Develop 30 s at 1:3 MIBK:IPA
6. Squirt with IPA to stop the development
7. Blow dry with nitrogen
8. Check the alignment with an optical microscope

F.5.1 Mechanical resonator evaporation

The evaporation is done in a Nanotalo UHV (ultra-high vacuum) evaporator because the larger cups allow more material to be evaporated without having to fill them too often. When evaporating for longer (up to 300 nm), the chamber will heat up and the chamber pressure can start to increase towards the end of the evaporation. The higher pressure in the chamber will result in a smaller grain size of the evaporated material. There is a belief that bigger grain size would result in better mechanical properties, that is, a better Q-value so the chamber pressure is ideally kept low. For this I have cooled down the slab on top of the evaporator chamber by filling it with liquid nitrogen through the siphons on top.

Sometimes the vacuum pressure will increase nonetheless. If the pressure goes over 1e-6 mbar, I stop the evaporation, let the chamber cool down/pump down, and continue after an hour or so.

1. Evaporate 300 nm of aluminum keeping the pressure below 1e-6 mbar. Cool down the chamber by pouring liquid nitrogen into the hollow slab on top of the chamber.
2. Lift-off by keeping the Sample in 95°C acetone for 3 minutes. Rinse with IPA.

F.5.2 Mechanical resonator release

The mechanical resonator is released by burning away the PMMA sacrificial layer in oxygen plasma. The task is challenging since the gap is approximately 50 nm and this narrow gap has to be etched two micrometers from each side. To get an isotropic etch, as large as possible pressures should be used such that the oxygen plasma still ignites. Otherwise the etching can take too much time. In principle the etching could be done in the Micronova RIE which has the luxury of a water cooled stage. However, it has been producing weird, fluffy stuff hanging down from the mechanical resonator and has been unable to etch through. This is possibly due to cross contamination [99] from the other processes done with the etcher (SF6, CF4) and therefore can be from any other substance used (C, F, etc).

In the Nanotalo plasma chamber, there is no cooling mechanism so the etching has to be done in steps to avoid overheating the samples. In cases where the etching time has been too long, the areas with oxide in between two aluminum layers have started to produce large hillocks. This is the case with Josephson junction devices where the whole device is fabricated in one step. One has to also be careful that the chamber actually contains oxygen and that it is not only air leaking in which is being ignited. The plasma produced by air is a lot brighter than the plasma that is produced by pure oxygen.

1. Start the etcher, and especially the vacuum pump, well in advance to allow the pump to reach its maximum efficiency.
2. Make a dummy etch for a few minutes to clean the chamber before putting the actual sample in. Failing to do this can leave oil droplets from the pump in the vacuum chamber possibly contaminating the Sample surface.
3. Etch for 15 minutes at 1000 mTorr oxygen after which let it cool down for 15 minutes. Etch for a total of 60 minutes.

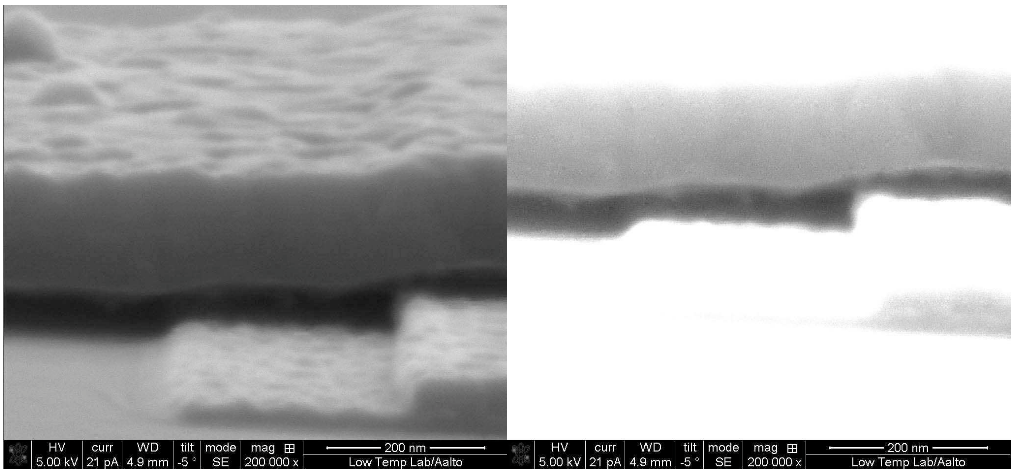

Fig. F.2: Unidentified material in the gap between the mechanical resonator and qubit island. On the left, normal contrast image with low acceleration voltage. On the right, contrast is chosen to maximize the visibility of the material hanging from the mechanical resonator.

F.5.3 Imaging the gap with SEM

For checking the released mechanical resonator and to measure the gap, I have been using the SEM of the Focused Ion Beam system in Micronova. I recommend attaching the sample facing outwards from the rod with which it is moved into the chamber. This way, the sample is imaged with negative angles but is upright.

Using higher acceleration voltages makes it easier to see through, so I have mostly used 30 kV. A higher acceleration voltage also helps when using small angles that are almost parallel with the surface. With these small angles, the image starts to bend on the edges and focusing (and correcting stigma) becomes impossible. To see through, one has to tilt to angles smaller than one degree, depending of course on how small the gap is. There is inevitably also an offset in the angle, so one might have to go to positive angles.

To be able to image the fluffy material hanging down from the mechanical resonator, small acceleration voltages should be used because the electrons very easily just travel through them. Therefore, not so tight angles can be used because of the abovementioned problems. One should also adjust the contrast such that the small differences can be seen. an SEM image of this unidentified material in the gap is shown in Fig. F.2.

Appendix G

Cryogenic setup

All the qubit-mechanics experiments were conducted in a Leiden MNK126 dilution cryostat with 600 μW cooling power at 120 mK. The cryostat was operated in an electrically shielded room and the helium dewar provided extra shielding from electrical radiation. The dewar also had a magnetic shield around it at room temperature. Within the vacuum can, a cylindrical copper radiation shield was attached to the still flange and a rectangular Amumetal 4K magnetic shield was attached to the cold finger. In the latest experiments, the internal surfaces of the radiation and magnetic shield were covered with Eccosorb coating 269E in order to absorb radiation from 1 K at microwave frequencies. However, the coating did not result in any appreciable change of qubit decoherence which could have been observed without dedicated measurements. All the experiment were performed at the base temperature at 25 mK.

The cryostat had a total of nine microwave cables going down to the base temperature. The setup had two cryogenic amplifiers attached to the 4 K stage so that four of the nine microwave lines were dedicated for amplifier inputs/outputs. The microwave cabling for the experiments that are presented in Publication **IV** is depicted in Fig. G.3. As for the dc cable to mechanical resonator, a thermocoax cable was used [100]. The dc line was further filtered with a homemade RC filter, see the measured low frequency transmission in Fig. G.2. For microwave frequencies up to 10 GHz, the minimum attenuation of the RC filter was 24 dB.

As the cryogenic pre-amplifier, Miteq AFS2-03000600-08-10P-2-CR microwave amplifier was used with a noise temperature ~4 K. The nominal bandwidth of the amplifier is 3-6 GHz.

A sample holder was made out of brass with lateral dimensions of 33×39 mm, shown in Fig. G.3 with the lid open. A sample holder was made out of three parts such that the fabricated chip was attached with varnish on the bottommost part.

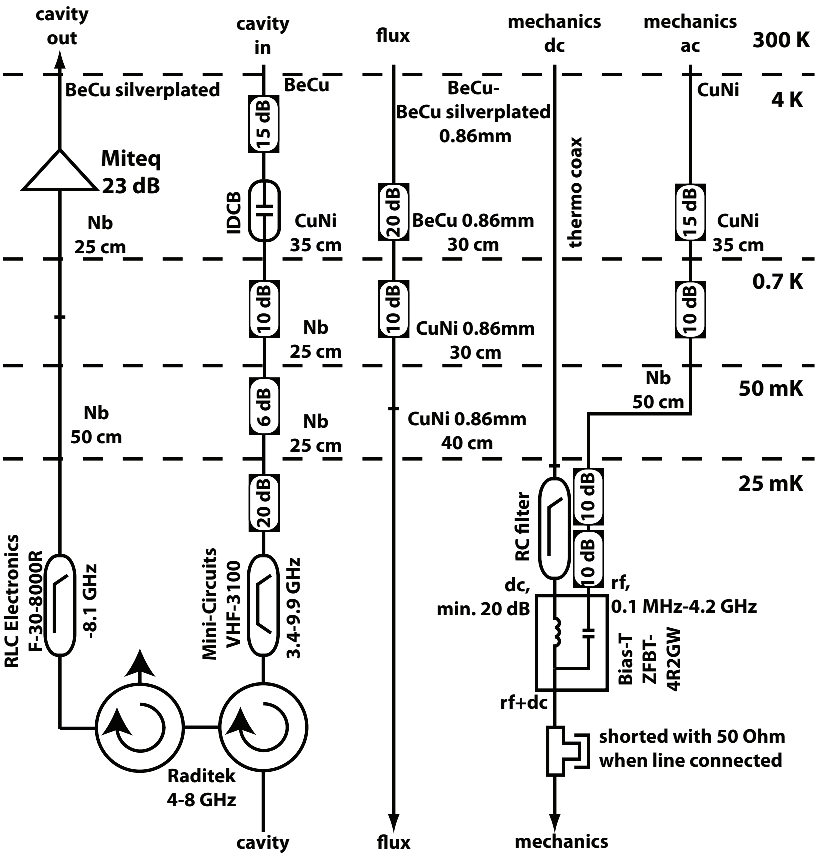

Fig. G.1: Dilution cryostat wiring in the transmon-mechanics experiments. For cables we used niobium (Nb), beryllium copper (BeCu), and Copper nickel (CuNi). Thinner wires are marked with their diameter and inner-pin dc block is abbreviated as IDCB. The measured transmission of the RC filter is shown in Fig. G.2.

The middle part contained the PCB board with a 4×4 mm hole in the center. The chip size was roughly 5×5 mm such that the edges of the PCB board lay on the chip. After attaching the middle part, the chip was tightened against the PCB board with screws from the bottommost part. The sample holder was designed such that with the lid closed, open vacuum spaces were minimized in order to avert box resonances at the range of 4-8 GHz.

The Rabi oscillation measurement setup is shown in Fig. G.4, which was used in Publication **IV**. The qubit excitation tone was pulsed using a Tektronix arbitrary waveform generator (AWG). The cavity reflection was measured using a network analyzer whose input tone was also pulsed using AWG. One signal generator was

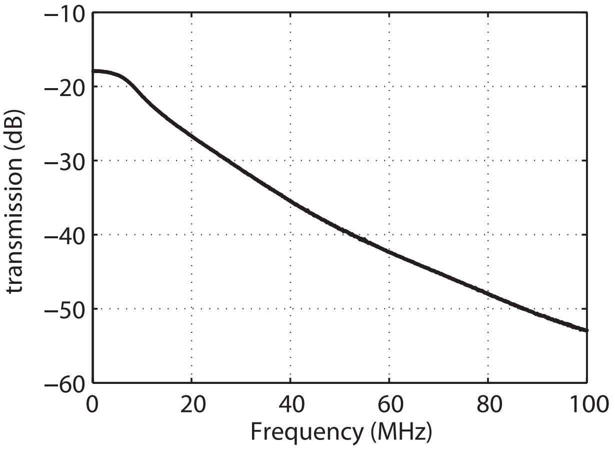

Fig. G.2: Measured attenuation of the homemade RC filter with $R = 660\ \Omega$.

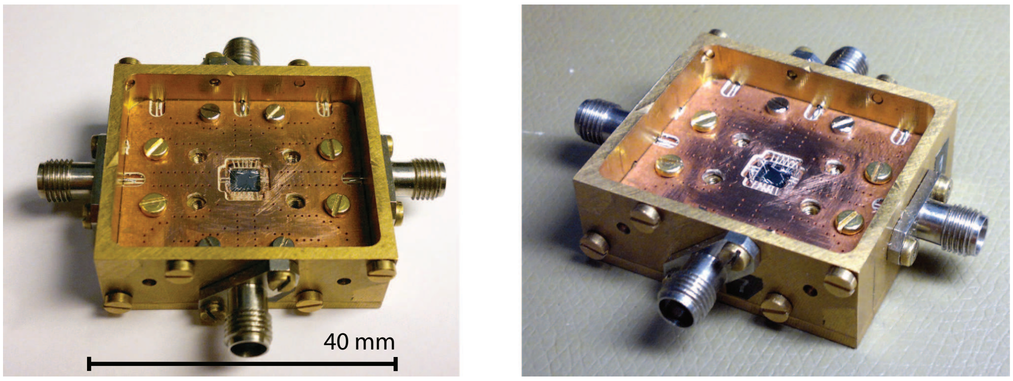

Fig. G.3: Sample holder with slots for up to eight SMA connectors. Top layer of the PCB board shown in the images is grounded with vias to the backside of the board.

used as a clock to trigger the qubit excitation pulses and the network analyzer simultaneously. The dc voltage to mechanics was not controlled by feedback but the mechanics was excited to the dynamical sweet spot such that the gate charge dependency practically vanished.

For the dynamic Stark shift measurement presented in Publication **IV**, gate charge was controlled. The room temperature measurement setup is depicted in Fig. G.5 for the dc voltage input to mechanics. Two voltage sources were used, one of which provided the large dc voltage that was regulated with a diode and inducing the coupling between the qubit and mechanics. The other voltage source was used to control the gate charge. Regularly during the measurements, the cavity

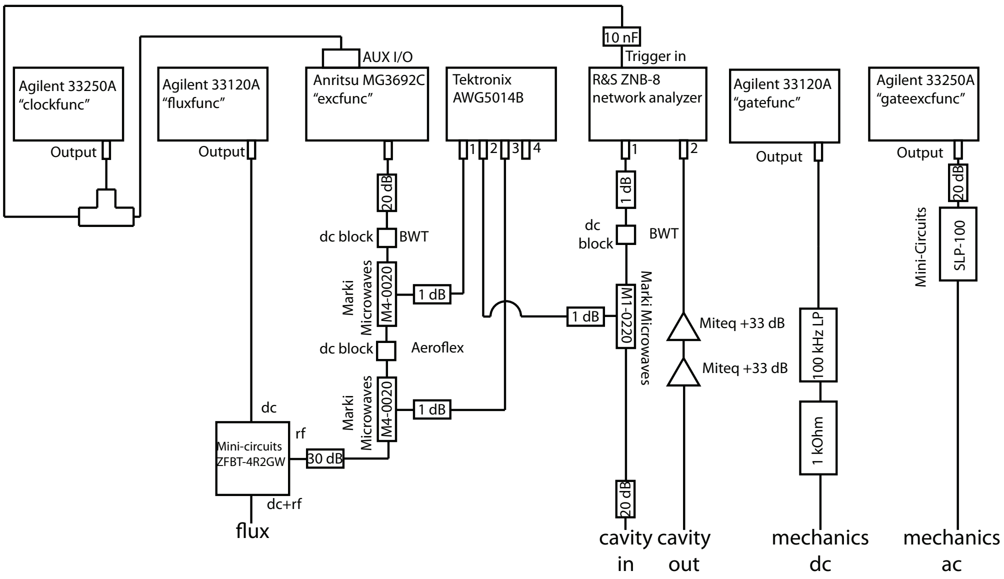

Fig. G.4: Measurement setup for Rabi oscillations. The qubit population is inferred by measuring the cavity reflection with a network analyzer. For the measurement in which the gate charge was controlled, see Fig. G.5.

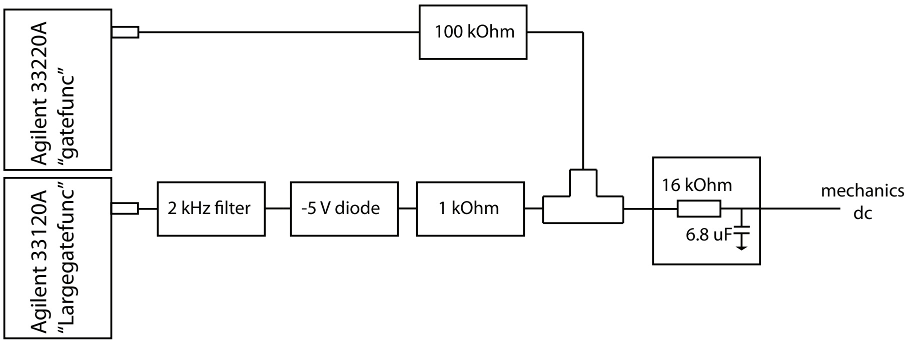

Fig. G.5: Voltage divider used for tuning the gate charge on top of a large ($\sim$5 V) gate voltage. This scheme gives roughly a division of one hundred to the voltage source controlling the gate charge. Further, an RC filter was used to attenuate ac signals from the voltage sources.

reflection was measured at a set frequency and the gate charge was tuned such that the cavity reflection reached the set value.

quantum bit-a transmon-to perform an analogue simulation of motional averaging, a phenomenon initially observed in nuclear magnetic resonance spectroscopy. By modulating the flux bias of a transmon with controllable pseudorandom telegraph noise we create a stochastic jump of its energy level separation between two discrete values. When the jumping is faster than a dynamical threshold set by the frequency displacement of the levels, the initially separate spectral lines merge into a single, narrow, motional-averaged line. With sinusoidal modulation a complex pattern of additional sidebands is observed. We show that the modulated system remains quantum coherent, with modified transition frequencies, Rabi couplings, and dephasing rates. These results represent the first steps towards more advanced quantum simulations using artificial atoms.

examples include cavity quantum electrodynamics, trapped ions, and electrons and phonons in the solid state. In those systems, strong coupling makes the constituents lose their individual character and form dressed states, which represent a collective form of dynamics. As well as having fundamental importance, hybrid systems also have practical applications, notably in the emerging field of quantum information control. A promising approach is to combine long-lived atomic states with the accessible electrical degrees of freedom in superconducting cavities and quantum bits (qubits). Here we integrate circuit cavity quantum electrodynamics with phonons. Apart from coupling to a microwave cavity, our superconducting transmon qubit, consisting of tunnel junctions and a capacitor, interacts with a phonon mode in a micromechanical resonator, and thus acts like an atom coupled to two different cavities. We measure the phonon Stark shift, as well as the splitting of the qubit spectral line into motional sidebands, which feature transitions between the dressed electromechanical states. In the time domain, we observe coherent conversion of qubit excitation to phonons as sideband Rabi oscillations. This is a model system with potential for a quantum interface, which may allow for storage of quantum information in long-lived phonon states, coupling to optical photons or for investigations of strongly coupled quantum systems near the classical limit.

Aalto-DD 24/2014

ISBN 978-952-60-5580-0
ISBN 978-952-60-5581-7 (pdf)
ISSN-L 1799-4934
ISSN 1799-4934
ISSN 1799-4942 (pdf)

Aalto University
School of Science
O.V. Lounasmaa Laboratory
Department of Applied Physics

BUSINESS +
ECONOMY

ART +
DESIGN +
ARCHITECTURE

SCIENCE +
TECHNOLOGY

CROSSOVER

DOCTORAL
DISSERTATIONS